

LEVEL II

②

AD A105616

HOT ELECTRON EFFECTS OF IMPORTANCE FOR
MICRON AND SUBMICRON DEVICES.

⑨ FINAL REPORT

⑩ K. HESS AND G. E. STILLMAN

⑪ SEPTEMBER 1981

OFFICE OF NAVAL RESEARCH

DTIC
ELECTE
OCT 14 1981
S D
H

NR 322-086

NO0014-79-C-0768

⑫ 77

COORDINATED SCIENCE LABORATORY
UNIVERSITY OF ILLINOIS AT URBANA-CHAMPAIGN
URBANA, ILL. 61801

DTIC FILE COPY

APPROVED FOR PUBLIC RELEASE;
DISTRIBUTION UNLIMITED.

047700

JCB

81 10 5 157

P-1

Accession #	NTIS	DTIC TAB	Unannounced	Justification
By	Distribution/	Availability Coc	Avail and/or	Special
Dist	A			

During the period of this contract fifteen papers have been published. The manuscripts concern lateral transport in superlattices, transport at extremely high electric fields and impact ionization and quantum well heterojunction lasers.

1. Lateral Transport in Superlattices

A new mechanism was introduced to obtain negative differential resistance in layered heterostructures for conduction parallel to the interface. The mechanism is based on hot-electron thermionic emission from high mobility GaAs into low mobility $\text{Al}_x\text{Ga}_{1-x}\text{As}$ and represents the real space analogy to the Gunn effect (paper 1). The validity of this idea was substantiated by phenomenological treatments (paper 2), Monte Carlo Simulations (paper 3) and experiments (paper 4). This effect is vital for any high field transport application in layered structures for scaling laws of the high mobility transistor, (T. Mimura, S. Hiyamizu, T. Fujii and K. Nambu, JJAP 19, 225-227, 1980) emission of electrons into substrates, etc. Our work on this effect continues especially with respect to the possibility of fast switching and storage between layers. The interest in this effect led to the development of a fairly complete theory of transport in heterolayers which was also treated and partly expanded by B. K. Ridley and P. Price.

2. Transport at Extremely High Electric Fields and Impact Ionization

We have developed a Monte Carlo simulation of impact ionization including the bandstructure as calculated by the empirical pseudopotential method (papers 5 and 7). We chose to include bandstructure effects into transport phenomena i.e. we calculated transport at high energies while all other groups in this area rather calculate transport at high fields.

We were able to show the vital importance of the bandstructure to impact ionization phenomena and to fit our results to most existing experimental data (except for the anisotropy measured by Pearsall as pointed out in paper 6). We consider this penetration to high energies and deep into the bands as vital for the development of high field transport and continue this project to include various materials and also high scattering rates.

We also investigated impact ionization in layered structures and designed a low noise avalanche photo diode. This structure was successfully fabricated at Bell Labs (Capasso et al. IEDM to be published) and confirms our theoretical predictions (paper 8).

3. Drift at Extremely High Electric Field

A system for measuring the high field drift with the microwave time of flight technique has been set up. It is currently successfully used in a follow up project (supported by ONR)

4. Quantum Well Heterojunction Lasers

Our work on quantum well heterojunction lasers centered on theoretical aspects of the participation of hot electrons and phonons in the laser operation. The work was performed in cooperation with the group of Professor N. Holonyak, Jr. and resulted in publications on phonon contributions to laser operation (9, 10) the effect of compositional disorder on the energy of the emitted light (11), exciton recombination (12), the temperature dependence of the threshold current (13), the effect of phonon reflectors (14) and finally in a summary of the hot-electron and laser research (Physics Today paper (15)).

PREVIOUS REPORTS

NR 322-086, University of Illinois at Urbana-Champaign, "Hot Electron Effects of Importance for Micron and Submicron Devices," P.I. - K. Hess and G. E. Stillman, (217) 333-6362, NO0014-79-C-0763.

The goal of this research is to understand the basic mechanisms of high-field electronic transport, drift, diffusion and generation-recombination in materials which are important or have high potential for device applications.

Progress: We have developed a computer program for high field transport which includes a realistic band structure as calculated by the empirical pseudopotential model. This numerical technique allows us to calculate impact ionization almost from first principles including the orientation dependence, energy loss by polar optical and deformation potential scattering and also spatial dependences as encountered in semiconductor heterojunctions (publications 1-3). Our investigations of transport in heterojunction layers led us to the concept of real space transfer or hot electron thermionic emission out of potential wells. This concept has, in our opinion, a high potential for novel device applications (publications 4,5). Part of our research was connected with scattering processes at interfaces and with transport in quantized inversion layers. Here we assessed the importance of remote phonon scattering (publication 6). The influence of the heating of electrons to suprathreshold levels on the threshold current of heterojunction lasers was investigated and it was found that the temperature dependence is reduced by these effects (publications 7,8). Finally, we investigated (in cooperation with Prof. N. Holonyak, Jr.) the influence of high phonon densities on quantum well heterojunction lasers. It was found that the phonon occupation numbers can be enhanced a factor 10 or more over the equilibrium thermodynamic average value in specific structures (publications 9-11).

Recent Publications:

1. H. Shichijo, K. Hess and G. E. Stillman, "Orientation Dependence of Ballistic Electron Transport and Impact Ionization," Electronics Letters 16, 208-210 (1980).
2. H. Shichijo, K. Hess and G. E. Stillman, "Simulation of High Field Transport in GaAs Using a Monte Carlo Method and Pseudopotential Band Structures," Appl. Phys. Lett. (submitted).
3. R. Chin, N. Holonyak, Jr., G. E. Stillman, J. Y. Tang and K. Hess, "Impact Ionization in Multilayered Heterojunction Structures," Electronics Letters 16, 467-469 (1980).
4. M. Keever, H. Shichijo, K. Hess, S. Panerjee, L. Witkowski, H. Morkoc and B. G. Streetman, "Measurements of Hot Electron Conduction and Real Space Transfer in GaAs-Al_xGa_{1-x}As Heterojunction Layers." Appl. Phys. Lett. (submitted).
5. T. H. Glission, J. R. Hauser, M. A. Littlejohn, K. Hess, B. G. Streetman and H. Shichijo, "Monte Carlo Simulation of Real-Space Electron Transfer in GaAs-AlGaAs Heterostructures," J. Appl. Phys. (in press).

6. D. K. Ferry, K. Hess and P. Vogl. "Physics and Modeling of Submicron Insulated-Gate Field-Effect Transistors. II. Transport in Quantized Inversion Layers," in Microstructure Science and Technology/VLSI, Norman Einspruch, Editor (New York: Academic Press, in press).
7. K. Hess, B. A. Vojak, N. Holonyak, Jr., R. Chin and P. D. Dapkus, "Temperature Dependence of Threshold Current for a Quantum-Well Heterostructure Laser," Solid State Electronics 23, 585-589 (1980).
8. R. Chin, N. Holonyak, Jr., B. A. Vojak, K. Hess, R. D. Dupuis and P. D. Dapkus, "Temperature Dependence of Threshold Current for Quantum-Well $\text{Al}_x\text{Ga}_{1-x}\text{As-GaAs}$ Heterostructure Laser Diodes," Appl. Phys. Lett. 36, 19-21 (1980).
9. N. Holonyak, Jr., R. M. Kolbas, W. D. Laidig, B. A. Vojak, K. Hess, R. D. Dupuis and P. D. Dapkus, "Phonon-Assisted Recombination and Stimulated Emission in Quantum-Well $\text{Al}_x\text{Ga}_{1-x}\text{As-GaAs}$ Heterostructures," J. Appl. Phys. 51, 1328-1337 (1980).
10. K. Hess, N. Holonyak, Jr., W. D. Laidig, B. A. Vojak, J. J. Coleman and P. D. Dapkus, "Hot Electrons and Phonons in Quantum-Well $\text{Al}_x\text{Ga}_{1-x}\text{As-GaAs}$ Heterostructures," Solid State Comm. 34, 749-752 (1980).
11. N. Holonyak, Jr., B. A. Vojak, W. D. Laidig, K. Hess, J. J. Coleman and P. D. Dapkus, "Phonon Contribution to Double-Heterojunction Laser Operation," Appl. Phys. Lett. 37, 135-138 (1980).

PUBLICATIONS

Abstract for an Invited Paper
for the New York Meeting of the
American Physical Society

24-28 March 1980

Date

Real Space Transfer of Hot Electrons in Modulation-Doped Structures. *
K. HESS, University of Illinois, Urbana. (30 min.)

Electronic transport in semiconductor heterojunction layers differs from "normal" bulk transport in several respects. Electrons may be confined to a potential well (typically 0.1 - 0.5 eV deep) and therefore may be separated from their parent donors and other scattering centers which are located in neighboring layers. As a consequence of this separation, ionized impurity scattering can be strongly reduced.¹ The scattering rate for the electron-phonon interaction is enhanced in layered structures. However, the enhancement is negligible as long as size quantization is unimportant.² Other departures from bulk properties arise for hot electrons in heterojunction layers. High electric fields parallel to the interface can supply enough energy to the electrons to allow them to propagate out of the well into the confinement layers, where they experience strong scattering. A similar effect can occur in MOS-transistors, metal-semiconductor field effect transistors, and charge coupled devices as an unwelcome side effect. In modulation doped GaAs-Al_xGa_{1-x}As heterojunction structures, however, there exists the possibility of new device applications. The transfer of electrons (in real space) from a high mobility layer (GaAs) to a low mobility layer (Al_xGa_{1-x}As) can give rise to negative differential resistance. The similarities and differences to the Hilsum-Ridley-Watkins mechanism (k-space transfer, Gunn effect) are discussed, based on results from the method of moments and Monte Carlo calculations.⁴

* Supported by the Office of Naval Research and the Joint Services Electronics Program.

¹L. Esaki and R. Tsu, IBM Research Report No. RC-2418, (1969). R. Dingle, H. L. Stormer, A. C. Gossard, and W. Wiegmann, Appl. Phys. Lett. 33, 665 (1978).

²R. M. Kolbas, N. Holonyak, Jr., B. A. Vojak, K. Hess, M. Altarelli, R. D. Dupuis and P. D. Dapkus, Solid State Communications, 31, 1033 (1979).

³K. Hess, H. Morkoç, H. Shichijo, and B. G. Streetman, Appl. Phys. Lett. 35, 469 (1979).

⁴T. H. Glisson, J. R. Hauser, M. A. Littlejohn, K. Hess, B. G. Streetman, and H. Shichijo, to be published.

REAL-SPACE ELECTRON TRANSFER BY THERMIONIC EMISSION IN GaAs-Al_xGa_{1-x}As HETEROSTRUCTURES: ANALYTICAL MODEL FOR LARGE LAYER WIDTHS†

H. SHICHUO, K. HESS and B. G. STREETMAN

Department of Electrical Engineering and Coordinated Science Laboratory, University of Illinois at Urbana-Champaign, Urbana, IL 61801, U.S.A.

(Received 29 October 1979; in revised form 7 January 1980)

Abstract—Calculations are presented for negative differential resistance (NDR) and switching in layered GaAs-Al_xGa_{1-x}As heterostructures with a high electric field parallel to the interface. The mechanism is based on thermionic emission of hot electrons from the GaAs layers into the Al_xGa_{1-x}As layers. An analytical model is obtained in the limit of relatively large layer widths (400 Å or wider). The method of moments is employed to solve the Boltzmann equation, assuming a position-dependent electron temperature and Quasi-Fermi level in the Al_xGa_{1-x}As layers, and a position-independent electron temperature and Quasi-Fermi level in the narrower GaAs layer. Thermal conduction of hot electrons from the GaAs layer into the Al_xGa_{1-x}As layers is taken into account. The results of the calculations show that the threshold electric field for the onset of NDR and the peak-to-valley ratio can be controlled to a large extent by adjusting the mobility of the Al_xGa_{1-x}As layer, the layer dimensions, and the potential barrier (Al mole fraction in the Al_xGa_{1-x}As).

NOTATION

E_0	effective field strength $E_0 = me\omega_0 \left(\frac{1}{\epsilon_x} - \frac{1}{\epsilon_0} \right) / 4\pi\hbar$
E_{F1}	Quasi-Fermi level in the GaAs layer
$E_{F2}(x)$	position-dependent Quasi-Fermi level in the Al _x Ga _{1-x} As layer
ϵ	energy of the electron
F	applied electric field
$\hbar\omega_0$	optical phonon energy in the GaAs
j_{1-2}	thermionic current from the GaAs layer to the Al _x Ga _{1-x} As layer
j_{2-1}	thermionic current from the Al _x Ga _{1-x} As layer to the GaAs layer
K_0	Bessel function of order 0
K_1	Bessel function of order 1
k_x, k_y	components of the electron wave vector
L_1	width of the GaAs layer
L_2	width of the Al _x Ga _{1-x} As layer
m^*	electron effective mass in GaAs
m_x^*	electron effective mass in Al _x Ga _{1-x} As
N	total number of electrons in the system
N_1	number of electrons in the GaAs layer
N_2	number of electrons in the Al _x Ga _{1-x} As layer
T_0	lattice temperature
T_e	electron temperature in the GaAs
$T_L(x)$	position-dependent electron temperature in the Al _x Ga _{1-x} As
ΔE	potential barrier height
μ_1	electron mobility in GaAs
μ_2	electron mobility in Al _x Ga _{1-x} As

1. INTRODUCTION

Negative differential effects, typified by the tunnel diode and the Gunn diode, are of fundamental interest and are

also important for their possible applications to microwave, switching, and memory devices. Recently a new mechanism has been proposed to obtain negative differential resistance (NDR) in semiconductor heterostructures[1]. The basic structure of this device consists of alternating GaAs-Al_xGa_{1-x}As multilayers, or other appropriate lattice-matched materials with dissimilar band-gap energies and carrier mobilities. It has been mentioned[1] that this mechanism may benefit from modulation doping[2, 3] of the layers. In such a structure electrons reside primarily in the GaAs potential wells at equilibrium. NDR is obtained by applying a high electric field parallel to the layer interface, sufficient to cause thermionic emission of hot electrons from the high-mobility GaAs layers into the neighboring low-mobility Al_xGa_{1-x}As layers. We have previously calculated current-voltage characteristics for such structures[1], which exhibit NDR at an electric field of 3.4 kV/cm. In those preliminary calculations, however, the GaAs and the Al_xGa_{1-x}As layers were treated independently in the sense that the exchange of energy and momentum by the electrons in the GaAs and the Al_xGa_{1-x}As layers was not taken into account. Therefore, the current-voltage characteristics showed the "polar runaway" at an electric field of 3.4 kV/cm typical of polar optical phonon scattering. In a more realistic treatment, however, one must account for exchange of electrons between the layers, and consequently exchange of energy by the transfer of hot electrons into the Al_xGa_{1-x}As layer and the reverse transfer of cooler electrons into the GaAs. In this paper we extend our previous calculations to include this effect in the limit of large layer dimensions. We used the method of moments to solve the Boltzmann equation at the GaAs-Al_xGa_{1-x}As interface, assuming a position-

†Supported by the Joint Services Electronics Program (U.S. Army, U.S. Navy, U.S. Air Force) under Contract Number N00014-79-C-0424, and the Office of Naval Research under Contract Number N00014-76-C-0768.

dependent electron temperature and Fermi level in the $\text{Al}_x\text{Ga}_{1-x}\text{As}$ layer. Special attention is given to the degree of control of the device characteristics by the adjustment of the following parameters: the mobility of the $\text{Al}_x\text{Ga}_{1-x}\text{As}$ layer; the layer dimensions; the Al mole fraction (and therefore the potential barrier height).

2. ANALYTICAL CONSIDERATIONS

Figure 1 shows schematically the band structure, doping distribution, and electron mobility of modulation-doped GaAs- $\text{Al}_x\text{Ga}_{1-x}\text{As}$ layers. The $\text{Al}_x\text{Ga}_{1-x}\text{As}$ layers are intentionally doped to a density of $10^{17} \sim 10^{18} \text{ cm}^{-3}$, whereas the GaAs layers contain only unintentional background impurities ($10^{14} \sim 10^{15} \text{ cm}^{-3}$) [2]. At thermal equilibrium the electrons reside at the minimum of the potential wells, i.e. in the GaAs layers. When separated from their parent donors by more than 200 Å these electrons experience strongly reduced impurity scattering [2, 4]. Therefore, for a typical layer thickness of 400 Å the electron mobility in the GaAs layer will be very high ($\geq 5000 \text{ cm}^2/\text{V}\cdot\text{sec}$ at 300 K). Dingle *et al.* have experimentally observed a mobility of $5000 \text{ cm}^2/\text{V}\cdot\text{sec}$ at 300 K, and even higher mobilities ($\sim 15000 \text{ cm}^2/\text{V}\cdot\text{sec}$) at lower temperatures [2]. The $\text{Al}_x\text{Ga}_{1-x}\text{As}$ layers can be made strongly compensated, and thereby the mobility in these layers can be very low ($\sim 500 \text{ cm}^2/\text{V}\cdot\text{sec}$ or less). Application of a high electric field parallel to the layer interfaces of this structure will result in heating of the high mobility electrons in the GaAs layer only. When the mean kinetic energy of these electrons becomes comparable to the potential barrier height, ΔE , they can be thermionically emitted into the $\text{Al}_x\text{Ga}_{1-x}\text{As}$. During the transfer from the high mobility GaAs layer to the low mobility $\text{Al}_x\text{Ga}_{1-x}\text{As}$ layer, the sample should exhibit negative differential resistance.

The problem is complicated by the fact that some of the cooler electrons in the $\text{Al}_x\text{Ga}_{1-x}\text{As}$ can undergo reverse transfer into the GaAs layer. In order to take account of

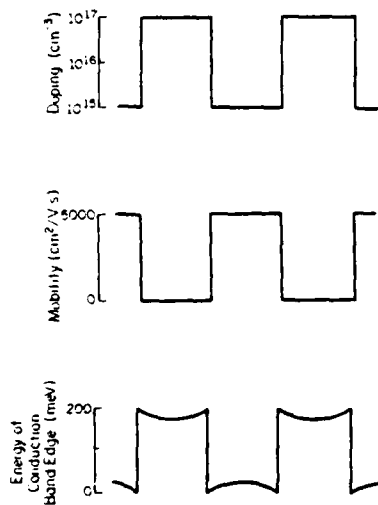


Fig. 1. Schematic diagrams of doping density, electron mobility, and conduction band energy of modulation-doped layers.

this energy and momentum exchange between the GaAs and the $\text{Al}_x\text{Ga}_{1-x}\text{As}$ layers, one must solve the Boltzmann equation:

$$\frac{\partial f}{\partial t} + \frac{1}{\hbar} \mathbf{F} \cdot \nabla_{\mathbf{k}} f - \mathbf{v} \cdot \nabla_{\mathbf{r}} f = \left. \frac{\partial f}{\partial t} \right|_c \quad (1)$$

with appropriate boundary conditions. Due to the complexity of the boundary conditions in the case of real space transfer, an explicit expression for the distribution function cannot be obtained. Therefore we assume a Maxwellian form for the isotropic part of the distribution function, with a position-dependent electron temperature. This assumption is justified by the fact that the electron density is high in the GaAs layer at the start of the electron transfer, since the GaAs layer collects electrons from the neighboring layers. Typically the GaAs layer will have an electron density of $10^{18} \sim 10^{19} \text{ cm}^{-3}$. Electron-electron collisions will, therefore randomize the energy gained in the electric field direction and establish a Maxwellian distribution. Above the band edge of the $\text{Al}_x\text{Ga}_{1-x}\text{As}$ the electrons in the GaAs will follow a "cooler" distribution function because of the reverse transfer of cooler electrons from the $\text{Al}_x\text{Ga}_{1-x}\text{As}$. For the sake of simplicity, however, we will assume the GaAs layer is sufficiently narrow that a single electron temperature can be used in the GaAs.

In the calculations we have deliberately chosen typical layer widths larger than 400 Å. This will avoid the complications arising from size quantization effects and other two-dimensional effects. One of the consequences of such effects is the increase of the NDR threshold electric field by a factor of two at room temperature [1]. This occurs because polar optical phonon scattering is enhanced in two-dimensional systems. The choice of large layer width also allows the use of the semiclassical Boltzmann equation. With large layer widths, the potential fluctuations due to the statistical distribution of the impurities can also be neglected. Supposedly, however, the transfer speed is slower for large layers, which is not considered here.

Figure 2 shows the model used in the calculations. We assume a position-dependent electron temperature, $T_L(x)$, and Fermi level, $E_{F2}(x)$, in the $\text{Al}_x\text{Ga}_{1-x}\text{As}$ layer. Because of the small dimensions, the use of the Quasi-Fermi level is justified only at very high electron densities. Similar methods have recently been employed by others [5] to analyze the thermionic emission in metal-

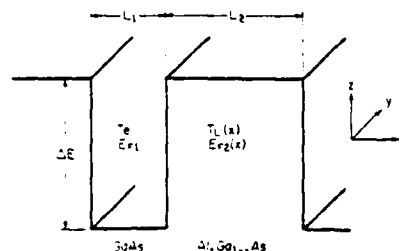


Fig. 2. Simplified electron-temperature model with coordinate system used for the calculations.

GaAs contacts. In the independent electron approximation, E_{F1} . With this assumption, position dependence of the Fermi level in the Al_xGa_{1-x}As layer is $T_L(x)$ at the interface. At the boundary the slope of $T_L(x)$ is assumed to be the same as the slope of $T_L(x)$ is extracted. We then proceed to form:

$$f = f_0(\epsilon, x)$$

where $f_0(\epsilon, x)$ is a Maxwellian distribution

$$f_0(\epsilon, x) = \frac{1}{4\pi^{3/2}} \exp\left(-\frac{\epsilon - E_{F2}(x)}{kT_L(x)}\right)$$

The coordinate system is in the y -direction. t represents the drift time. The third term is to take account of the electric field. It represents the distribution perpendicular to the electric field directions. After integration of eqn (1), we then obtain the equations for the spherical terms. The method of obtaining the equations is as follows:

$$\left(\frac{2\hbar\omega_0}{\pi m^*}\right)^{1/2} e E_0 \frac{\exp(Z_L)}{\exp(Z_0)} = e \mu_2 F^2 + \frac{5\mu_2}{2e} (kT_L)^{-3/2}$$

$$\frac{d^2}{dx^2} (kT_L)$$

where $Z_L = \frac{kT_L}{\hbar\omega_0}$, $Z_0 = \frac{kT_0}{\hbar\omega_0}$ of $E_{F2}(x)$ and $T_L(x)$ in eqn (4) is the rate of scattering [6], and the power input from the term on the right represents the GaAs due to the transfer of energy. We can then obtain a similar equation for T_L and F (electric field)

$$\left(\frac{2\hbar\omega_0}{\pi m^*}\right)^{1/2} e E_0 \frac{\exp(Z_L)}{\exp(Z_0)}$$

in the GaAs
the Boltzmann

(1)

to the com-
case of real
distribution
we assume a
distribution
electron tem-
fact that the
at the start of
collects elec-
the GaAs
 $\sim 10^{19} \text{ cm}^{-3}$.
randomize
direction and
the band edge
As will follow
of the reverse
GaAs. For
assume the
single electron

chosen typical
avoid the com-
fects and other
sequences of
threshold electric
ture[1]. This
scattering is
The choice of
semiclassical
ons, the poten-
tiation of the
ably, however,
s, which is not

calculations. We
temperature.
GaAs layer.
of the Quasi-
electron den-
employed by
on in metal-

with coordinate

GaAs contacts. In the GaAs layer we assume a position-independent electron temperature, T_e , and Fermi level, E_{F1} . With this assumption we only need to solve for the position dependence of the electron temperature and the Fermi level in the $\text{Al}_x\text{Ga}_{1-x}\text{As}$ layers. The thermal conduction of hot electrons from the GaAs layer into the $\text{Al}_x\text{Ga}_{1-x}\text{As}$ layers is then accounted for by the slope of $T_L(x)$ at the interface boundary. Although at the boundary the slope of T_e in the GaAs layer is zero, we assume that the same amount of energy (as given by the slope of $T_L(x)$) is extracted from the GaAs.

We then proceed to assume a distribution function of a form;

$$f = f_0(\epsilon, x) + g(\epsilon, x)k_y + h(\epsilon, x)k_x, \quad (2)$$

where $f_0(\epsilon, x)$ is a Maxwellian distribution;

$$f_0(\epsilon, x) = \exp\left[\frac{E_{F2}(x) - \epsilon}{kT_L(x)}\right]. \quad (3)$$

The coordinate system is shown in Fig. 2. The electric field is in the y -direction. The second term of eqn (2) represents the drift term of the distribution along the electric field as is usual for a spatially uniform system[6]. The third term is to take into account the spatial nonuniformity. It represents the displacement of the distribution perpendicular to the electric field. This term is essential to account for the energy flow normal to the field directions. After substituting eqn (2) into the Boltzmann eqn (1), we then separate the variables into equations for the spherical symmetric part and the drift terms. The method of moments[7] is then utilized to obtain the equations for $T_L(x)$ and $E_{F2}(x)$. The set of equations obtained is given below:

$$\left(\frac{2\hbar\omega_0}{\pi m^*}\right)^{1/2} eE_0 \frac{\exp(Z_0 - Z_L) - 1}{\exp(Z_0) - 1} Z^{1/2} \exp(Z/2) K_0(Z/2) \\ = e\mu_2 F^2 + \frac{5\mu_2}{2e} (kT_L)^{-3/2} \exp(-E_{F2}/kT_L) \frac{d^2}{dx^2} \\ \{[(kT_L)^{3/2} \exp(E_{F2}/kT_L)]\} \quad (4)$$

$$\frac{d^2}{dx^2} [(kT_L)^{5/2} \exp(E_{F2}/kT_L)] = 0 \quad (5)$$

where $Z_L = \frac{kT_L}{\hbar\omega_0}$, $Z_0 = \frac{kT_0}{\hbar\omega_0}$, and the position dependences of $E_{F2}(x)$ and $T_L(x)$ have been omitted. The left side of eqn (4) is the rate of energy loss due to polar optical scattering[6], and the first term on the right side is the power input from the applied electric field. The second term on the right represents the energy flow from the GaAs due to the transfer of hot electrons. With the assumption of energy conservation at the boundary, we can then obtain a similar power balance equation relating T_e and F (electric field) in the GaAs layer;

$$\left(\frac{2\hbar\omega_0}{\pi m^*}\right)^{1/2} eE_0 \frac{\exp(Z_0 - Z_e) - 1}{\exp(Z_0) - 1} Z^{1/2} \exp(Z/2) K_0(Z/2)$$

$$= e\mu_1 F^2 + \frac{5\mu_2}{2eL_1} k^2 T_L(0) \frac{dT_L(0)}{dx}, \quad (6)$$

where $Z_e = \frac{kT_e}{\hbar\omega_0}$, and μ_1 is the mobility in the GaAs when only polar optical scattering is operative. This mobility is given by:

$$\mu_1 = \frac{3\sqrt{\pi}}{2E_0} \left(\frac{2\hbar\omega_0}{m^*}\right)^{1/2} \frac{1}{N_q} Z_e^{-3/2} \exp(-Z_d/2) \\ \times \{[\exp(Z_0 - Z_e) + 1] K_1(Z_d/2) \\ + [\exp(Z_0 - Z_e) - 1] K_0(Z_d/2)\}^{-1}. \quad (7)$$

The second term on the right side of eqn. (6) represents the power flowing out of the GaAs into the $\text{Al}_x\text{Ga}_{1-x}\text{As}$ layers. $T_L(0)$ and $dT_L(0)/dx$ are evaluated at the boundary $x = 0$. We have used the fact that this power flow is due only to those electrons in the GaAs with energy higher than the $\text{Al}_x\text{Ga}_{1-x}\text{As}$ band edge. Equation (4) combined with eqn (5) is now solved numerically with the boundary condition $T_L(0) = T_e$.

To determine the Quasi-Fermi levels, E_{F1} and $E_{F2}(x)$, we need two additional conditions. One is obtained from the condition $j_x = 0$. We simplify this condition to the balance of the thermionic currents in both directions at the interface. Under collision-free transport conditions the thermionic current j_{1-2} , from the GaAs to the $\text{Al}_x\text{Ga}_{1-x}\text{As}$, is given after Bethe[8] by;

$$j_{1-2} = \frac{em^*}{2\pi^2\hbar^3} (KT_e)^2 \exp\left[\frac{E_{F1} - \Delta E}{kT_e}\right]. \quad (8)$$

The current j_{2-1} , flowing from the $\text{Al}_x\text{Ga}_{1-x}\text{As}$ to the GaAs layer is:

$$j_{2-1} = \frac{em^*}{2\pi^2\hbar^3} (KT_L)^2 \exp\left[\frac{E_{F2} - \Delta E}{kT_L}\right], \quad (9)$$

where T_L is evaluated at $x = 0$. Under steady-state conditions we have $j_{1-2} = j_{2-1}$. The other additional condition arises from conservation of the total number of electrons, $N = N_1 + N_2$. N_1 and N_2 are calculated using the electron temperature and Fermi level in each layer.

3. NUMERICAL RESULTS

From eqn (6) we obtain the variation of electron temperature, T_e , with the electric field in the GaAs layer. The result is shown in Fig. 3 with the mobility in the $\text{Al}_x\text{Ga}_{1-x}\text{As}$ as a parameter. The dashed curve is for bulk GaAs, with only polar optical scattering operative. This corresponds to treating the GaAs and the $\text{Al}_x\text{Ga}_{1-x}\text{As}$ layers independently (in other words, $\mu_2 = 0$). As is well known[9], at an electric field of about 3.4 kV/cm the electron temperature goes to infinity and "polar runaway" occurs. When the transport of hot electrons is taken into account, however, the electron temperature does not increase as rapidly. The rate of increase is slower for higher mobility in the $\text{Al}_x\text{Ga}_{1-x}\text{As}$, because of the larger power out-flow. This situation is quite analo-

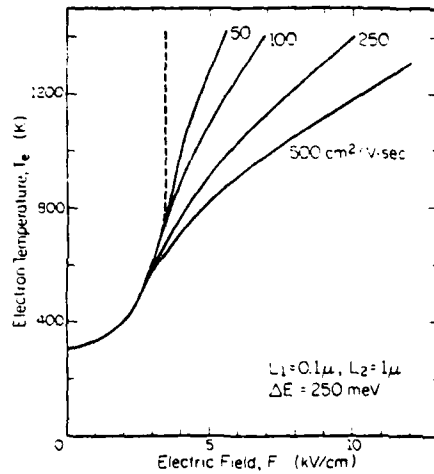


Fig. 3. Variation of electron temperature in the GaAs layer with applied field for various mobilities in the $\text{Al}_x\text{Ga}_{1-x}\text{As}$ layer.

gous to the Gunn effect[9], where intervalley scattering supplies an additional energy loss mechanism[11].

Figure 4 shows the position dependence of both the electron temperature, $T_L(x)$, and the Fermi level, $E_{F_2}(x)$ for several different values of electric field. The dashed line indicates the GaAs potential well. The interface is set at $x = 0$. It can be seen that both $T_L(x)$ and $E_{F_2}(x)$ approach their thermal equilibrium values within a distance on the order of $0.1 \mu\text{m}$. The small spikes in the Quasi-Fermi levels which occur at the boundary arise from the imposed condition of thermionic current balance and also from the small difference in effective masses. These spikes are of no physical significance. The rapid decrease of the Fermi level in the GaAs with higher fields indicates the depletion of electrons in this layer, and hence the transfer of electrons into the $\text{Al}_x\text{Ga}_{1-x}\text{As}$. The variation of the fraction of electrons in the GaAs

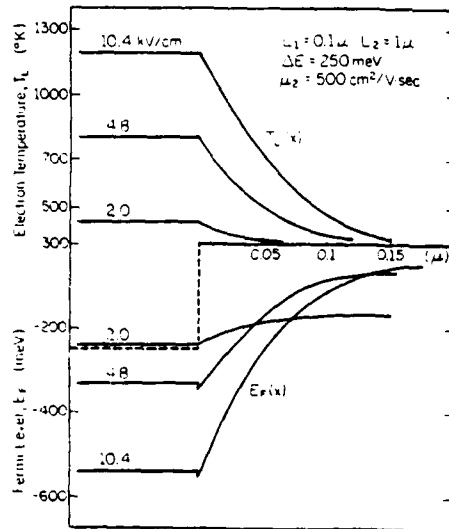


Fig. 4. Electron temperature and Fermi level as functions of position. The GaAs potential well is shown in the dashed line. The interface between the GaAs and the $\text{Al}_x\text{Ga}_{1-x}\text{As}$ is set at $x = 0$.

layer with increased field is more clearly illustrated in Fig. 5. The transfer is larger for smaller mobility values, a consequence of the greater carrier heating for smaller mobility as seen in Fig. 3. Here again the analogy with the Gunn effect should be noted[12].

The current-voltage characteristics are straightforward to calculate from this model. The results of the calculations are shown in Fig. 6. The magnitude of the NDR changes dramatically with the mobility in the $\text{Al}_x\text{Ga}_{1-x}\text{As}$ layer. For purposes of comparison we include in Fig. 6 (insert) the velocity-field characteristics calculated by Fawcett *et al.* in 1970 for the Gunn effect[13]. The parameter for their curves was the intervalley deformation potential.

The two sets of curves in Fig. 6 show surprisingly similar features. Actually, our discussion of real space transfer almost parallels that of the Gunn effect, but with two crucial differences. First, in our mechanism electrons leave the high mobility GaAs layer by thermionic emission and are transferred in *real space* to the low-

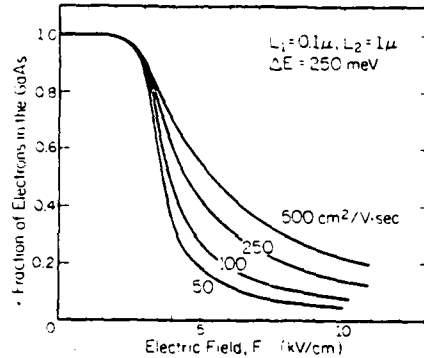


Fig. 5. Fraction of electrons in the GaAs layer as a function of electric field for various mobilities in the $\text{Al}_x\text{Ga}_{1-x}\text{As}$ layer.

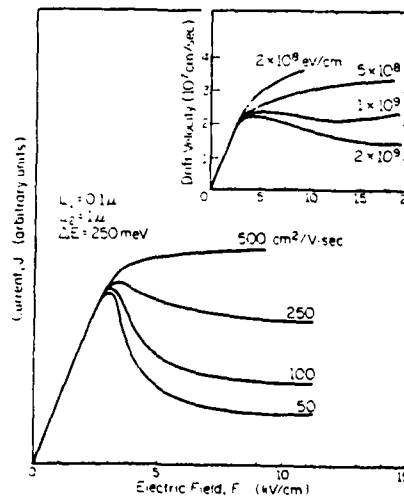


Fig. 6. Current-voltage characteristics for a real-space transfer device with various values of electron mobility in the $\text{Al}_x\text{Ga}_{1-x}\text{As}$ layer. The inset shows the velocity-field characteristics of the Gunn effect in GaAs for various intervalley deformation potentials[13].



Fig. 7. Current-voltage characteristics for various mobilities. Note the dip in the current near the conduction band edge.

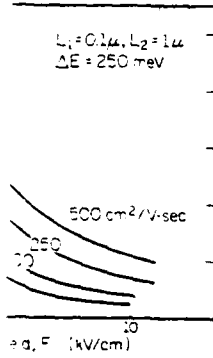
mobility $\text{Al}_x\text{Ga}_{1-x}\text{As}$ layer. On the other hand, electron transfer to an adjacent space. A second, crucial difference is that our device has a greater degree of real space transfer than the Gunn effect. As already noted, the intervalley scattering mechanism potential, which is not present for the real-space transfer, is absent in the $\text{Al}_x\text{Ga}_{1-x}\text{As}$ layer. The doping of the $\text{Al}_x\text{Ga}_{1-x}\text{As}$ layer can be changed by varying the layer dimensions. For example, the potential barrier height can be changed by changing the Al mole fraction. The effect of varying the layer thickness on the characteristics is still under investigation. The effects of the other parameters can be varied between the GaAs and the $\text{Al}_x\text{Ga}_{1-x}\text{As}$ layer. The effects of the other parameters on the NDR is more pronounced.

Finally, we would like to mention a limitation of our model. As shown in Fig. 6, the band-bending caused by the ionized donor impurities in the $\text{Al}_x\text{Ga}_{1-x}\text{As}$ layer can be quite large. The ionized donor impurities in the $\text{Al}_x\text{Ga}_{1-x}\text{As}$ layer tend to aid the transfer of electrons toward the GaAs layer. We believe that the band-bending effect in the $\text{Al}_x\text{Ga}_{1-x}\text{As}$ layer will aid the transfer of electrons from the $\text{Al}_x\text{Ga}_{1-x}\text{As}$ layer to the GaAs layer. The band-bending effect in the $\text{Al}_x\text{Ga}_{1-x}\text{As}$ layer will account for the effect of the ionized donor impurities which are known to be present above the Γ minimum of the conduction band edge of the GaAs layer.

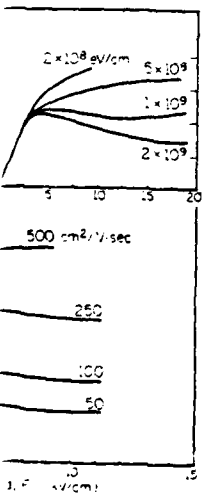
are clearly illustrated in Fig. 5. For smaller mobility values, a carrier heating for smaller barrier heights again the analogy with [12].

Characteristics are straightforward. The results of the calculation show the magnitude of the NDR in the mobility in the cases of comparison we in velocity-field characteristics [13]. In 1970 for the Gunn effect their curves was the inter-

Fig. 6 show surprisingly our discussion of real space of the Gunn effect, but with st. in our mechanism elec- y GaAs layer by thermionic d in real space to the low-



the GaAs layer as a function of mobilities in the Al_xGa_{1-x}As layer.



Characteristics for a real-space transfer of electron mobility in the shows the velocity-field charac- in GaAs for various intervalley potentials [13].

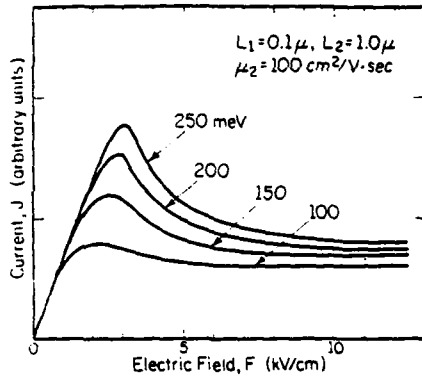


Fig. 7. Current-voltage characteristics for various potential barrier heights. Note that the GaAs L minima are above the conduction band edge of the Al_xGa_{1-x}As in the cases shown.

mobility Al_xGa_{1-x}As layer. In the Gunn effect, on the other hand, electrons transfer from one valley of high mobility to another of low mobility or k space. A second, and most important distinction is the fact that our device characteristics can be controlled to a greater degree than with a device utilizing the Gunn effect. As already seen in Fig. 6 (insert), the curves for the Gunn effect have as a parameter the intervalley deformation potential, which is a material property and cannot be changed. On the other hand, the parameter in Fig. 6 for the real-space transfer process is the mobility of the Al_xGa_{1-x}As layer, which can be controlled by adjusting the doping of the layer. The characteristics can also be changed by varying other device parameters, such as the layer dimensions and the potential barrier height. For example, the potential barrier height can be controlled by changing the Al mole fraction of the Al_xGa_{1-x}As. The effect of varying this parameter on the current-voltage characteristics is shown in Fig. 7. For this particular set of parameters the threshold field for the onset of NDR can be varied between 2 and 3 kV/cm and the peak-to-valley ratio between 1.3 and 2.0. We have also examined the effects of the operating temperature and as expected, the NDR is more pronounced at lower temperatures.

Finally, we would like to summarize the simplification of our model. As shown in Fig. 2, we have ignored the band-bending caused by the ionized donors. This effect can be quite large for heavily doped Al_xGa_{1-x}As layers. The ionized donors create an electric field at the GaAs-Al_xGa_{1-x}As interface which tends to pull the hot electrons toward the Al_xGa_{1-x}As layer. Therefore, we believe that the band-bending due to ionized donors should aid the transfer of electrons into the low-mobility Al_xGa_{1-x}As layers. Of course, as greater numbers of electrons are transferred, the effect becomes smaller since more ionized donors are neutralized. This band-bending effect is also reduced for compensated Al_xGa_{1-x}As layers. Secondly, we have not taken into account the effects of the conduction band L minima, which are known to be located approximately 330 meV above the Γ minimum of GaAs. We have deliberately chosen values of ΔE such that these L minima are above the band edge of the Al_xGa_{1-x}As (see for example, Fig.

7). As the Al_xGa_{1-x}As band edge approaches the GaAs L minima, some electrons may be transferred to these L minima by intervalley scattering before they undergo transfer in real space to the Al_xGa_{1-x}As layer. However, Monte Carlo calculations [14] show that the effects of the L minima are negligible and that real space transfer dominates over intervalley scattering even for a barrier height of ΔE = 200 meV. For values of ΔE = 250 meV and more, however, the effect of the L minima can be considerable. In fact, by intentionally aligning the Al_xGa_{1-x}As band edge to the energy value of the L minima in GaAs, the Gunn effect can be enhanced by real space transfer, and larger peak-to-valley ratios should result. Third and finally, we have neglected the quantum mechanical reflection of electrons at the GaAs-Al_xGa_{1-x}As interface. Wu and Yang [15] have obtained the formula for the three-dimensional transmission coefficient at a heterostructure interface using quantum mechanical considerations. When an electron with an energy of 230 meV is moving perpendicular to an interface with a barrier height of 200 meV, we obtain a transmission coefficient value of 75% using their formula. Therefore, some electrons are reflected into the GaAs layer when trying to cross the interface. Similarly, some of those electrons which have already transferred into the Al_xGa_{1-x}As are also reflected at the interface.

The effects of thermionic emission can also be used to construct a high-speed switch. If the GaAs and the Al_xGa_{1-x}As layers are contacted separately, voltages can be applied independently to the two materials or between them. There will be a negligible current in the Al_xGa_{1-x}As until an appreciable fraction of electrons are emitted from the GaAs. Figure 8 illustrates this switching effect. The electric field to the Al_xGa_{1-x}As is kept constant at 12 kV/cm. The GaAs and the Al_xGa_{1-x}As currents can be switched on and off by the electric field applied to the GaAs layer. The dotted curve is obtained in the case of no thermal conduction. Since the transfer times in this mechanism are short (~10⁻¹¹ sec) [1], a high-speed switch can be envisioned. Extensions of the real space transfer mechanism might include variation of the effective barrier height by application of voltage

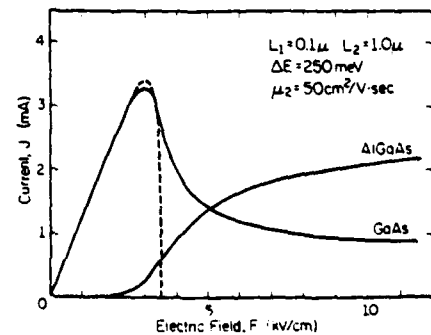


Fig. 8. Switching characteristics of a real-space transfer device. The GaAs and the Al_xGa_{1-x}As layers are contacted separately. The electric field to the Al_xGa_{1-x}As layers is kept constant at 12 kV/cm. Each layer can be switched on and off by the applied field to the GaAs layer.

between the layers, detection of optical excitations from the GaAs well by monitoring the $\text{Al}_x\text{Ga}_{1-x}\text{As}$ conductivity, and other applications.

4. CONCLUSIONS

We have described a mechanism to obtain negative differential resistance and switching in layered GaAs- $\text{Al}_x\text{Ga}_{1-x}\text{As}$ heterostructures with high electric fields applied parallel to the interfaces. The mechanism is based on thermionic emission of hot electrons from high mobility GaAs layers into low mobility $\text{Al}_x\text{Ga}_{1-x}\text{As}$ layers. An analytical model has been presented in the limit of large layer width, typically 400 Å or wider. We have employed the method of moments to solve the Boltzmann equation assuming a position-dependent electron temperature, $T_L(x)$, and Fermi level, $E_{F2}(x)$, in the $\text{Al}_x\text{Ga}_{1-x}\text{As}$ layer and a position-independent electron temperature, T_e , and Fermi level, E_{F1} , in the GaAs layer. The thermal conduction of hot electrons from the GaAs layers into the $\text{Al}_x\text{Ga}_{1-x}\text{As}$ layers is taken into account. As a consequence, the power balance equation contains an additional term. The resulting differential equation for $T_L(x)$ has been solved numerically. The results of the calculations show the device characteristics are similar to those for the Gunn effect. The crucial difference between the Gunn effect and the real-space transfer mechanism is that our device characteristics can be engineered by adjusting various parameters. The effects of changing the mobility in the $\text{Al}_x\text{Ga}_{1-x}\text{As}$ layers are apparent from Figs. 5 and 6. The characteristics can also be varied by changing the layer dimensions and Al

mole fraction (potential barrier height, Fig. 7). This degree of control of device characteristics makes the real-space transfer mechanism especially attractive for various applications.

Acknowledgements—We would like to thank Prof. H. Morkoç and J. Oberstar for helpful discussions.

REFERENCES

1. K. Hess, H. Morkoç, H. Shichijo and B. G. Streetman, *Appl. Phys. Lett.* **35**, 469 (1979). The possibility of NDR by a similar mechanism was also discussed by Pacha and Paschke, *Electron. Comm. (AEU)* **32**, 235 (1978). However, their mechanism did not involve layered heterostructures.
2. R. Dingle, H. L. Störmer, A. C. Gossard and W. Weigmann, *Appl. Phys. Lett.* **33**, 665 (1978); L. Esaki and R. Tsu, *IBM Research Report No. RC-2418* (1969).
3. G. H. Döhler, *J. Vac. Sci. Technol.* **16**, 851 (1979).
4. K. Hess, *Appl. Phys. Lett.* **35**, 484 (1979).
5. G. Salardi, B. Pellegrini and T. Di Leo, *Solid-St. Electron.* **22**, 435 (1979).
6. See for example, E. M. Conwell, *Solid-St. Phys. Suppl.* **9**, Academic Press (1967).
7. See for example, K. Seeger, *Semiconductor Physics* Springer-Verlag, Berlin (1973).
8. S. M. Sze, *Physics of Semiconductor Devices*, Chap. 8, Wiley, New York (1969).
9. Hilsum, *Proc. IRE*, **50**, 185 (1962).
10. E. M. Conwell and M. O. Vassel, *Phys. Rev.* **166**, 797 (1968).
11. See Fig. 16 of Ref. [10].
12. See Fig. 14 of Ref. [10].
13. W. Fawcett, A. D. Boardman and S. Swain, *J. Phys. Chem. Solids* **31**, 1963 (1970).
14. T. H. Glisson, J. R. Hauser, M. A. Littlejohn, K. Hess, H. Shichijo and B. G. Streetman, (To be published).
15. C. M. Wu and E. S. Yang, *Solid-St. Electron.* **22**, 241 (1979).

Monte Carlo simulation of real-space electron transfer in GaAs-AlGaAs heterostructures

3

T. H. Glisson, J. R. Hauser, and M. A. Littlejohn

Department of Electrical Engineering, North Carolina State University, Raleigh, North Carolina 27650

K. Hess, B. G. Streetman, and H. Shichijo

Department of Electrical Engineering and Coordinated Science Laboratory, University of Illinois at Urbana-Champaign

(Received 13 March 1980; accepted for publication 11 June 1980)

The Monte Carlo method has been used to simulate electron transport in GaAs/AlGaAs heterostructures with an electric field applied parallel to the heterojunction interface. The simulations indicate that a unique physical mechanism for negative differential conductivity is provided by such layered heterostructures, which is analogous in many respects to the Gunn effect. This mechanism has been termed "real-space electron transfer" since it involves the transfer of electrons from a high-mobility GaAs region to an adjacent low-mobility AlGaAs region as the applied electric field intensity is increased. The simulations further indicate that the important details of the resulting velocity-field characteristics for these layered heterostructures can be controlled primarily through material doping densities, layer thicknesses, and the material properties of the individual layers. Thus, the phenomenon of real-space electron transfer potentially provides the ability to "engineer" those basic material properties which influence the performance of negative resistance devices.

PACS numbers: 72.20.Jv, 72.80.Ey.

I. INTRODUCTION

In a recent paper¹ a new mechanism for obtaining negative differential conductivity in layered heterostructures was described. This mechanism is based on the transfer of hot electrons from high-mobility GaAs layers sandwiched between adjacent low-mobility Al_xGa_{1-x}As layers. The resulting negative differential conductivity is analogous to the Gunn effect, except that the electrons are transferred in real space rather than in momentum space.

To properly describe real-space electron transfer, it is necessary to account for the scattering mechanisms encountered by electrons being transported at high kinetic energies in the potential well in the GaAs, which exists due to the conduction band discontinuity between GaAs and AlGaAs. A mechanical analogy to real-space transfer is provided by the example of a ball rolling down a chute. The ball will stay in the chute if its kinetic energy remains small. However, if the ball gains adequate kinetic energy, then an obstacle can scatter the ball out of the chute. A similar effect occurs in a layered heterostructure where electrons drift in the potential well under the influence of a high electric field. If the mobilities inside and outside the well can be controlled, then the transfer of electrons from the well can be used to control the current-voltage characteristics of the heterostructure device. If the mobility outside the well is much lower than that inside, the effect results in a negative differential conductivity.

In the previous paper,¹ the real-space transfer effect was examined on the basis of "thermionic emission currents"; that is, the densities of electrons inside and outside the well were calculated by balancing the Richardson currents.² In these calculations the layers were treated independently, and energy exchange between the layers was not considered. The

energy distribution of the electrons in both layers was assumed to be Maxwellian, with the GaAs at an elevated temperature T_c and with the temperature in the Al_xGa_{1-x}As assumed to be equal to the lattice temperature T_L . This model has four essential deficiencies: (i) It is well known that at high electric fields the energy distribution functions in polar semiconductors are highly non-Maxwellian. (ii) There is an energy exchange between the layers because energetic carriers are flowing out of the GaAs and cold carriers are returning. (iii) The model does not account for electron temperature gradients or electron-electron interactions. (iv) The complicated band structure of the multilayer heterojunctions (e.g., the role of the L minima in the two materials) was not considered.

It is possible to include (ii) and (iii) in a simple theory using the method of moments.³ This type of calculation is described elsewhere.⁴ The only calculation capable of simultaneously including (i), (ii), and (iv), however, is a Monte Carlo calculation. The purpose of this paper is to describe the results of a Monte Carlo study of real-space transfer in GaAs/AlGaAs layered heterostructures. The Monte Carlo calculations predict a negative differential conductivity for properly chosen heterostructures. The advantage of this negative resistance mechanism over the normal Gunn effect is that all the essential materials parameters can be "engineered". For example, the peak-to-valley ratio can be controlled by the layer width and mobility ratio (including modulation doping⁵), the onset of the negative differential resistance can be controlled by the Al mole fraction (barrier height), and finally the speed of the device can be controlled by the layer thicknesses. We also show that the real-space transfer effect should occur well before the Gunn effect (k -space transfer) for junction barrier heights of approximately 200 meV in GaAs/Al_xGa_{1-x}As heterostructures.

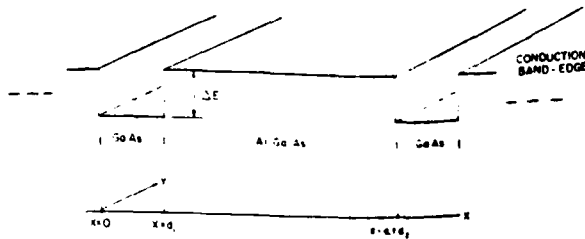


FIG. 1. Material configuration used to simulate real-space transfer.

II. THE TRANSPORT MODEL

The model used in the calculations is classical in the sense that the transport equations are based on the quasiclassical approximation normally employed in the Monte Carlo method.⁷ The essential features of the simulation procedures have been presented previously.⁸⁻¹⁰ These procedures were modified for the present work in order to allow the Monte Carlo method to be applied to the material/device configuration shown schematically in Fig. 1. The model assumes an abrupt potential barrier of height ΔE in the GaAs, and band bending effects are neglected. The electric field created by the ionized donors in the space-charge region of the heterojunction is also neglected. This field tends to attract energetic electrons from the GaAs into the $\text{Al}_x\text{Ga}_{1-x}\text{As}$. Hence it would enhance the transfer out of the well and impede transfer back into the well. This would enhance the negative resistance effect reported here. The importance of the exact nature of the potential barrier will be difficult to ascertain. An exact treatment should of course include a self-consistent calculation of the potential barrier. In practice, however, the ideal potential barrier can be closely approximated by suitable doping profiles and compensation in the AlGaAs.

The well layer thickness d_1 is assumed to be large enough for size quantization effects¹¹ to be neglected. For layer thicknesses greater than 400 Å size quantization effects are not important at room temperature.^{1,4,11} Therefore, these effects are even less important for the hot-electron problem investigated in this work.

Bulk material parameters are used in the simulation of the transport in the two regions of the heterostructure. The parameters for the GaAs have been reported previously.² Their use has resulted in values for both low-field mobility and hot-electron velocity-field characteristics which are in good agreement with experiment. The material parameters for the $\text{Al}_x\text{Ga}_{1-x}\text{As}$ are determined from either measured experimental values or by the use of an interpolation procedure.^{9,10} These parameters depend on the alloy composition x . The value of x is obtained from the desired barrier height ΔE , the known energy-band structure of AlGaAs, and the accepted conduction-band alignment scheme of the GaAs/AlGaAs system.¹¹

The electrons drift in a uniform electric field applied in the y direction parallel to the heterojunction interface. The one-electron simulation begins by releasing an electron from the center of the GaAs well with thermal ($T = 300$ K) energy and in a randomly selected direction. The electron then undergoes scattering interactions in the normal Monte Carlo

framework.⁷⁻¹⁰ The scattering mechanisms considered in these calculations include acoustic-phonon scattering, optical-phonon scattering, piezoelectric scattering, equivalent and nonequivalent intervalley scattering, ionized impurity scattering, and random potential alloy scattering in the $\text{Al}_x\text{Ga}_{1-x}\text{As}$. In the calculations reported here only the $\Gamma(000)$ and L(III) conduction bands are considered for GaAs, and only the $\Gamma(000)$ conduction band is considered in $\text{Al}_x\text{Ga}_{1-x}\text{As}$. This represents adequate band structure details to illustrate the essential features of real-space transfer in GaAs/AlGaAs heterostructures.

The basic heterostructure cell as shown in Fig. 1 is cyclically repeated in the Monte Carlo simulation. This is accomplished in the following manner. An electron which has the correct energetics to transfer from GaAs to AlGaAs across the boundary at $x = 0$ in Fig. 1 is made to enter the AlGaAs at $x = d_1 + d_2$ with the same energetics. Likewise, an electron that transfers from the AlGaAs to GaAs at $x = d_1 + d_2$ is made to enter the GaAs at $x = 0$ with the same energetics. The average drift velocities in the individual materials and the average velocity in the heterostructure are calculated using standard velocity estimators.⁷⁻¹⁰ Since the drift velocity in the AlGaAs is often very low ($\sim 10^5$ – 10^6 cm/sec), the total number of interactions used in the simulation must often be very large ($\approx 250\,000$) in order to obtain accurate velocity estimates.

The transmission of the electrons across the boundary has been modeled in two ways. First, a classical transmission model based on conservation of energy and momentum was used. This requires a particle with inadequate energy to be ideally reflected with no energy loss, with reversal of its momentum perpendicular to the barrier and no change in momentum parallel to the barrier. Second, the quantum-mechanical transmission coefficient described by Wu and Yang¹³ was used in the simulation. Within the statistical error of the simulation no substantial differences in the results have been observed between these two transmission models.

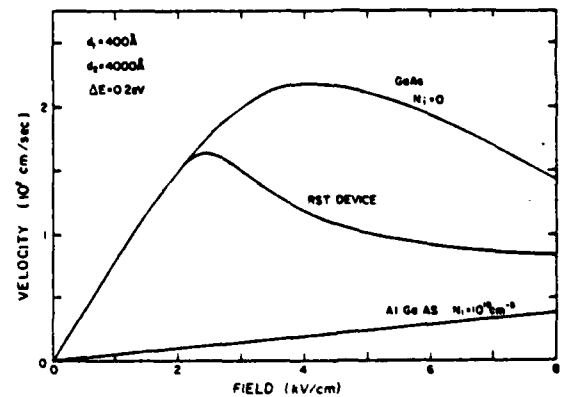


FIG. 2. Velocity-field characteristic for real-space transfer device compared to GaAs and AlGaAs. Here $d_1 = 400$ Å, $d_2 = 4000$ Å, $\Delta E = 0.2$ eV, and $\mu = 8000$ cm²/V sec and 500 cm²/V sec in GaAs and AlGaAs, respectively.

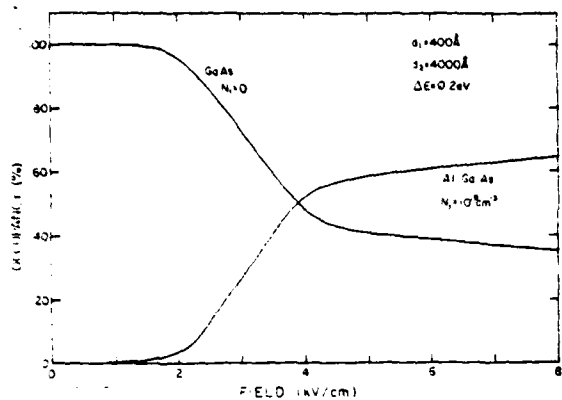


FIG. 3. Relative occupancy of electrons in GaAs and AlGaAs vs field for the same parameters listed in Fig. 2.

Carrier compensation is utilized in order to vary the mobility of electrons in the AlGaAs. The free-electron density in the scattering rate for ionized impurity scattering is taken to be 10^{17} cm^{-3} , while the net ionized impurity density is allowed to vary from 10^{17} cm^{-3} to 10^{20} cm^{-3} . This varies the electron mobility in the AlGaAs from about 4000 to 50 $\text{cm}^2/\text{V sec}$. The low-field mobility in the GaAs is held constant at about 8000 $\text{cm}^2/\text{V sec}$ by taking the ionized impurity density in the GaAs to be zero.¹²

III. SIMULATION RESULTS

The model and procedures described in Sec. II were used to simulate the electron transport in GaAs/AlGaAs heterostructures with various device thicknesses, barrier heights, and other AlGaAs material parameters. Figure 2 shows the steady-state drift velocity of such a structure for the case where the low-field mobility of GaAs is 8000 $\text{cm}^2/\text{V sec}$ and that in AlGaAs is about 500 $\text{cm}^2/\text{V sec}$. Here, the ionized impurity density in AlGaAs is 10^{19} cm^{-3} and the barrier height is 0.2 eV. In this figure the drift velocity in the device structure is compared to that for GaAs and AlGaAs. The transport in AlGaAs remains essentially ohmic for the range of electric fields shown in Fig. 2, although at fields of near 15 kV/cm the transport in the AlGaAs

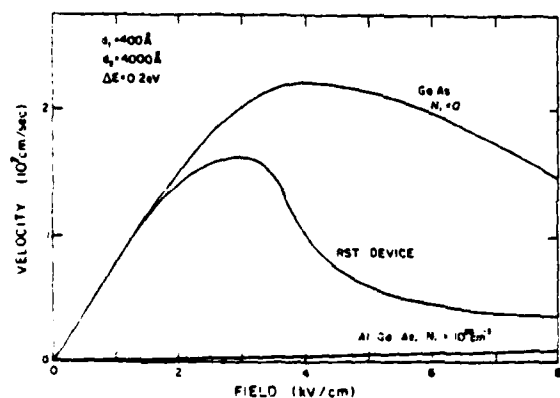


FIG. 4. Velocity-field characteristic for real-space transfer device. All parameters are the same as in Fig. 2, except $\mu = 50 \text{ cm}^2/\text{V sec}$ in AlGaAs.

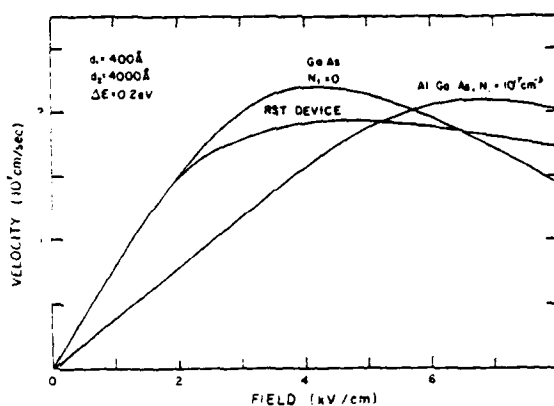


FIG. 5. Velocity-field characteristic for real-space transfer device. All parameters are the same as in Fig. 2, except $\mu = 4000 \text{ cm}^2/\text{V sec}$ in AlGaAs.

would become nonlinear and would eventually exhibit velocity saturation. The peak velocity for the real-space transfer structure is $1.6 \times 10^7 \text{ cm/sec}$ and the threshold field is about 2.4 kV/cm. The onset of electron transfer to the AlGaAs occurs at a field of about 2 kV/cm, as can be seen in Fig. 3. This figure, which shows the relative numbers of electrons in the two adjacent materials, illustrates that for the material thicknesses and barrier height used a substantial number of electrons remain in the GaAs, even for fields well above threshold. The ratio of electrons in the two materials largely determines the peak-to-valley ratio of the real-space transfer device.¹ This is illustrated in Fig. 4 which shows the velocity-field characteristics for the same material parameters as in Fig. 2 except that the AlGaAs mobility is reduced to about 50 $\text{cm}^2/\text{V sec}$. Here the peak velocity is essentially the same as before, although the peak-to-valley velocity ratio has been increased by a factor of 2 (valley taken at 8 kV/cm). In this case, at 8 kV/cm fewer than 10% of the electrons remain in the GaAs. The peak velocity of $1.6 \times 10^7 \text{ cm/sec}$, threshold field of 2.8 kV/cm, peak-to-valley ratio of 4, and a negative mobility magnitude above threshold of greater than $10^4 \text{ cm}^2/\text{V sec}$ in this case are very attractive parameters for Gunn-type device considerations. Figures 2 and 4 support the general features of real-space electron transfer described

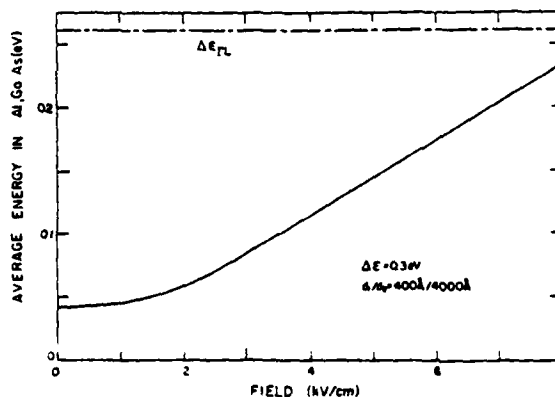


Fig. 6. Average energy in AlGaAs vs electric field for real-space transfer device. All parameters are the same as for Fig. 2, except $\Delta E = 0.3 \text{ eV}$. The Γ -L energy separation in GaAs is shown for comparison.

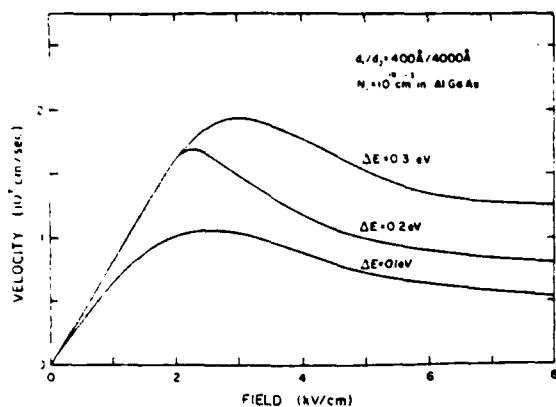


FIG. 7. Velocity-field characteristic for real-space transfer device with barrier height as a parameter. All other parameters are the same as in Fig. 2.

by Hess *et al.* based on the thermionic currents and the method of moments.^{1,4}

Figure 5 shows a velocity-field characteristic when the AlGaAs mobility is $4000 \text{ cm}^2/\text{V sec}$. Here, a substantial number of electrons remain in the GaAs for fields well above 8 kV/cm , and the two materials are equally important in determining the drift velocity in the heterostructure for fields above the threshold field of GaAs. This figure serves to illustrate that a layered heterostructure device might be used to achieve an adjustable velocity-saturation mechanism with very small or negligible negative resistance where the saturation velocity is well above the value normally obtained in silicon or indirect band gap AlGaAs ternary systems. It is worth noting that in Fig. 5 there is a slight negative differential conductivity in the AlGaAs even though only the central Γ valley was used in the simulation. This is due to the non-parabolic nature of the central conduction band; the details of this effect have been discussed previously.¹⁴

Since the threshold field in the heterostructure device is near that for GaAs, an attempt was made to assess the importance of intervalley scattering in the GaAs and AlGaAs on the velocity-field characteristic of the structure. The satellite L (III) valley in GaAs was removed from the simulation model, and the velocity-field characteristics were calculated for barrier heights up to 0.3 eV , which is near the Γ - L intervalley separation for GaAs proposed by Aspnes.^{12,15} Within the statistical accuracy of the velocity estimator no differences could be observed in the results compared to those given in Fig. 2. In addition, Fig. 6 shows the average energy of the electrons in the AlGaAs as a function of electric field for a barrier height of 0.3 eV compared to the Γ - L energy separation in the AlGaAs. For this case between 2 and 4 kV/cm the average energy is well below the intervalley energy separation, although the electrons are becoming hot. At higher electric fields ($\sim 8 \text{ kV/cm}$) intervalley scattering in the AlGaAs will be important and will probably affect the peak-to-valley ratio, although it appears to influence neither the threshold field nor the peak velocity. Further studies are underway to examine the importance of scattering in the L and X valleys of AlGaAs.

Further aspects of the phenomenon of real-space trans-

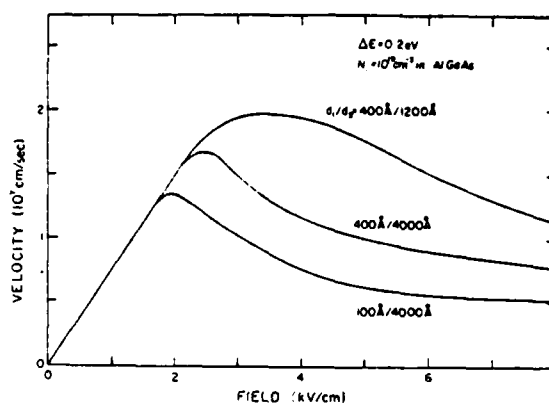


FIG. 8. Velocity-field characteristic for real-space transfer device with AlGaAs thickness as a parameter. All other parameters are the same as in Fig. 2.

fer are shown in Fig. 7. This figure illustrates the influence on the heterostructure velocity-field characteristics of varying the barrier height while maintaining fixed material thicknesses. Obviously, as the barrier height increases, the velocity-field characteristic approaches that for lightly doped GaAs. This is the expected behavior, although one might expect some additional influence if the layers are thin enough for size quantization effects to be important. In addition, the form of scattering at the GaAs/AlGaAs interface could effect the electron transport in the GaAs well material. In this paper specular interface scattering has been used. Thus, the energy and momentum relaxation mechanisms in the well material are the same as those an electron would encounter in bulk GaAs. Future studies of real-space transfer will include size quantization effects and other physical forms of interface scattering.

As the barrier height decreases in the real-space transfer simulation model, the velocity-field characteristic is increasingly influenced by the heavily compensated $\text{Al}_{1-x}\text{Ga}_x\text{As}$. Physically, for the material systems used here, as the barrier height decreases x approaches unity. Thus, the device would consist of alternating layers of thin, lightly doped GaAs and thicker, heavily compensated

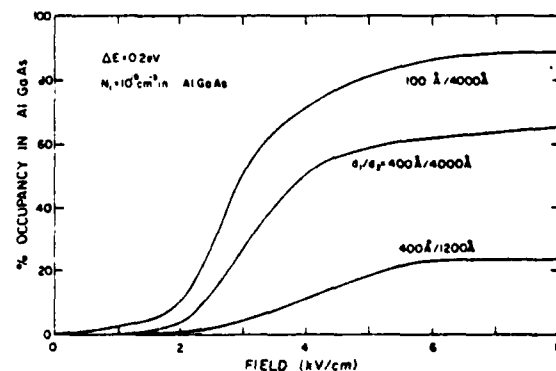


FIG. 9. Relative occupancy of electrons in AlGaAs thickness as a parameter, as a function of electric field. All other parameters are the same as in Fig. 2.

GaAs. For all practical purposes, the resultant velocity-field characteristic would be dominated by the heavily compensated GaAs. In Fig. 7, the free-electron density is 10^{17} cm^{-3} and the ionized impurity density is 10^{19} cm^{-3} . The results in this figure for a barrier height of 0.1 eV are consistent with these conclusions based on our own calculations on bulk, heavily compensated GaAs, and with other calculations on more heavily doped GaAs.¹⁶

It appears that for a given materials system there will be an optimum barrier height for most effectively utilizing real-space transfer in a given device application. For the GaAs/AlGaAs system studied in this paper, a barrier height in the vicinity of 0.2 eV results in an attractive set of material parameters for consideration for negative resistance devices.

Figure 8 shows the influence of respective layer thickness on the velocity-field characteristics of the layered heterostructure. Figure 9 shows the occupancy in the AlGaAs as a function of the electric field intensity. Again, the influence of size quantization has not been included and could influence the results for GaAs layer thicknesses of 100 Å. The purpose of these last two figures is to show in a qualitative manner the way in which simple geometric changes can be used to control the transport properties of a layered heterostructure.

IV. SUMMARY AND CONCLUSIONS

The Monte Carlo simulations presented here have validated the general features of the phenomenon of real-space electron transfer discussed and examined by Hess and co-workers at the University of Illinois.¹⁻⁴ The simulation model presented here has included the important scattering processes and energy exchange mechanisms between the two adjacent materials in layered heterostructures. It predicts that real-space transfer provides a mechanism for negative differential conductivity that is analogous to the Gunn effect, but which is different from it to the extent that the nature of the mechanism can be "engineered" by the materials and device designer. This includes the control of the important parameters such as velocity-field characteristic and speed of response. The work discussed here is now being

extended to the investigation of other practical materials systems and to the inclusion of other important physical mechanisms such as size quantization, interface effects, heavy doping effects, and electron-electron interactions.

ACKNOWLEDGMENTS

The authors wish to thank the Department of Defense for financial support of this work through the Joint Services Electronics Program (U.S. Army, U.S. Navy, U.S. Air Force) under Contract No. N00014-79-C-0424, the Office of Naval Research under Contract Nos. N00014-76-C-0768, N00014-76-C-0806, N00014-76-C-0480, and the U.S. Army Research Office under Contract No. DAAG29-79-D-1003.

¹K. Hess, H. Morkoc, H. Shichijo, and B. G. Streetman, *Appl. Phys. Lett.* **35**, 469 (1979).

²See for example S. M. Sze, *Physics of Semiconductor Devices* (Wiley, New York, 1969).

³K. Seeger, *Semiconductor Physics* (Springer, Wein, 1973).

⁴H. Shichijo, K. Hess, and B. G. Streetman, *Solid-State Electron.* (to be published).

⁵R. Dingle, H. L. Störmer, A. C. Gossard, and W. Wiegmann, *Appl. Phys. Lett.* **33**, 665 (1978).

⁶G. H. Wannier, *Elements of Solid State Theory* (Cambridge, London, 1960).

⁷T. Kurosawa, Proceedings of the International Conference Physics Semiconductors, Kyoto, 1966 (unpublished); *J. Phys. Soc. Jpn. Suppl.* **21**, 424 (1966).

⁸M. A. Littlejohn, J. R. Hauser, and T. H. Glisson, *Appl. Phys. Lett.* **26**, 625 (1975).

⁹J. R. Hauser, M. A. Littlejohn, and T. H. Glisson, *Appl. Phys. Lett.* **28**, 458 (1976).

¹⁰M. A. Littlejohn, J. R. Hauser, and T. H. Glisson, *Appl. Phys. Lett.* **30**, 242 (1977).

¹¹R. Dingle in *Festkörper-Probleme XV (Advances in Solid State Physics)*, edited by A. V. Queisser, Pergamon-Vieweg, Brunschweig, 1976, pp. 21-48.

¹²M. A. Littlejohn, J. R. Hauser, and T. H. Glisson, *J. Appl. Phys.* **48**, 4587 (1977).

¹³C. M. Wu and E. S. Yang, *Solid-State Electron.* **22**, 241 (1979).

¹⁴J. R. Hauser, T. H. Glisson, and M. A. Littlejohn, *Solid-State Electron.* **22**, 487 (1979).

¹⁵D. E. Aspnes, *Phys. Rev. B* **14**, 5331 (1976).

¹⁶J. G. Ruch and W. Fawcett, *J. Appl. Phys.* **41**, 3843 (1970).

Measurements of hot-electron conduction and real-space transfer in GaAs-Al_xGa_{1-x}As heterojunction layers

4

M. Keever, H. Shichijo, K. Hess, S. Banerjee, L. Witkowski, H. Morkoç, and B. G. Streetman

Department of Electrical Engineering and the Coordinated Science Laboratory, University of Illinois at Urbana-Champaign, Urbana, Illinois 61801

(Received 25 August 1980; accepted for publication 16 October 1980)

Measurements of the current-voltage characteristics of GaAs-Al_xGa_{1-x}As heterojunction layers are reported. The experimental results are consistent with the idea of real-space transfer of the electrons out of the GaAs into the Al_xGa_{1-x}As under hot-electron conditions. Current saturation and negative differential resistance are observed as predicted by Monte Carlo simulations.

PACS numbers: 72.20.Ht, 73.40.Lq

Electronic transport in semiconductor heterojunction layers has attracted considerable interest since Dingle and co-workers verified mobility enhancement in modulation-doped structures.¹ Such enhancement occurs when electrons leave their parent donors (e.g., in the Al_xGa_{1-x}As) and transfer to a neighboring undoped layer which has a smaller band gap (e.g., GaAs). Thus the electrons will not be scattered strongly by the remote impurities (donors) and the mobility in the GaAs will be enhanced. Although there are some subtleties, including an enhanced phonon scattering rate,² this improved mobility is reflected by the experiments.

Theoretical investigations of high-field transport in these layers led Hess *et al.* to conclude that when a high electric field is applied parallel to the layer interfaces the inverse process takes place, namely a transfer of electrons from the GaAs layers back into the Al_xGa_{1-x}As layers.³ This process can be viewed as the thermionic emission of hot electrons, and has simple mechanical analogies.⁴ A Monte Carlo simulation of the real-space trajectory of an electron for a double heterojunction of Al_xGa_{1-x}As ($x = 0.17$) is shown in the inset of Fig. 1. After some reflections an electron in the GaAs layer gains enough kinetic energy from the applied electric field to move out of the potential well caused by the band-gap difference between the two materials. More exact treatments of this effect including quantum-mechanical transmission coefficients do not reveal new features for this picture.⁴ The movement of the hot electrons back into the low-mobility Al_xGa_{1-x}As material will of course lead to a nonlinear behavior in the current density. Figure 1 shows the current-voltage characteristic of the double-heterojunction structure shown in the inset. These results were obtained from Monte Carlo calculations.⁴ The magnitude of the negative differential resistance in such a curve depends on the doping densities which control the free-carrier concentrations and mobilities in the Al_xGa_{1-x}As and GaAs layers. A very high doping density in the Al_xGa_{1-x}As causes a high concentration of scattering centers, which results in a very low mobility and high resistance in the Al_xGa_{1-x}As and therefore can yield large peak-to-valley ratios, larger than those observed in the Gunn effect, which is based on the k -space analog of the mechanism de-

scribed here.

In this letter we report measurements of the high-field characteristics of Al_xGa_{1-x}As structures grown by molecular beam epitaxy (MBE). The doping density in the Al_xGa_{1-x}As layers was $N_D \approx 10^{17} \text{ cm}^{-3}$ and the GaAs was not intentionally doped. The mobility in the GaAs layers was enhanced over the bulk value for equivalent doping and was typically $2 \times 10^4 \text{ cm}^2/\text{Vs}$ at 77 K. The mobility in the Al_xGa_{1-x}As layers was around $1000 \text{ cm}^2/\text{Vs}$ between 300 and 77 K. The doped Al_xGa_{1-x}As layer was 1000 Å thick in all cases, whereas the GaAs layers varied in thickness from 400 Å to $\sim 1.0 \mu\text{m}$. In some of the samples the GaAs layer was sandwiched between the doped and a second (undoped) Al_xGa_{1-x}As layer. Because of the pulling force of the donors we think that the actual width of the GaAs layer is relatively unimportant, since the electrons in the GaAs will always be within 1000 Å of the doped Al_xGa_{1-x}As layer. Although x was 0.17 for most of the data reported here, we have made similar measurements with x increased to 0.25. Au-Ge contacts were evaporated on top of the layer (top layer Al_xGa_{1-x}As) and alloyed by heating at a rate of 400 °C/min in flowing H₂ to a final temperature of 450 °C. Contacts formed in this way proved to be ohmic in most cases. The distance between the contacts was 0.065 cm and the width of the samples was about 0.1 cm. Measurements were performed using short current pulses. The measurements were taken at times between 1 and 600 ns. The samples were mounted in GR insertion units and the usual 50-Ω sampling oscilloscope x - y recorder technique was used.⁵ Below we report five groups of results:

(i) Unusually strong acoustoelectric sound amplification and accompanying negative differential resistance (inset Fig. 2) was observed in some samples at 77 K at very low electric fields of about 300 V/cm having incubation times as low as ~ 3 ns. This effect did not occur at room temperature (the samples were too short) and was not observed in any of the samples for which results are reported below. A detailed report will be given in a subsequent publication.

(ii) In samples not showing the acoustoelectric effect (about 40 samples from 5 wafers) onset of current saturation or slight negative differential resistance was observed at an

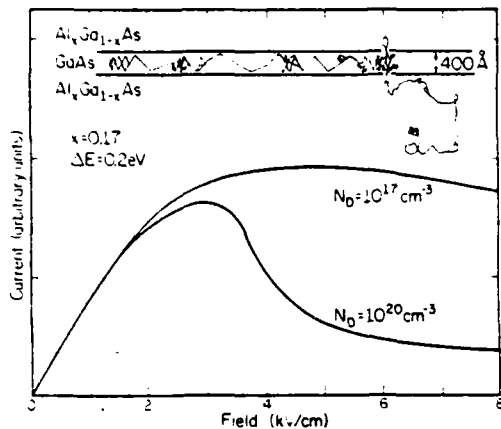


FIG. 1. Current-field characteristics for the double-heterostructure shown in the inset with Al_xGa_{1-x}As densities of 10^{17} cm^{-3} ($\mu = 4000 \text{ cm}^2/\text{V s}$) and 10^{20} cm^{-3} ($\mu = 50 \text{ cm}^2/\text{V s}$). The thickness of the AlGaAs layer is 4000 Å and the GaAs is 400 Å thick and has $\mu = 8000 \text{ cm}^2/\text{V s}$ in both cases. The inset shows a Monte Carlo simulation of the path of an electron when a high electric field is applied parallel to the layer interfaces.

electric field of 2000–3200 V/cm at room temperature and also at 77 K. Representative examples are given in Figs. 2 and 3. The consistency of the occurrence of negative differential resistance at these fields makes us believe that contact effects do not strongly influence our experimental results.

(iii) Figure 2 also shows the onset of a second (third if the acoustoelectric effect is counted) negative differential resistance, marked by the second arrow. We believe that this may be due to trapping in surface states when electrons finally spill to the unprotected surface. The effect is apparently slow and shows hysteresis.

(iv) We performed photoconductivity measurements using the 6328-Å line of a He-Ne laser. The result exhibited by six samples is shown in Fig. 3. The low-field conductance is slightly increased by the light but the high-field conductance is strongly decreased, thus enhancing the negative differential resistance. A natural explanation is that the light

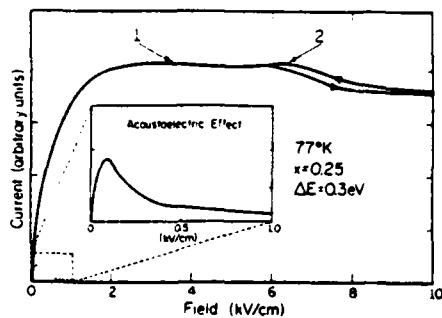


FIG. 2. Current-field characteristic showing a second negative differential resistance (marked by second arrow) believed to be due to trapping in surface states. The first arrow marks the negative differential resistance thought to be caused by real-space transfer. In the Al_xGa_{1-x}As, $N_D = 2 \times 10^{17} \text{ cm}^{-3}$. The thickness of the undoped GaAs layer is 2.0 μm. The inset shows a current-field curve exhibiting an acoustoelectric effect where the Al_xGa_{1-x}As (0.15 μm thick) has $N_D = 3 \times 10^{16} \text{ cm}^{-3}$ and the GaAs (1.6 μm thick) is not intentionally doped.

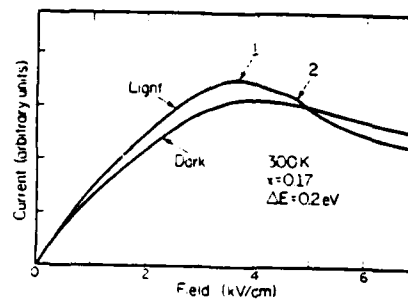


FIG. 3. Current-field characteristics demonstrating an enhanced negative differential resistance at 300 K when the sample is illuminated with a He-Ne laser. Note the second negative differential resistance at arrow 2. The Al_xGa_{1-x}As layer is 1000 Å thick and has $N_D = 6 \times 10^{17} \text{ cm}^{-3}$. The GaAs layer is 1 μm thick and is not intentionally doped.

empties traps in the Al_xGa_{1-x}As and increases the low-field conductivity. The traps are filled again when the hot electrons transfer back to the Al_xGa_{1-x}As, thus increasing the peak-to-valley ratio of the curve and decreasing the high-field conductivity. Note also the close agreement of the dark curve in Fig. 3 with the Monte Carlo simulations ($N_D \approx 10^{17} \text{ cm}^{-3}$) of Fig. 1.

(v) Our knowledge of carrier concentration and mobility was obtained from Hall effect data, which reflect average concentrations and mobilities. Additional information can be obtained from the hot-electron results by assuming a value of $\sim 10^7 \text{ cm}^2/\text{V s}$ for the peak velocity. Nevertheless, the exact concentration and its spatial variation is hard to determine. Therefore, in some cases our samples showed mainly conduction in the Al_xGa_{1-x}As, which was in these cases too highly doped to be depleted. (The built-in fields prevent complete transfer of all the electrons to the GaAs.) Some of these samples showed a fourth kind of negative differential resistance at about 10^4 V/cm due to the Gunn effect in the Al_xGa_{1-x}As and also exhibited oscillations. By etching away part of the Al_xGa_{1-x}As layers, depletion of the Al_xGa_{1-x}As could be achieved, and negative differential resistance was again observed around 3000 V/cm. This experiment also gave another estimate of the doping from the known depletion width, which was obtained from the etch-

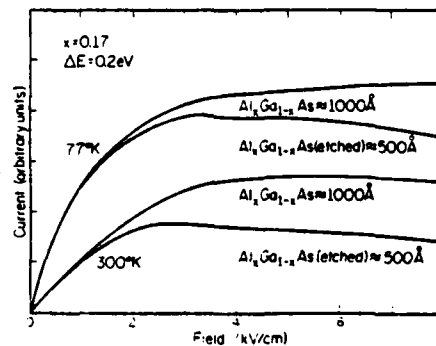


FIG. 4. Current-field characteristics showing the occurrence of negative differential resistances at 300 and 77 K when the Al_xGa_{1-x}As layer thickness is reduced. The Al_xGa_{1-x}As layer was doped at $N_D = 6 \times 10^{17} \text{ cm}^{-3}$ and the undoped GaAs layer was 1 μm thick.

ing rate. A representative example is shown in Fig. 4. The relative change in peak velocity between 77 and 300 K agrees roughly with Monte Carlo simulations.⁶

From the above experiments we conclude that the negative differential resistance around the electric field of 3000 V/cm is consistent with the idea of real-space electron transfer. The effect is different from the effect of k -space transfer [the Ridley-Watkins-Hilsum (RWH) mechanism]. The distinction from the RWH effect in $\text{Al}_x\text{Ga}_{1-x}\text{As}$ is demonstrated by the etching experiment of Fig. 4. Negative differential resistance due to k -space transfer in GaAs is also different from the effect described here. The threshold voltage is somewhat higher for the RWH mechanism, but this could also be caused by the higher mobility and contact effects in our samples. However, the Monte Carlo simulations⁴ show that for $x < 0.17$ (where the band-gap difference is smaller than the energy separation to the satellite minima) the electrons move out of the GaAs long before they can populate higher valleys. Furthermore, the photoconductive enhancement of the negative differential resistance (Fig. 3) does not occur for the RWH effect and can not be simply explained without the transfer of electrons out of the GaAs. We have never observed Gunn oscillations connected with the negative differential resistance at 3000 V/cm. The reason for this is not entirely understood. However, we can point out the following distinct differences between real-space transfer and the RWH mechanism. There is no local microscopic negative differential resistance in the $\text{Al}_x\text{Ga}_{1-x}\text{As}$ at the electric fields considered. Accumulation (and therefore dipole) domains cannot be formed because accumulating electrons would be emitted out of the GaAs. The total lack of any kind of instability, however, does not necessarily follow from these arguments and might be connected with fixed interface inhomogeneities at which the electrons spill out first.

The speed of the effect could not be determined with the present experimental arrangement. We can only say that the effect is faster than 1 ns. Our measurements below 1 ns were hampered by parasitic capacitances possibly caused by the layered structure itself. Finally, we would like to mention that the peak-to-valley ratio of the current-voltage characteristic will depend strongly on the electron mobility of the

$\text{Al}_x\text{Ga}_{1-x}\text{As}$. To obtain high peak-to-valley ratios, the mobility in the $\text{Al}_x\text{Ga}_{1-x}\text{As}$ should be around 100 and > 5000 $\text{cm}^2/\text{V s}$ in the GaAs. In order to allow simultaneously for depletion of the $\text{Al}_x\text{Ga}_{1-x}\text{As}$, highly compensated material is needed. If low mobilities in compensated material can be achieved without introducing deep traps, the resulting negative differential resistance should have a peak-to-valley ratio much larger than that achievable by the RWH mechanism.

For assistance in portions of this work we wish to thank Susan Brennecke, Bob McFarlane, and R. T. Gladin. We are particularly grateful to N. Holonyak, Jr. for many valuable discussions and to A. Y. Cho for assisting the MBE program. We also thank M. A. Littlejohn, T. H. Glisson, and J. R. Hauser of North Carolina State University (Raleigh) for providing us with the Monte Carlo stimulation results. The work has been supported primarily by the Office of Naval Research, Contract No. N000-14-79-C-0768, and the Army Research Office, Contract No. DAAG-19-80-C-0011. The crystal growth facilities have been supported by the Air Force Office of Scientific Research, Contract No. AFOSR-80-0084, and the Joint Services Electronics Program, Contract No. N000-14-79-C-0429.

¹The idea of modulation doping, introduced by L. Esaki and R. Tsu (IBM Research Report No. RC-2418, 1969 (unpublished), was first demonstrated by R. Dingle, H. L. Stormer, A. C. Gossard, and W. Wiegmann [Appl. Phys. Lett. 33, 665 (1978)].

²K. Hess, Appl. Phys. Lett. 35, 484 (1979).

³K. Hess, H. Morkoc, H. Shichijo, and B. G. Streetman, Appl. Phys. Lett. 35, 469 (1979).

⁴T. H. Glisson, J. R. Hauser, M. A. Littlejohn, K. Hess, B. G. Streetman, and H. Shichijo, J. Appl. Phys. 51, 5445 (1980). See also H. Shichijo, K. Hess, and B. G. Streetman, Solid-State Electron. 23, 817 (1980).

⁵K. Hess, A. Neugroschel, C. C. Shiu, and C. T. Sah, J. Appl. Phys. 46, 1721 (1975).

⁶T. H. Glisson, J. R. Hauser, and M. A. Littlejohn (private communication).

Simulation of high-field transport in GaAs using a Monte Carlo method and pseudopotential band structures

H. Shichijo, K. Hess, and G. E. Stillman

Department of Electrical Engineering and Coordinated Science Laboratory, University of Illinois at Urbana-Champaign Urbana, Illinois 61801

(Received 15 August 1980; accepted for publication 16 October 1980)

We have performed a Monte Carlo simulation of high-field transport in GaAs using a realistic band structure obtained by the empirical pseudopotential method. On this basis, a detailed study of the band structure dependence of impact ionization in GaAs is given. Our method avoids the use of the effective mass theorem or the Kane model of nonparabolicity, which are no longer accurate at high electron energies. We show (i) that the orientation dependence of the impact ionization rate is negligibly small, (ii) that the saturation velocity of electrons in GaAs is close to 6×10^6 cm/s at extremely high fields (this value is determined to a large extent by the band structure, and (iii) that the previous theories of impact ionization as given by Wolff, Shockley, and Baraff have numerous limitations.

PACS numbers: 72.20.Ht, 72.10. — d, 79.20.Hx, 85.30.De

Impact ionization and other high-field phenomena¹ are of considerable interest because many semiconductor devices are based on high-field effects (avalanche photodiodes, IMPATT diodes, Gunn diodes) or necessarily involve them in their operation and are limited because of them (charge coupled devices, field effect transistors). In spite of the urgent need, a rigorous theory for electronic transport above about 5×10^4 V/cm has not been developed. The main reason for this is that any theory applicable at high electric field must include a realistic band structure and abandon the effective mass approximation or simple extensions using the *k*-*p* method to allow for nonparabolicity.²

Surprisingly enough, for specific quantities (such as the impact ionization rate) successful phenomenological theories have been given without including the band structure. These theories developed by Wolff,³ Shockley,⁴ Baraff,⁵ Dumke,⁶ and Chwang *et al.*⁷ fail, however, when used to calculate other transport quantities or when applied to different materials. Dumke's theory is only applicable to InSb or InAs, whereas Wolff's, Baraff's, and Chwang's treatments are only valid for nonpolar materials. The reason for the partial success of theories³⁻⁷ is that adjustable parameters

are used, which can successfully "absorb" the band-structure effects on the field dependence of the impact ionization rate, but do not "absorb" these effects for other transport quantities. Effects of crystal orientation can not be practically treated by these theories at all. The reason is that the inclusion of the band structure in analytical solutions of the Boltzmann equation is impractical, if not impossible.

The Monte Carlo method provides an alternative to the solution of the Boltzmann equation. This method can be used to calculate the impact ionization rate,^{8,9} the drift velocity, and other quantities of interest without any *a priori* assumptions on the form of the distribution function. The Monte Carlo method can also take into account a large variety of scattering mechanisms and, therefore, is applicable to both polar and nonpolar semiconductors. In this letter we report the use of the Monte Carlo method with a realistic band structure as calculated by the empirical pseudopotential method¹⁰ for the calculation of high-field transport. The numerical procedure is as follows. The *E*(*k*) relation and its gradients (velocity) have been calculated using the 48-fold symmetry of the Brillouin zone (156 mesh points in the 1/48 part of the zone). The *E*(*k*) relation for an arbitrary *k* vector

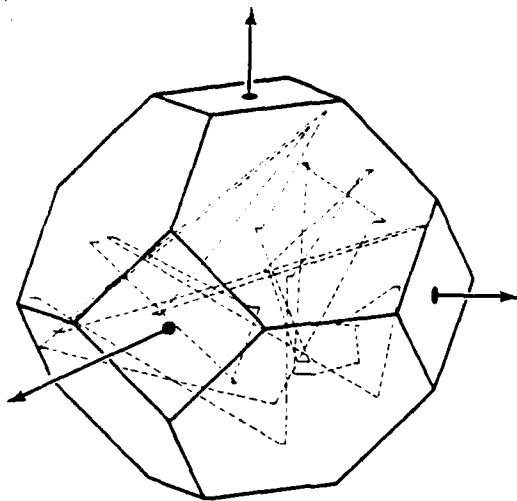


FIG. 1. Typical trajectory of the electron k vector in the Brillouin zone for an electric field of 500 kV/cm. The solid lines represent the drifts and the broken lines represent the scatterings from one point to the next.

can then be calculated by quadratic interpolation. Only the lowest conduction band (over the whole Brillouin zone) has been used for the simulations. Tunneling to upper bands has been neglected because of the much smaller probability of tunneling as compared to the probability of phonon scattering.¹¹ Next we need to know the phonon scattering rate. The scattering rates in GaAs for energies below 1.0 eV are well known from the study of the Gunn effect.¹² We have used the same parameters as given by Littlejohn *et al.*¹³ Not much is known, on the other hand, about the scattering rate above 1.0 eV. Here we have assumed a quadratically decreasing scattering rate above 1.5 eV because the intervalley scattering rate is proportional to the density of final states, and the density of states in the conduction band decreases above 1.5 eV.¹⁴ The rate varies from $4.5 \times 10^{14} \text{ s}^{-1}$ at 1.5 eV to $2.5 \times 10^{14} \text{ s}^{-1}$ at 2.5 eV. For simplicity we have assumed the scattering rate to be isotropic, and the overlap integrals¹⁵ are assumed to be unity. This overestimates the scattering rate in the satellite valleys. However, since scattering to upper bands is possible in reality, (which increases the scattering

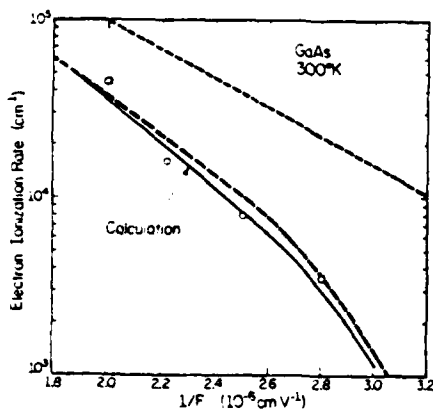


FIG. 2. Calculated electric field dependence of the electron initiated impact ionization rate in GaAs. The shaded region indicates the range of available experimental data. (See Refs. 17 and 18).

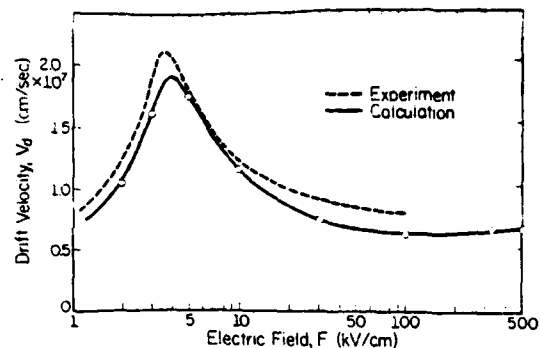


FIG. 3. Calculated electron drift velocity in GaAs at room temperature compared with the experimental data. (See Refs. 19 and 20).

rate in the satellite valleys), the overestimation is at least partly compensated.

The final state of the scattering process is determined in the following way. Since polar optical scattering is dominant only at low energies in the central valley, the usual formula with effective mass and nonparabolicity terms is used to choose a candidate for the final k point. The energy at this k point is then recalculated using the exact band structure to check if it is within an allowed range ($\sim 30 \text{ meV}$) around the final energy ($E + \hbar\omega_0$ in the case of phonon absorption). If it is outside this range, a different final state is chosen, and the process is repeated until a proper state with correct energy is found. Intervalley scattering is known to be completely randomizing.¹ For this mechanism, once the final energy is calculated, those mesh points, whose energies are within the allowed range, are tabulated. One of them is then randomly selected as the final state.

Our treatment of phonon scattering processes represents a compromise between accuracy and numerical tractability. In the limit of infinitely fine mesh points (instead of 156 points in $1/48$ of the Brillouin zone) and infinitely small allowed final energy range (instead of 30 meV) the procedure is basically correct as the scattering rate for deformation potential scattering is proportional to the final density of states.

The impact ionizing collision is treated as an additional scattering mechanism. We assume an isotropic threshold energy of 2.0 eV. According to Keldysh,¹⁶ the probability of impact ionization can be represented as

$$\frac{1}{\tau_i(E)} = \frac{1}{\tau(E_i)} P \left(\frac{E - E_i}{E_i} \right)^2, \quad (1)$$

where E is the electron energy, E_i is the threshold energy, $1/\tau(E_i)$ is the scattering rate at $E = E_i$, and P is a dimensionless constant which is generally much larger than unity. This formula is valid for semiconductors with large dielectric constants. We insert $P = 400$.⁷ A more rigorous treatment must involve the calculation of the matrix element for the screened Coulomb interaction.⁹

The simulation then starts by releasing an electron with zero energy at the bottom of the central valley. The motion of an electron during the drift is determined by the equations of motion

$$\hbar \frac{dk}{dt} = eF, \quad (2)$$

$$v = \frac{1}{\hbar} \nabla_k E, \quad (3)$$

where F is an electric field vector, and v is the electron velocity in real space. The drift time and the scattering events are determined by random numbers as in conventional Monte Carlo methods. When impact ionization occurs, the energy of an electron is reinitialized to zero. The impact ionization rate can be obtained by averaging the distance to impact ionization over a sufficient number of ionizations. Each distance traveled during the drift is calculated either by accumulating a differential distance, $v\Delta t$, or by utilizing the relation

$$\Delta E = eF\Delta x, \quad (4)$$

where ΔE is the energy gained during the drift.

Figure 1 shows a typical trajectory of the k vector in the Brillouin zone for an electric field of 500 kV/cm in the $\langle 100 \rangle$ direction. The solid lines represent the drift of the electron, and the broken lines represent the scatterings from one point to another. When the k vector lies outside of the Brillouin zone, it is placed back to the equivalent point inside the zone. A typical simulation consists of approximately 100,000–200,000 scattering events.

The calculated electric field dependence of the impact ionization rate in GaAs is shown in Fig. 2. The shaded region indicates the range covered by the currently available experimental data.^{17,18} The agreement is fairly good considering the uncertainty in the scattering rate at higher energies. The inclusion of upper bands is expected to increase the calculated ionization rate slightly. Within statistical fluctuations ($\sim 20\%$) we do not see any orientation dependences of the ionization rate. This contradicts the experimental data by Pearsall *et al.*,¹⁸ who found that the ionization rate differs in various crystal directions by almost an order of magnitude at lower fields.

Figure 3 shows the electron drift velocity in GaAs calculated by our method. The broken curve represents the experimental data.^{19,20} The agreement is good in the whole range of electric fields which has been investigated experimentally. The slight deviations between theory and experiment are believed to be mainly due to the pseudopotential band structure which gives the effective masses at the Γ , X , and L valleys larger than are usually measured. In Fig. 3 it can also be seen that the calculations describe quantitatively the Gunn effect. Both X and L valleys are of course automatically included.

These are three major results which have been obtained with one set of material constants. We now describe briefly some other results of more qualitative nature. We have learned that the electrons are not at all drifting mainly in the direction of the electric field; they are frequently scattered practically all over the Brillouin zone (Fig. 1). The electrons move over relatively long time periods perpendicular to the external fields because of Bragg reflection at energies above 1 eV. Moreover, we find hardly any "lucky" electrons which totally escape the phonon scattering. This contradicts some

of Shockley's ideas of impact ionization. Shockley's "lucky" electrons start from zero energy, escape the phonon scattering, and impact ionize. We find instead that the electrons stay around an average energy of typically 0.8 eV (for the case of 500 kV/cm) and experience a large number of scattering events. Once in a while electrons escape the phonon scattering events and move up to higher energy. Then if they are lucky enough they reach ionization threshold after a few (typically three to five) scattering events. In view of these facts the question arises why the previous theories^{3–6} of impact ionization are so successful and which one is the closest to the truth? For instance, Shockley's physical arguments linking the number of phonon scatterings and the probability to impact ionize are reflected also by our simulations. The quantitative success of previous theories, however, is connected with the large number of adjustable parameters.

Our method can, of course, be applied to any semiconductor. The calculations, however, can be costly and time consuming. The above simulation takes about an hour of CPU time on a DEC-20 for each value of the electric field. However, the efficiency of the program has not yet been optimized. Finally, we would like to note that the problem of hot electron emission from silicon into silicon dioxide²¹ over a potential barrier of ~ 3 eV certainly needs the inclusion of a realistic band structure. Calculations on this problem are in progress.

We would like to thank N. Alparelli for his help with the band-structure calculations. This work was supported by the Office of Naval Research under Contract No. N00014-79-C-0768 and the Joint Services Electronics Program under Contract No. N00014-79-C-0424. The use of the computer facilities of the Materials Research Laboratory, University of Illinois, under Contract No. DMR 77-23999 is also gratefully acknowledged.

¹E. M. Conwell, *High Field Transport in Semiconductors in Solid State Physics*, Suppl. 9 (Academic Press, New York, 1967).

²E. O. Kane, *Semiconductors and Semimetals*, Vol. 1, edited by R. K. Willardson and A. C. Beer (Academic Press, New York, 1966).

³P. A. Wolff, *Phys. Rev.* **95**, 1415 (1954).

⁴W. Shockley, *Solid-State Electron.* **2**, 35 (1961).

⁵G. A. Baraff, *Phys. Rev.* **128**, 2507 (1962).

⁶W. P. Dumke, *Phys. Rev.* **167**, 783 (1968).

⁷R. Chwang, C. W. Kao, and C. R. Crowell, *Solid-State Electron.* **22**, 599 (1979).

⁸P. A. Lebowitz and P. J. Price, *Solid State Commun.* **9**, 1221 (1971).

⁹R. C. Curby and D. K. Ferry, *Phys. Status. Solidi (A)* **15**, 319 (1973).

¹⁰M. L. Cohen and T. K. Bergstresser, *Phys. Rev. B* **141**, 789 (1966).

¹¹H. D. Law and C. A. Lee, *Solid State Commun.* **21**, 331 (1978).

¹²W. Fawcett, A. D. Boardman, and S. Swain, *J. Phys. Chem. Solids* **31**, 1963 (1970).

¹³M. A. Littlejohn, J. R. Hauser, and T. H. Glisson, *J. Appl. Phys.* **48**, 4587 (1977).

¹⁴J. R. Chelikowsky and M. L. Cohen, *Phys. Rev. B* **14**, 556 (1976).

¹⁵D. Matz, *Phys. Rev.* **168**, 843 (1968).

¹⁶L. V. Keldysh, *Sov. Phys. JETP* **21**, 1135 (1965).

¹⁷G. E. Stillman and C. M. Wolf, *Semiconductor and Semimetals*, Vol. 12, edited by R. K. Willardson and A. C. Beer (Academic Press, New York, 1977).

¹⁸T. P. Pearsall, F. Capasso, R. E. Nahory, M. A. Pollack, and J. R. Chelikowsky, *Solid-State Electron.* **21**, 297 (1978).

¹⁹J. G. Ruch and G. S. Kino, *Phys. Rev.* **174**, 921 (1968).

²⁰P. A. Houston and A. G. R. Evans, *Solid-State Electron.* **20**, 197 (1977).

²¹T. H. Ning, *Solid-State Electron.* **21**, 273 (1978).

6

Band-structure-dependent transport and impact ionization in GaAs

H. Shichijo and K. Hess

*Department of Electrical Engineering and Coordinated Science Laboratory,
University of Illinois at Urbana-Champaign, Urbana, Illinois 61801*

(Received 14 October 1980)

We have performed a Monte Carlo simulation of high-field transport in GaAs including a realistic band structure to study the band-structure dependence of electron transport and impact ionization. The band structure has been calculated using the empirical pseudopotential method. Unlike previous theories of impact ionization, our method is capable of calculating various parameters, such as mean free path, from first principles. The calculated electron mean free path, drift velocity, and impact ionization rate are in reasonable agreement with the experimental data in spite of several simplifications of the model. Within statistical uncertainty we do not observe any orientation dependence of the ionization rate in contradiction to the interpretation of recently reported experimental results. We also find that the contribution of ballistic electrons to impact ionization is negligibly small. Based on the results of the calculation, a general discussion of impact ionization is given.

I. INTRODUCTION

A large number of semiconductor devices operate on the basis of highly energetic (hot) electrons. Impact ionization is an essential mechanism in the operation of photodetectors¹ and impact-avalanche transit-time (IMPATT) diodes.² At present, however, the understanding of this effect is limited to a number of theories³⁻⁸ which contain several adjustable parameters whose physical significance is not well understood. The most widely used theory of impact ionization has been given by Baraff.⁵ The adjustable parameters of his theory are the threshold energy for ionization, the optical-phonon energy, the ionization mean free path, and the mean free path for optical-phonon scattering. Although some attempts have previously been made to determine these parameters theoretically,^{9,10} a "complete" theory of impact ionization, which is capable of calculating these quantities (and therefore the ionization rate) from first principles, has not been developed. The main reason is that any theory applicable at extremely high electric fields (causing ionization) must abandon the effective-mass approximation or simple extensions using the $\bar{k} \cdot \bar{p}$ method, and instead include a realistic band structure. The surprising success of Baraff's theory in explaining the electric field dependence of the ionization rate is due to the adjustable parameters, which can "absorb" the band-structure effects. The inclusion of the band structure in solutions of the Boltzmann equation, however, is impractical. It is also difficult to include realistic scattering mechanisms. For example, the inclusion of both small angle scattering and randomizing scattering mechanisms in the same analytical frame-

work is difficult. As a consequence all the previous theories are only applicable to specific materials. For instance, Dumke's theory⁷ is only applicable to InSb or InAs, whereas Baraff's⁵ or the Chwang *et al.*⁸ treatment is only valid for nonpolar materials, such as Si or Ge.

The Monte Carlo method provides an alternative to the solution of the Boltzmann equation.^{11,12} The method can take into account a large variety of scattering mechanisms, and therefore, is applicable to both polar and nonpolar semiconductors. It can calculate the quantities of interest such as drift velocity, mean free path, and average electron energy without any *a priori* assumption on the form of the distribution function. Some attempts have previously been made to calculate the impact ionization rate by the Monte Carlo method,^{13,14} but without including a realistic band structure. In this paper we describe a Monte Carlo method that includes a realistic band structure as calculated by the empirical pseudopotential method.¹⁵ This method should provide a tool for understanding electronic transport in very high fields. Of course, we do not yet have all the necessary information to perform a rigorous calculation at such high fields. For example, not much is known about the selection rules for scattering at points of low symmetry, the changes of the ionization matrix, and the scattering rate at high energies. Because of this lack of information, we must still use a simpler model than the method would allow for. These simplifications should not be considered as restrictions of the method itself. As more information becomes available in the future, the method can be improved with ease to accommodate new information. In spite of the simplifications, the results we obtain provide in-

sight into how the various parameters in previous theories are connected and into how the band structure influences the impact ionization rate. In particular, the method is applied to study the electron-initiated ionization in GaAs. The results also give us information about the accuracy of the pseudopotential band structure at high energies.

II. SUMMARY OF EXPERIMENTAL RESULTS

Before we discuss the theory of impact ionization, it is instructive to summarize the available experimental data. Various experimental techniques to measure the ionization rate are described in detail in the review paper by Stillman and Wolfe.¹ Their article also contains some of the experimental data on the electron-initiated ionization rate in GaAs. Figure 1 summarizes more recent data.¹⁶⁻¹⁹ The experimental results usually show a $1/F^2$ dependence of the ionization rate (F is the electric field). As can be seen from the figure, the data of different workers scatter almost by an order of magnitude.

Of special interest are the results of Pearsall *et al.*,¹⁹ who measured the electron ionization rate with the electric field applied in three different crystallographic directions. Their data are replotted in Fig. 2. They have measured the highest ionization rate in the $\langle 110 \rangle$ direction and the lowest in the $\langle 111 \rangle$ direction. They have attributed this difference to ballistic electrons and electron tunneling to the

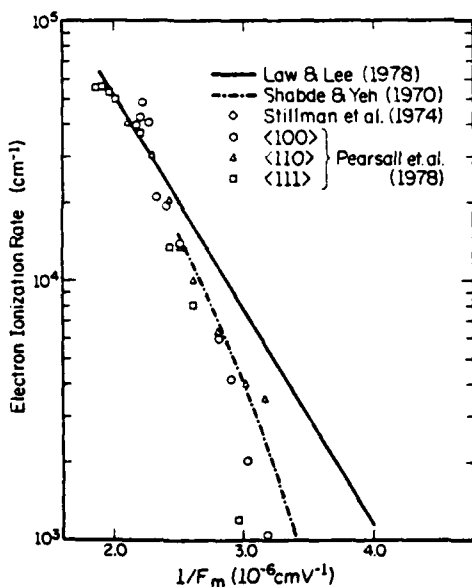


FIG. 1. Experimental ionization rates of electrons for GaAs at room temperature (Refs. 16-19).

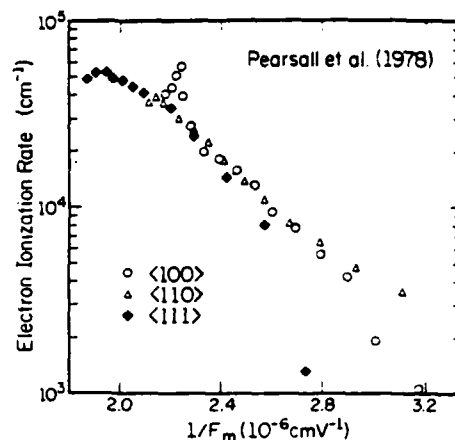


FIG. 2. Experimental electron ionization rates by Pearsall *et al.* (Ref. 19) as a function of reciprocal electric field for three orientations of electric field.

next higher conduction band.^{19,20} Although these data raise an interesting question as to how the band structure actually influences the ionization rate, their notion of ballistic electrons seems to be incorrect, as is shown in this work. More systematic and reliable data are necessary to make a comparison with the theory.

III. PREVIOUS THEORIES OF IMPACT IONIZATION

Wolff³ was the first to calculate the ionization rate in semiconductors. He applied the gas discharge theory to solve the Boltzmann equation taking into account the effect of electron-phonon and pair-producing collisions on the distribution function. The velocity distribution function was approximated as

$$n(v, \theta) = n_0(v) + n_1(v) \cos \theta \quad (1)$$

where v is the electron velocity, and θ is the angle between the velocity and the electric field. This is an energy diffusion theory, in which the electrons undergo many collisions when moving to higher energies. The Boltzmann equation was then solved to calculate the ionization rate with the result

$$\alpha(F) \sim \exp(-A/F^2) \quad (2)$$

where F is the electric field.

Shockley,⁴ on the other hand, argued that ionization is mainly due to "lucky" electrons which completely escape phonon scatterings and reach the threshold energy. In this streaming approximation the distribution is a spike in the direction of the electric field. He considered the relative probability of

phonon scattering and pair production, and obtained an ionization rate whose dependence on F is given by

$$\alpha(F) \sim \exp(-B/F) \quad (3)$$

Next, Baraff^{5,21} solve the time-independent Boltzmann equation and showed that his result contained Shockley's result as a low-field limit, and Wolf's result as a high-field limit. His theory gives the "universal" curves with phonon mean free path and ionization threshold energy as parameters, which are adjusted to fit theory to experimental data. However, it does not provide a way to calculate these quantities, nor does it include the band structure.

Recently, Chwang *et al.*⁸ took a different approach using a finite Markov chain formation. Their method is based on the calculation of a transition matrix which characterizes the transition probability between virtual states defined by small discrete energy intervals. Interesting as it is, their method is limited by the analytical formulations. It still requires the same assumptions as Baraff's theory and does not produce much more information. For example, an assumption of a constant mean free path for phonon scattering is still necessary. Moreover, the Markov formulation is only applicable to nonpolar semiconductors.

Nevertheless, Baraff's and Chwang's theories contain some "truth" about the impact ionization mechanism, as does Shockley's and Wolf's approach. How they are related, and how they complement each other will be clear as a result of the Monte Carlo calculation described in this work. This Monte Carlo method includes a realistic band structure. As a result, the orientation dependence of the impact ionization can also be calculated.

IV. BAND STRUCTURE OF GaAs

The band structure of GaAs has been calculated using the empirical pseudopotential method as described by Cohen and Bergstresser.¹⁵ Only the lowest conduction band has been considered. The effect of higher bands is briefly discussed in the later sections. Advantage is taken of the 48-fold symmetry of the Brillouin zone of the zinc-blende structure.²² It is only necessary to examine a $\frac{1}{48}$ th of the zone. This region is defined by the conditions

$$0 \leq k_x \leq k_y \leq k_z \leq 1 \quad (4)$$

and

$$k_x + k_y + k_z \leq \frac{3}{2} \quad (5)$$

where all the k components are in units of $2\pi/a$ (a is the lattice constant, $a = 5.64 \text{ \AA}$ for GaAs). Mesh points ($k_x, k_y, k_z = 0.0, 0.1, \dots$) are sampled from this region, and the energy and its gradient (velocity) at each k point are calculated. A total of 249 points have been sampled with 156 points within the region. The extra 93 points outside the region are necessary

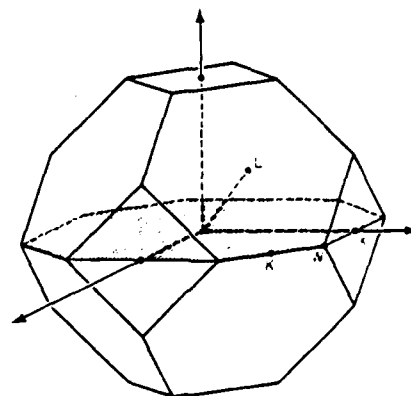


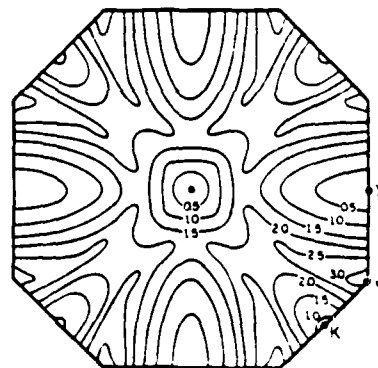
FIG. 3. Cross section of the Brillouin zone.

for the interpolation of energy in the proximity of the surface of the sampling region. Figure 4 illustrates the isoenergy lines in the cross section of the Brillouin zone shown in Fig. 3, with the numbers representing the electron energy from the bottom of the conduction band (at Γ). It can be seen that the Γ valley is nearly isotropic, whereas the X valleys are more elliptic. The band structure is then stored in memory, and used in the Monte Carlo simulation which is described in Sec. VI.

For the study of "lucky electron" transport extra \bar{k} points have been sampled in three major crystal directions, i.e., the $\langle 100 \rangle$, $\langle 110 \rangle$, and $\langle 111 \rangle$ directions. The results have made it obvious (see, for example, Fig. 5 of Ref. 15) that the use of the effective mass and nonparabolicity is not valid for electron energies above approximately 1 eV in some directions. In fact, the effective mass defined as

$$\frac{1}{m^*} = \frac{1}{\hbar^2} \frac{\partial^2 E(k)}{\partial k^2} \quad (6)$$

goes to negative values at higher energies.



V. BALLISTIC ELECTRON TRANSPORT AND PHONON SCATTERING

The term "ballistic electrons" has recently been used to denote those electrons which do not suffer phonon scattering.^{20,23} This is equivalent to the "lucky" electron notion in Shockley's theory. Since the possible contribution of ballistic electrons to impact ionization has been suggested,²⁰ the behavior of ballistic electrons has been examined using the pseudopotential band structure. The study has been performed by solving the equations of motion

$$\hbar \frac{d\vec{k}}{dt} = e\vec{F} \quad (7)$$

and

$$\vec{v} = \frac{1}{\hbar} \nabla_{\vec{k}} E(\vec{k}), \quad (8)$$

where \vec{F} is the applied electric field, \vec{k} is the electron wave vector, E is the electron energy, and \vec{v} is the group velocity of the electron. Equations (7) and (8) are solved simultaneously with the initial condition $\vec{k} = \vec{0}$ at $t = 0$, to express \vec{v} and E as a function of time t . The field is assumed to be constant. Results of the calculations are shown in Fig. 5 for the three major crystallographic directions. The electric field has been chosen to be 500 kV/cm, a typical field for impact ionization. Figure 5 shows the electron velocity, \vec{v} , as a function of time. The orientation dependence of the ballistic behavior is obvious from this figure. The highest peak velocity is reached in the $\langle 100 \rangle$ direction ($\sim 1.1 \times 10^8$ cm/sec) and the lowest

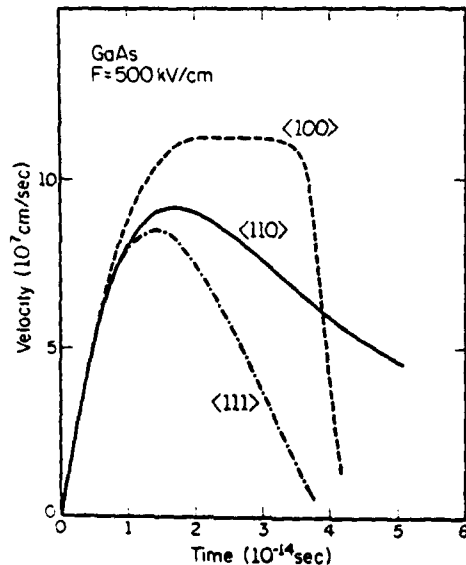


FIG. 5. Variation of ballistic electron velocity with time in three crystallographic directions of GaAs.

in the $\langle 111 \rangle$ direction ($\sim 0.8 \times 10^8$ cm/sec).

In a nonideal crystal, however, ballistic transport must compete with scattering processes. It will be shown by the Monte Carlo simulation that on the average an electron can travel ballistically for only $\sim 3 \times 10^{-14}$ sec before it suffers a phonon scattering. In the $\langle 111 \rangle$ direction, the electron can never gain sufficient energy ballistically for impact ionization.¹⁹ In the $\langle 100 \rangle$ direction, the impact ionization threshold can be reached only if electrons tunnel in \vec{k} space to the next higher band ~ 0.2 eV above the principal conduction band.^{18,19} Therefore scattering events be-

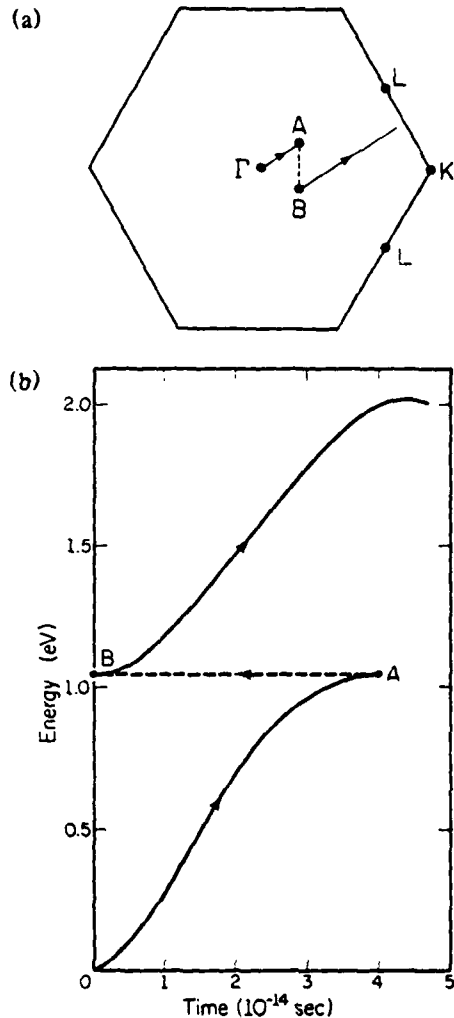


FIG. 6. (a) Example of wave-vector trajectory of electron in ΓKL plane under the influence of electric field in the $\langle 111 \rangle$ direction. Electron is scattered from A to B. Energy change in the scattering process has been neglected. (b) Variation with time of electron energy for the process shown in (a).

come crucial for the occurrence of impact ionization in these directions.

Electrons can be scattered to other regions of the Brillouin zone with a single scattering event being sufficient to permit the electrons to reach threshold energy. This mechanism is illustrated in Fig. 6 for an electric field applied in the $\langle 111 \rangle$ direction. An electron starts at the Γ point and moves along the $\langle 111 \rangle$ direction. At point A [$\vec{k} = (\pi/a)(0.3, 0.3, 0.3)$], the energy is at the maximum for this direction, but it is still much less than the threshold energy. Subsequently, the electron can be scattered (by a phonon or impurity) to some other point in the Brillouin zone, point B , for example. Following this scattering event, the $\langle 111 \rangle$ component of the electron wave vector continues to increase. However, the wave vector points in a direction different from the $\langle 111 \rangle$ so that the electron can now reach a higher energy. As shown in Fig. 6, the electron can actually exceed the threshold energy for impact ionization (~ 2.0 eV).

This is, of course, only one example of an electron trajectory to show the importance of scattering processes to impact ionization. The actual calculation of the impact ionization rate must involve averaging of all the possible electron trajectories until the electron reaches the threshold energy. This is achieved by the Monte Carlo method which is described in the next section.

VI. SIMULATION METHOD

The Monte Carlo simulation keeps track of an electron \vec{k} vector in the Brillouin zone until it reaches the threshold energy for impact ionization. This is done with a knowledge of scattering mechanisms, scattering rates, and band structure in the whole Brillouin zone. The $E(\vec{k})$ relation for an arbitrary \vec{k} point can be calculated in the following way. First, the \vec{k} point is mapped into the sampling region by using the point-group symmetry. The energy is then calculated by quadratic interpolation utilizing the energies and the gradients of the surrounding eight mesh points. The gradient is interpolated only linearly. Applying the inverse operations on the calculated energy and gradient gives the $E(\vec{k})$ relation and the gradient at the original \vec{k} point.

Next we need to know the phonon scattering rate. Ideally the scattering rate should be calculated at each \vec{k} point in order to take into account the overlap integral.²⁴ Also, when the initial or final electron state is not on the symmetry points, the selection rules²⁵ become less restrictive and this may give rise to additional scattering. Moreover, even near the bottom of the valleys, it is known that the scattering rates are different in the Γ , L , and X valleys. We have assumed the scattering rate to be isotropic (only energy dependent) for simplicity and because of lack of additional information. We have taken the scattering rate

as given for the central valley. This overestimates the scattering rate when the electron is in the satellite valleys. The simplification is partly justified by the fact that the scattering rates of different valleys approach each other at higher energies. Furthermore, since scattering to upper bands is possible in reality (which increases the scattering rate in the satellite valleys), the overestimation is at least partly compensated.

The values of the parameters for the calculation of the scattering rate are the same as the ones used in the simulation of the Gunn effect.²⁶ They are known to give a good fit to the experimental data at low fields. Below 0.33 eV only polar optical scattering occurs in the central valley. Above 0.33 eV polar optical scattering occurs only when an electron is in the central valley arbitrarily defined as

$$-0.3 \leq k_x, k_y, k_z \leq 0.3 \quad (9)$$

where the components are in units of $2\pi/a$. Otherwise intervalley scattering occurs. It is not appropriate to simply extend the scattering rate to higher energies because of the complicated band structure. Because the intervalley scattering rate is proportional to the density of final states, and the density of states in the conduction band decreases nearly quadratically above 1.5 eV,²⁷ we have assumed a quadratically decreasing scattering rate above 1.5 eV. The resultant total scattering rate as a function of electron energy is shown in Fig. 7 (solid line). The maximum scattering rate is 4.5×10^{14} sec⁻¹ at 1.5 eV.

In the $\langle 100 \rangle$ direction the threshold state for electron-initiated ionization lies in the second conduction band.¹⁸ An electron can tunnel through the "pseudogap" (~ 0.2 eV) between the lowest and the second conduction band to reach threshold. No attempt has been made to simulate this tunneling mechanism. Since the tunneling time is estimated to be of the order of 1×10^{-13} sec,¹⁸ and the intervalley scattering time for an electron energy of 2.0 eV is much shorter ($< 1 \times 10^{-14}$ sec) than this tunneling time, electrons are more likely to be scattered before they can tunnel to the upper band. Therefore, the contribution of these tunneling electrons to impact ionization is expected to be small.

The final state of the scattering process is determined in the following way. Since polar optical scattering is dominant only at low energies in the central valley, the usual formula with effective mass and nonparabolicity terms is used to choose a candidate for the final \vec{k} point. The energy at this \vec{k} point is then recalculated using the exact band structure to check if it is within an allowed range (typically 30 meV) around the final energy (for example, $E + \hbar\omega_{\text{ph}}$ in the case of phonon absorption). If it is outside this range, a different final state is chosen and the process is repeated until a proper state within the correct energy range is found. Intervalley scattering

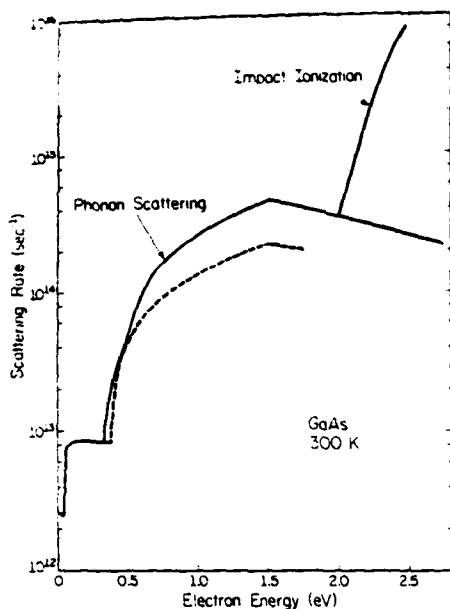


FIG. 7. Phonon scattering rate and the impact ionization probability in GaAs as a function of electron energy. The parameters are due to Littlejohn *et al.* (solid line) (Ref. 26) and Vinson *et al.* (broken line) (Ref. 33).

is known to be completely randomizing.²⁸ For this mechanism, once the final energy is calculated, those mesh points whose energies are within the allowed range are tabulated. One of them is then randomly selected as the final state. The correct overall energy loss is checked and ensured in our procedure.

Our treatment of phonon scattering processes represents a compromise between accuracy and numerical tractability. For a finite number of mesh points, the energy separation between any two \vec{k} points is finite. For example, for our 156 mesh points this energy separation can be as large as 60 meV. The allowed energy range during the scattering must be large enough to bridge this gap in order to assure the continuity of the energy band. In the limit of infinitely fine mesh points, the allowed range for final energy can be infinitely small. The number of \vec{k} points in this energy range for a given final energy is proportional to the density of states at each region of \vec{k} space with this final energy. Therefore, in the limit of infinitely fine mesh our procedure is correct, since the scattering rate for deformation potential scattering is proportional to the final density of states.

The impact ionizing collision is treated as an additional scattering mechanism. We assume an isotropic threshold energy of 2.0 eV. Anderson and Crowell⁹ have shown that the threshold energy actually depends on the \vec{k} vector. However, their graphical

procedure is almost impossible to perform in three-dimensional momentum space. A more systematic approach may be possible.²⁹ If the threshold energy is calculated for each \vec{k} point, it can be easily included in this simulation procedure. The impact ionization probability can be calculated from the matrix element for the screened Coulomb interaction.^{14,30,31} However, here we use a simpler model demonstrated by Keldysh^{6,32} and used by others.⁸ According to Keldysh the probability of impact ionization can be represented as

$$\frac{1}{\tau_i(E)} = \frac{1}{\tau(E_i)} P \left(\frac{E - E_i}{E_i} \right)^2, \quad (10)$$

where E is the electron energy, E_i is the threshold energy, $1/\tau(E_i)$ is the scattering rate at $E = E_i$, and P is a dimensionless constant which is usually much larger than unity. This formula is valid for semiconductors with large dielectric constants. We take P as a parameter. $P = \sim 50 - \infty$ has been used by Chwang *et al.*⁸ As shown by Baraff,⁵ and then by Chwang⁸ the impact ionization rate does not strongly depend on this parameter as long as P is large compared to unity. The energy dependence of the impact ionization probability for $P = 400$ is illustrated in Fig. 7.

Once the scattering rate and the ionization probability are determined, the rest of the simulation procedure is similar to the conventional Monte Carlo method.¹¹ The scattering probability $[\Delta t/\tau(E)]$ is calculated at each time interval, Δt , and compared with a random number. This is necessary because of the complicated $E(\vec{k})$ relation. Δt is taken to be approximately $\frac{1}{10}$ th the average drift time. The simulation starts by releasing an electron with zero energy at the bottom of the central valley. The energy and the \vec{k} vector of the electron are traced. When impact ionization occurs, the energy is reinitialized to zero to start a new history. This is justified by the fact that the resultant electron after ionization lies very close to the bottom of the central valley.⁹ The impact ionization rate can be obtained by averaging each distance that an electron travels until impact ionization occurs over a sufficient number of ionizations. The distance, Δx , traveled during each drift is calculated either by accumulating a differential distance, $v\Delta t$, or by utilizing the relation

$$\Delta E = eF\Delta x, \quad (11)$$

where ΔE is the energy gained during the drift. The velocity v is calculated from the gradient of the $E(\vec{k})$ relation.

VII. RESULTS

A: Contribution of ballistic electrons

By terminating the simulation after the first scattering the electron suffers, the behavior of ballistic elec-

trons can be studied. Additionally, we can determine the extent which these ballistic electrons contribute to impact ionization. Since there is no electron-initiated threshold state in the $\langle 100 \rangle$ or the $\langle 111 \rangle$ direction,¹⁹ we only consider the $\langle 110 \rangle$ direction. We have also changed the threshold energy to 1.7 eV, which is the correct threshold energy in this direction.⁹ Typically 100 000 trials have been done for each electric field.

The result of the calculation shows that an electron travels on the average approximately 200 Å, for an average time of 3×10^{-14} sec before the first scattering event. These numbers differ slightly for different orientations. By counting those electrons which cause impact ionization instead of scattering, we can estimate the contribution of ballistic electrons to the impact ionization rate. If the same scattering rate is used as shown in Fig. 7 (known to give a good fit to the Gunn effect²⁶), we find no electrons (less than 0.001%) causing impact ionization. There may be some uncertainties in the scattering rate, particularly in the values of the deformation potential constants. To find the maximum possible contribution of ballistic electrons to impact ionization, a smaller scattering rate has been tried. We have used the values given by Vinson *et al.*³³: $E_{\Gamma-X} = 0.4$, $E_{\Gamma-L} = 0.38$ eV, $D_{\Gamma-X} = 1.1 \times 10^9$, and $D_{\Gamma-L} = 2.8 \times 10^8$ eV/cm. This gives the scattering rate shown by the broken line in Fig. 7. This rate is approximately half of the previous value. Using this scattering rate in our calculation we obtain the results shown in Fig. 8. This fig-

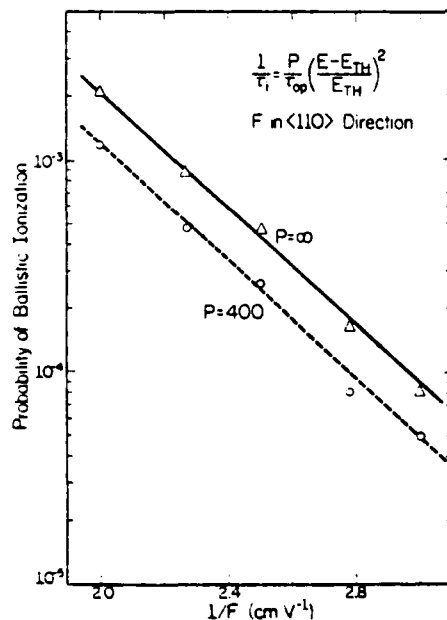


FIG. 8. Probability of ballistic electron causing impact ionization as a function of a reciprocal electric field.

ure shows the probability that an electron causes impact ionization prior to its scattering by a phonon as a function of electric field. As can be seen, even at the maximum (500 kV/cm for $P = \infty$), only 0.2% of the electrons causing impact ionization are "ballistic." Therefore we conclude that the contribution of ballistic electrons to impact ionization is negligibly small if our present understanding of the scattering rate is correct. This conclusion negates the considerations by Capasso *et al.*²⁰ who suggested that ballistic electrons give a non-negligible contribution to the total ionization rate.

These "ballistic" electrons were discussed by Shockley who called them "lucky" electrons.⁴ We have shown that Shockley's theory gives ionization rates that are too small. It is interesting to note, however, that the two curves in Fig. 8 show the correct $1/F$ dependence as in Shockley's theory in spite of the much more complicated band structure and scattering rate that we used.

B. Transport properties and ionization rate

In the calculation of the impact ionization rate a typical simulation consists of approximately 200 000 to 400 000 scattering events. Depending on electric field this would give 40–300 impact ionization events. Figure 9 shows a typical trajectory of the \bar{k} vector in the Brillouin zone for an electric field of 500 kV/cm in the $\langle 100 \rangle$ direction. The solid lines represent the drift of the electron, and the broken lines represent the scatterings from one end to the next. When the \bar{k} comes to lie outside of the Brillouin zone, it is placed back inside the zone to the equivalent point. This is done by adding the appropri-

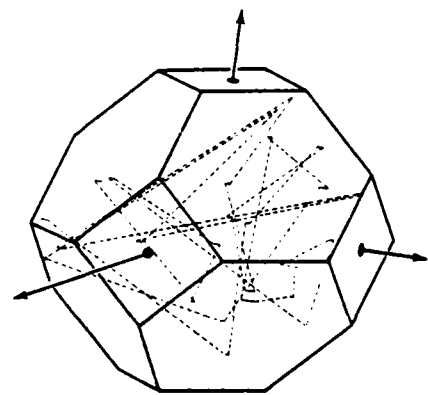


FIG. 9. Typical trajectory of the electron \bar{k} vector in the Brillouin zone for an electric field of 500 kV/cm. The solid lines represent the drift and the broken lines represent the scatterings from one point to the next.

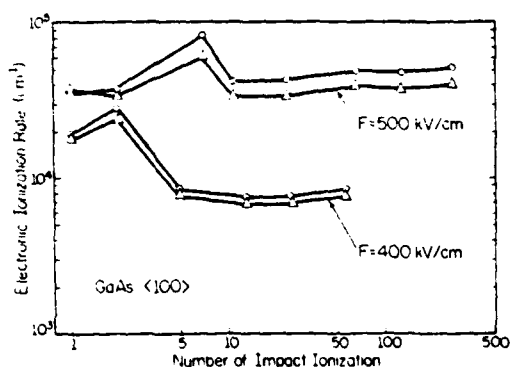


FIG. 10. Impact ionization rate in GaAs as a function of the number of ionizations obtained with the Monte Carlo simulation. The calculation is from the slope of the $E(\vec{k})$ curve (Δ) or from Eq. (11) (\circ).

ate reciprocal-lattice vector to the original \vec{k} vector. As seen from the figure the drift time is very short because of the high scattering rate at higher energies. The electron is frequently scattered over practically the entire Brillouin zone.

Figure 10 shows how the calculated ionization rate converges as the number of ionizations is increased. Because of the limited computer time it has not been possible to take averages over more than 300 ionizations. However, the convergence is fairly good after 10 ionizations. From this figure the statistical fluctuation is estimated to be approximately 20%. The problem of statistical fluctuation can be overcome by repeating the simulation only for the high-energy tail.³⁴ This has not been attempted in this work.

Figure 11 shows the average electron energy as a function of the electric field. The reason for the steeper increase beyond 100 kV/cm is not understood, but may be related to the band structure. Figure 12 shows the electron mean free path as a function of electric field. In the electric field range where impact ionization occurs, the mean free path between phonon scattering ranges from 50 to 30 Å. This is in

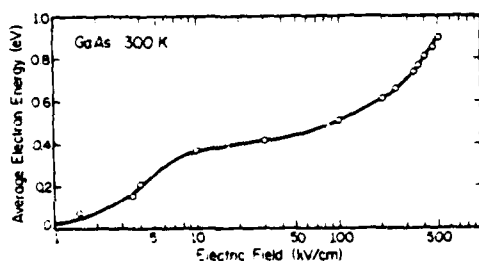


FIG. 11. Average electron energy in GaAs as a function of electric field calculated by the Monte Carlo simulation.

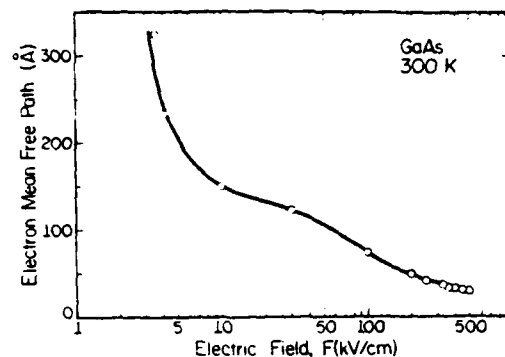


FIG. 12. Electron mean free path in GaAs as a function of electric field calculated by the Monte Carlo simulation (steady state).

agreement with previous data^{2,35} and the conventional Monte Carlo calculation.¹⁰ The reason that our calculation agrees in this respect with the conventional interpretation which does not include a realistic band structure is that the mean free path is mainly determined by the average electron energy, which is still small enough (~ 0.8 eV) for effective mass and nonparabolicity corrections to be sufficient (at least in certain \vec{k} directions).

The calculated electric field dependence of the electron drift velocity is shown in Fig. 13. The broken curve represents the experimental data by Ruch and Kino³⁶ at low electric field (< 14 kV/cm), and by Houston and Evans³⁷ at high field (~ 20 – 100 kV/cm). The agreement is good over the entire range of electric fields experimentally investigated. The result using Eq. (11) gives much better fit than the result using the slopes of the $E(\vec{k})$ relation. It is

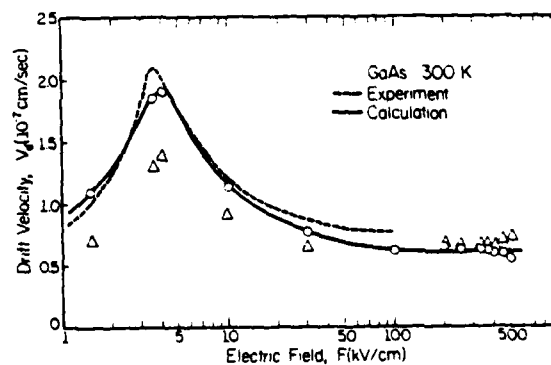


FIG. 13. Calculated electron drift velocity in GaAs at room temperature compared with the experimental data (Refs. 36 and 37). The calculated values are from the slope of the $E(\vec{k})$ curve (Δ) or from Eq. (11) (\circ).

suspected that the accumulation of numerical errors in the slope calculation is responsible for the discrepancy. The slight deviations between theory and experiment at higher fields are believed to be mainly due to the pseudopotential band structure which gives the satellite valley effective masses larger than are usually assumed. From Fig. 13 it can also be seen that the calculations describe quantitatively the Gunn effect. This means that the method can simulate polar optical scattering as well as intervalley scattering, and that the transition from polar optical scattering (low-energy region) to intervalley scattering (high-energy region) is accomplished smoothly.

Figure 14 shows the calculated electric field dependence of the impact ionization rate in GaAs for three different crystal orientations. We have assumed $P = 400$. The shaded region indicates the range covered by the experimental data (Sec. II). The agreement is fair, considering the uncertainty in the scattering rate at higher energies. The inclusion of upper bands is expected to increase the calculated ionization rate slightly, and therefore to improve the fit to the experimental data. Note, however, that the calculation shows within statistical uncertainty ($\sim 20\%$) no orientation dependence for the ionization rate. This contradicts previous interpretations of the experimental data by Pearsall *et al.*¹⁹ (Fig. 2). Another way to calculate the orientation dependence is rotating the electric field direction from one axis to another. The result is shown in Fig. 15 for an electric field of 400 kV/cm when the field is rotated from the $\langle 110 \rangle$ to $\langle 111 \rangle$ direction. Again we do not see

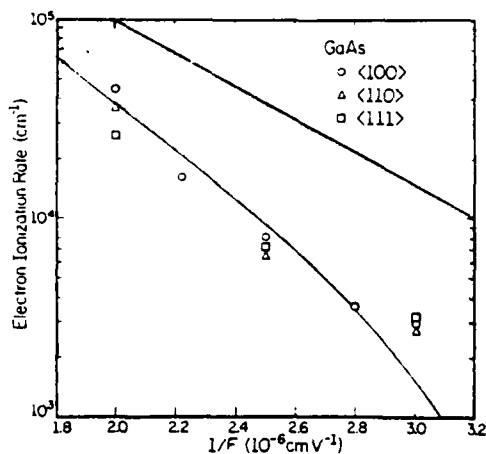


FIG. 14. Calculated impact ionization rate of an electron in GaAs with an electric field in three crystallographic directions as a function of a reciprocal field. The shaded region indicates the range of available experimental data (Fig. 1). Within statistical uncertainty, we do not observe any orientation dependence.

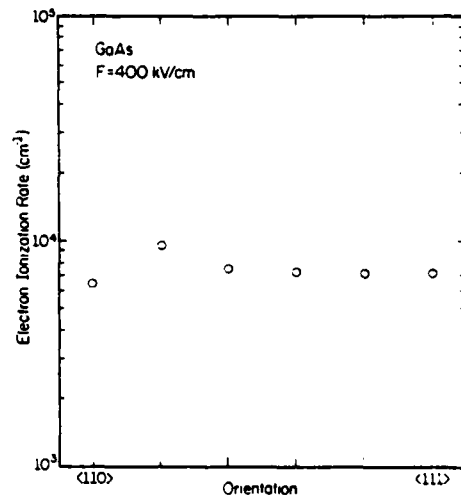


FIG. 15. Calculated impact ionization rate of an electron with an electric field of 400 kV/cm in several directions between the $\langle 110 \rangle$ and $\langle 111 \rangle$ directions.

any orientation dependence within the statistical uncertainty. A solution including this rotation of the electric field can be obtained only by the Monte Carlo method. The effect of changing the value of P has also been examined. Varying P from 50 to 400 we have obtained practically the same impact ionization rate. This confirms the result by Baraff⁵ and Chwang⁸ that the ionization rate is insensitive to the ionization probability as long as it is much larger than the probability of phonon scattering.

For a better understanding of how the electrons acquire the high energies, and how impact ionization is actually accomplished, we show in Figs. 16 and 17 the variation of electron energy after each scattering event for electric fields of 500 and 100 kV/cm, respectively. In the case of 500 kV/cm, the electron energy stays around ~ 0.7 – 1.2 eV most of the time, but the electron occasionally escapes phonon scattering and moves up to higher energies. In Fig. 16 we can see ~ 4 – 5 spikes which reach to ~ 1.8 eV. When an electron reaches 2.0 eV, it causes impact ionization. We can think of these electrons as the "lucky electrons" in Shockley's theory, and those electrons around the average energy as the diffusing (in energy) electrons in Wolff's theory. However, as seen in the figure this classification is not very distinct. Even those electrons in the spikes suffer several scatterings before they reach the peak energies. Our results, therefore, contain Shockley's and Wolff's notions of ionizing electrons as does Baraff's theory (but we have much more general conditions). Using Baraff's word,⁵ the notion of ballistic electrons by Shockley and diffusing electrons by Wolff are "complementary" in

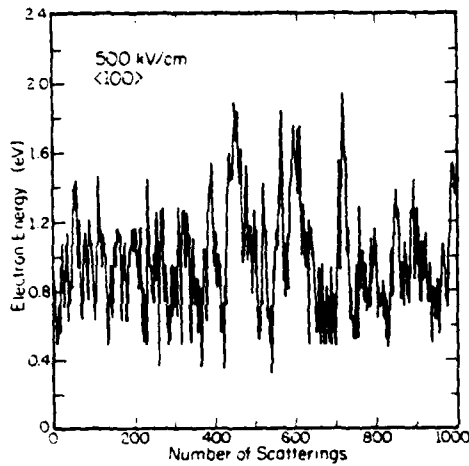


FIG. 16. Variation of electron energy after each scattering event for an electric field of 500 kV/cm obtained with a Monte Carlo simulation.

determining the impact ionization rate. This is due to the fact that the height of spikes (in Fig. 16) depends on the average energy of electrons. It is also important to note the difference between our ionizing electrons and Shockley's "lucky" electrons. Shockley's "lucky" electrons start from zero energy, escape the phonon scattering completely, and impact ionize. The ionizing electrons of our result start at the average energy and reach ionization threshold after a few scattering events. This explains why Shockley's theory badly underestimates the ionization rate, since he neglected electrons which are scattered at intermediate energy.

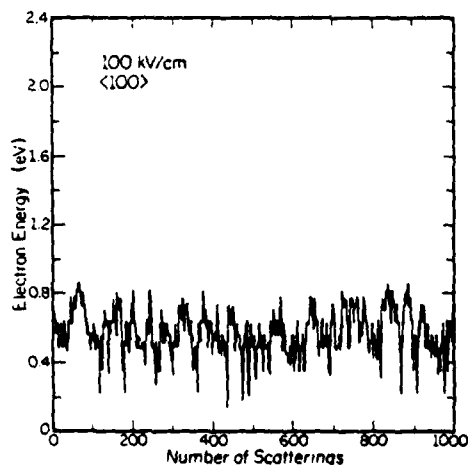


FIG. 17. Variation of electron energy after each scattering event for an electric field of 100 kV/cm.

VIII. CONCLUSIONS

A Monte Carlo simulation of high-field transport in GaAs employing a realistic band structure has been described. The method has been used to study the impact ionization mechanism in GaAs. The band structure of GaAs has been calculated using the empirical pseudopotential method. Partly due to lack of information and partly for simplicity, we have used simplifying assumptions for the phonon scattering rates, the ionization threshold energy, and the ionization probability. This, however, is not an inherent limitation of the method. Unlike previous theories of impact ionization, the method requires, in principle, no adjustable parameters as long as the band structure and the scattering mechanism are known. The method has provided new results and increased the understanding of high-field transport and impact ionization in GaAs. The calculated drift velocity, the mean free path, and the impact ionization rate are in fair agreement with some of the published experimental data. The inclusion of the higher conduction bands is expected to further improve the fit. We do not expect, however, to obtain the anisotropy measured by Pearsall *et al.*¹⁹ In our opinion this anisotropy is not a consequence of the band structure, but is rather caused by crystal defects or other effects not yet understood. It is found that the contribution of ballistic electrons to the impact ionization rate is negligibly small. Shockley's theory, therefore, badly underestimates the ionization rate. We have confirmed that the impact ionization rate is rather insensitive to the ionization probability above the threshold energy as long as the probability is much larger than the phonon scattering rate.

Based on the results of the simulation, a general discussion of impact ionization has been given. We find that typically electrons stay around an average energy and experience a large number of phonon scatterings. Occasionally electrons escape phonon scattering and move up to higher energy. Some reach ionization threshold after a few scattering events. This feature is seen in Fig. 16. It can be considered as a combination of Wolff's and Shockley's notion of ionizing electrons, but the distinction is rather vague. The reason for the success of Baraff's theory is that his theory also contains this feature. However, because of his formulation using distribution functions, the physical picture is not as clear as in our result (Fig. 16). Moreover, our method includes realistic scattering mechanisms and band structure.

Unlike previous theories of impact ionization, the present method can in principle be applied to any semiconductor. The method can be used for both polar and nonpolar materials. This is obvious from the successful simulation of the Gunn effect, which

contains the transition from polar optical scattering to intervalley scattering. The calculation of hole-initiated ionization rates should also be possible, although presently our understanding of hole transport is not as deep as electron transport. This is important for the understanding of the operation of photodetectors, since their performance depends on the ratio of electron- and hole-initiated ionization rates. It should be understood that the method is quite versatile in its application. A transient Monte Carlo method including the band structure may be used to investigate the orientation dependence of the avalanche response time.³⁸ Finally the inclusion of

the position dependence should enable us to study the effect of the "dark space."³⁹

ACKNOWLEDGMENTS

The authors wish to thank E. M. Kesler, R. T. Gladin, and R. F. MacFarlane for technical assistance. They are grateful to Professor G. E. Stillman, Professor B. G. Streetman, and Professor N. Holonyak, Jr., for many valuable discussions. The use of the computer facilities of the Materials Research Laboratory, University of Illinois, is also gratefully acknowledged. The work was supported by the Office of Naval Research and the Joint Services Electronics Program.

- ¹G. E. Stillman and C. M. Wolfe, in *Semiconductors and Semimetals*, edited by R. K. Willardson and A. C. Beers (Academic, New York, 1977), Vol. 12.
- ²S. M. Sze, *Physics of Semiconductor Devices* (Wiley, New York, 1969).
- ³P. A. Wolff, *Phys. Rev.* **95**, 1415 (1954).
- ⁴W. Shockley, *Solid State Electron.* **2**, 35 (1961).
- ⁵G. A. Baraff, *Phys. Rev.* **128**, 2507 (1962).
- ⁶L. V. Keldysh, *Sov. Phys. JETP* **21**, 1135 (1965).
- ⁷W. P. Dumke, *Phys. Rev.* **167**, 783 (1968).
- ⁸R. Chwang, C. W. Kao, and C. R. Crowell, *Solid State Electron.* **22**, 599 (1979).
- ⁹C. L. Anderson and C. R. Crowell, *Phys. Rev. B* **5**, 2267 (1972).
- ¹⁰J. R. Hauser, *Appl. Phys. Lett.* **33**, 351 (1978).
- ¹¹W. Fawcett, A. D. Boardman, and S. Swain, *J. Phys. Chem. Solids* **31**, 1963 (1970).
- ¹²P. J. Price, in *Semiconductors and Semimetals*, edited by R. K. Willardson and A. C. Beer (Academic, New York, 1979), Vol. 14.
- ¹³P. A. Lebowitz and P. J. Price, *Solid State Commun.* **9**, 1221 (1971).
- ¹⁴R. C. Curby and D. K. Ferry, *Phys. Status Solidi A* **15**, 319 (1973).
- ¹⁵M. L. Cohen and T. K. Bergstresser, *Phys. Rev.* **141**, 789 (1966).
- ¹⁶S. N. Shabde and C. Yeh, *J. Appl. Phys.* **41**, 4743 (1970).
- ¹⁷G. E. Stillman, C. M. Wolfe, J. A. Rossi, and A. G. Foyt, *Appl. Phys. Lett.* **24**, 471 (1974).
- ¹⁸H. D. Law and C. A. Lee, *Solid State Electron.* **21**, 331 (1978).
- ¹⁹T. P. Pearsall, F. Capasso, R. E. Nahory, M. A. Pollack, and J. R. Chelikowsky, *Solid State Electron.* **21**, 297 (1978).
- ²⁰F. Capasso, R. E. Nahory, and M. A. Pollack, *Solid State Electron.* **22**, 977 (1979).
- ²¹G. A. Baraff, *Phys. Rev.* **133**, A26 (1964).
- ²²D. Brust, *Phys. Rev.* **134**, A1337 (1964).
- ²³M. S. Shur and L. F. Eastman, *IEEE Trans. Electron Devices* **ED-26**, 1677 (1979).
- ²⁴D. Matz, *Phys. Rev.* **168**, 843 (1968).
- ²⁵J. L. Birman, M. Lax, and R. Loudon, *Phys. Rev.* **145**, 620 (1966).
- ²⁶M. A. Littlejohn, J. R. Hauser, and T. H. Glisson, *J. Appl. Phys.* **48**, 4587 (1977).
- ²⁷J. R. Chelikowsky and M. L. Cohen, *Phys. Rev. B* **14**, 556 (1976).
- ²⁸E. M. Conwell, *Solid State Physics* (Academic, New York, 1967), Suppl. 9.
- ²⁹P. T. Landsberg and D. J. Robbins, *J. Phys. C* **10**, 2717 (1977).
- ³⁰E. Antončík, *Czech. J. Phys. B* **17**, 735 (1967).
- ³¹D. J. Robbins, *Phys. Status Solidi B* **97**, 9 (1980).
- ³²L. V. Keldysh, *Sov. Phys. JETP* **10**, 509 (1960).
- ³³P. J. Vinson, C. Pickering, A. R. Adams, W. Fawcett, and G. D. Pitt, in *Proceedings of 23th International Conference on Physics of Semiconductors, Rome, 1976* (unpublished).
- ³⁴P. J. Price (private communication).
- ³⁵H. Kressel and G. Kupsky, *Int. J. Electron.* **20**, 535 (1966).
- ³⁶J. G. Ruch and G. S. Kino, *Phys. Rev.* **174**, 921 (1968).
- ³⁷P. A. Houston and A. G. R. Evans, *Solid State Electron.* **20**, 197 (1977).
- ³⁸J. Barenz, J. Kinoshita, T. L. Hielt, and C. A. Lee, *Electron. Lett.* **15**, 150 (1979).
- ³⁹Y. Okuto and C. R. Crowell, *Phys. Rev. B* **10**, 4284 (1974).

drive current for a constant magnetic field and the results are plotted in Fig. 4. The 50 Hz oscillating magnetic field was supplied by a solenoid 0.295 m long and the mean field strength was 3.93 mT r.m.s. The detector output reached a maximum value of 4.77×10^{-3} r.m.s. as the polarisation ratio increased. This corresponds to a Faraday rotation of about 0.14° r.m.s. Using the magnetic field parameters, this yields a value for the magneto-optic Verdet constant of 2.58×10^{-6} rad A^{-1} at 830 nm wavelength. This figure is in excellent agreement with the value obtained by extrapolating visible wavelength data using the reciprocal square wavelength dependence of the Verdet constant.

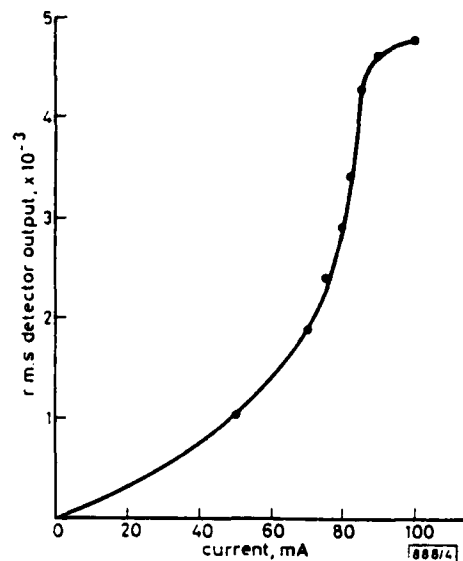


Fig. 4 Graph of r.m.s. detector output against current

Conclusion: The polarisation properties of single-mode double-heterostructure stripe lasers make them suitable light sources for optical-fibre current measurement systems and they should be useful in any optical fibre system where a linearly polarised light source is required.

Acknowledgment: This work was carried out at the Central Electricity Research Laboratories and is published by permission of the Central Electricity Generating Board.

A. M. SMITH
Central Electricity Research Laboratories
Kelvin Avenue
Leatherhead, Surrey KT22 7SE, England

6th February 1980

References

- HAYASHI, I., PANISH, M. B., and REINHART, F. K.: 'Gallium arsenide double-heterostructure injection lasers', *J. Appl. Phys.*, 1971, 42, pp. 1929-1941
- SAKUMA, I., YONEZU, H., NISHIDA, K., KABAYASHI, K., SAITO, F., and NANNICHI, Y.: 'Continuous operation of junction lasers at room temperature', *Japan J. Appl. Phys.*, 1971, 10, pp. 282-283
- REINHART, F. K., HAYASHI, I., and PANISH, M. B.: 'Mode reflectivity and waveguide properties of double heterostructure injection lasers', *J. Appl. Phys.*, 1971, 42, pp. 4466-4479
- IKEGAMI, T.: 'Reflectivity of mode at facet and oscillation mode in double-heterostructure injection lasers', *IEEE J. Quantum Electron.*, 1972, QE-8, pp. 470-476
- NISHIZAWA, J., FAKUDA, H., and MORISHITA, M.: 'The control of polarisation of laser diodes', *ibid.*, 1977, QE-13, pp. 604-609
- RAMASWAMY, V., and FRENCH, W. G.: 'Influence of noncircular core on the polarisation performance of single-mode fibres', *Electron. Lett.*, 1978, 14, pp. 143-144
- VALL, V., and SHORTHILL, R. W.: 'Fibre ring interferometer', *Appl. Opt.*, 1976, pp. 1099-1100
- SMITH, A. M.: 'Polarization and magneto-optic properties of single-mode optical fibre', *ibid.*, 1978, 17, pp. 52-56
- NORMAN, S. R., PAYNE, D. N., ADAMS, M. J., and SMITH, A. M.: 'Fabrication of single-mode fibres exhibiting extremely low polarisation birefringence', *Electron. Lett.*, 1979, 15, pp. 309-311

0013-5194/80/060706-03\$1.50/0

ORIENTATION DEPENDENCE OF BALLISTIC ELECTRON TRANSPORT AND IMPACT IONISATION

7

Indexing terms: Charge carriers, Semiconductors

The orientation dependence of ballistic electron transport in GaAs is investigated using the pseudopotential band structure. It is shown that a single scattering event can permit electron impact-ionisation threshold energies to be reached in the $\langle 111 \rangle$ and $\langle 100 \rangle$ directions. This is in contrast to ballistic calculations, where simple thresholds do not exist in these directions.

Ballistic transport of carriers is important for the understanding of impact ionisation in semiconductors. Shockley's theory of impact ionisation¹ considers those electrons which have escaped the scattering events and ballistically reach the threshold energy. Recently, Capasso *et al.*² have shown that ballistic motion competes with inter-valley scattering in determining electron dynamics in GaAs. Ballistic transport can also be utilised in low-power high-speed logic devices.³ It is the purpose of this letter to present the results of detailed calculations which confirm that the ballistic motion of electrons in GaAs depends sensitively upon the crystallographic direction of the electric field. However, the calculations also show that one phonon-scattering event is sufficient for an electron to reach the threshold energy for impact ionisation with an electric field applied in the $\langle 111 \rangle$ direction, even though there is no threshold state for ballistic electron-initiated impact ionisation⁵ in this crystalline direction.

The ballistic electron behaviour is studied by solving the equations of motion:

$$\hbar \frac{dk}{dt} = eF \quad (1)$$

and

$$v = \nabla_k E(k) \quad (2)$$

where F is the applied electric field, k is the electron wave vector, E is the electron energy and v is the group velocity of the electron. The band structure $E(k)$ is calculated by employing the empirical pseudopotential method of Cohen and Bergstresser.⁴ Eqns. 1 and 2 have been solved in successive small time intervals with the initial condition $k = 0$ at $t = 0$. The field F is assumed to be constant, i.e. we are interested only in cases where a few ballistic electrons cause the impact ionisation.

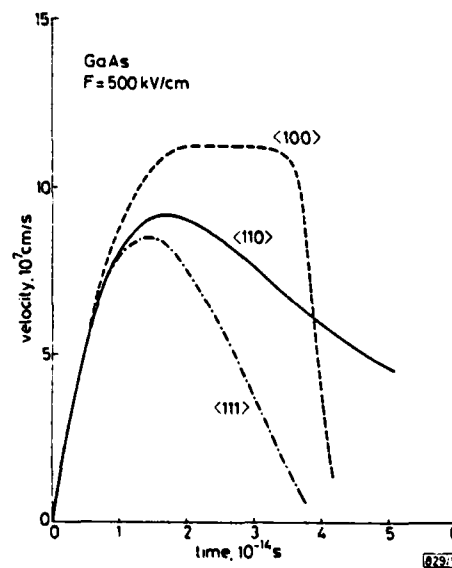


Fig. 1 Variation of ballistic electron velocity with time

chosen to be 500 kV/cm. Fig. 1 shows the electron velocity v as a function of time. The orientation dependence of ballistic behaviour is obvious from this Figure. The highest peak velocity

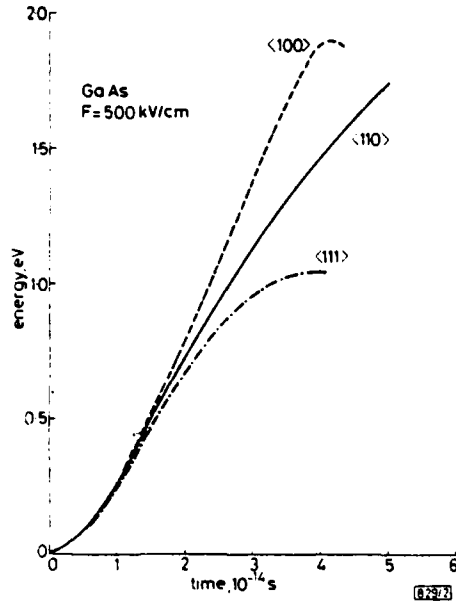


Fig. 2 Variation of electron energy with time as measured from the conduction band edge

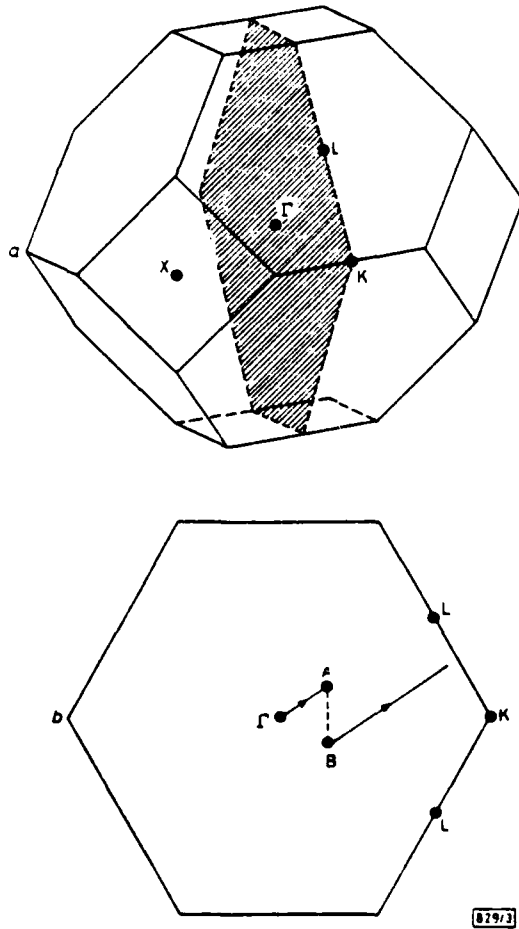


Fig. 3
 a (110) section of the first Brillouin zone
 b Wave vector trajectory of electron in this plane under the influence of electric field in $\langle 111 \rangle$ direction. Electron is scattered from A to B. Energy change in the scattering process has been neglected

time as measured from the conduction-band edge. The rate of increase is largest in the $\langle 100 \rangle$ direction and smallest in the $\langle 111 \rangle$ direction. Of course, ballistic transport must compete with the scattering processes. The dominant scattering mechanism for electron energies greater than 0.35 eV is intervalley scattering. The momentum relaxation time for this scattering process is about 2×10^{-14} s. Figs. 1 and 2 show that, even within this short timespan, the effect of orientation can be considerable. Ballistic electron transport can occur on longer time scales, but only with decreasing probability.

The orientation trend in Figs. 1 and 2 agrees with experimental results⁵ which show that, in GaAs, the electron impact ionisation rates are higher in the $\langle 100 \rangle$ and the $\langle 110 \rangle$ direction than in the $\langle 111 \rangle$ direction. The distance which an electron can travel in 2×10^{-14} s also reflects the same orientation dependence: 0.039 μm , 0.034 μm and 0.031 μm in the $\langle 100 \rangle$, $\langle 110 \rangle$ and $\langle 111 \rangle$ directions, respectively, for an electric field of 500 kV/cm.

In the $\langle 111 \rangle$ direction, the electron can never gain sufficient energy ballistically for impact ionisation. In the $\langle 100 \rangle$ direction, the impact-ionisation threshold can be reached only if electrons tunnel in k -space to the next higher band ~ 0.2 eV above the principal conduction band.⁵ As a result, scattering events become crucial for the occurrence of impact ionisation in these directions. Electrons can be scattered to other regions of the Brillouin zone, and a single scattering event is sufficient to permit the electrons to reach threshold energy. This mechanism is illustrated in Figs. 3 and 4. An electron starts at the point and moves along the $\langle 111 \rangle$ direction. At point A, ($k \sim 0.3\sqrt{3}\pi/a$), the energy is at the maximum for this direction, but it is still much less than the threshold energy. Subsequently, the electron can be scattered (e.g. by a phonon or impurity) to some other point in the first Brillouin zone; point B, for example. Following this scattering event, the $\langle 111 \rangle$ component of the electron wave vector continues to increase. However, the wave vector points in a direction different from $\langle 111 \rangle$ such that the electron can now reach a higher energy. As shown in Fig. 4, the electron can actually exceed the threshold for impact ionisation. This clearly indicates the importance of scattering processes to impact ionisation. We also note that since $\nabla_k E$ is not always in the direction of the electric field for

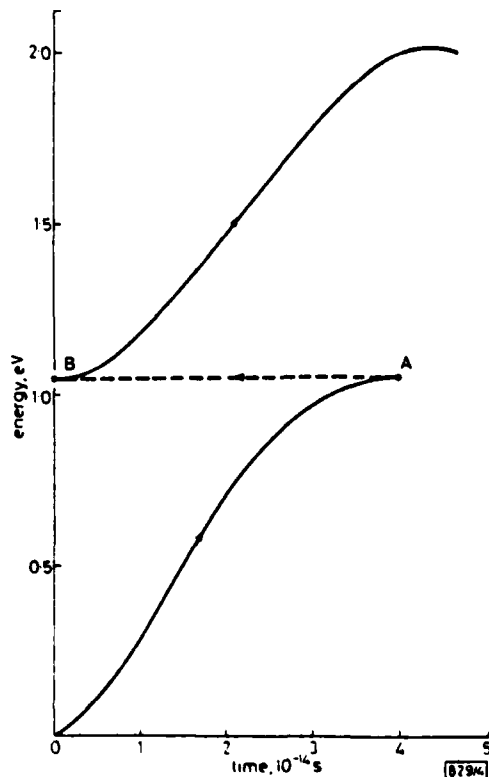


Fig. 4 Variation with time of electron energy for the process shown in Fig. 3

the path starting at point B, the electron trajectory in real space deviates slightly from the $\langle 111 \rangle$ direction.

In the $\langle 100 \rangle$ direction, the threshold state is separated from the principal conduction band by a small gap (~ 0.2 eV).⁵ Pearsall *et al.* argue that tunnelling through this 'pseudogap' is responsible for the impact ionisation in this direction. Law and Lee⁶ have shown that this tunnelling time is of the order of 4×10^{-13} s. This time is much longer than the inter-valley scattering time ($\sim 2 \times 10^{-14}$ s). Therefore electrons have a higher probability of being scattered before they tunnel through the gap. Using these characteristic time constants, it is possible to show that it is unlikely that tunnelling contributes more than 10% of the electrons for the impact ionisation in this direction. Of course, all the above arguments apply only near the threshold of impact ionisation, where ballistic electrons determine the rate. Far above the threshold, where the isotropic part of the distribution function contributes to impact ionisation, one can expect only slight orientation dependence.

In conclusion, we have discussed the importance of crystal-line orientation to ballistic electron transport and to the electron impact-ionisation rate of GaAs using the empirical pseudopotential band structure. We have also illustrated the significance of scattering events to the impact ionisation. More quantitative calculations using Monte Carlo techniques are in progress.

Acknowledgments: We would like to thank Profs. N. Holonyak, Jun., M. Altarelli and B. G. Streetman for helpful discussions. Research support from the Office of Naval

Research is gratefully acknowledged.

H. SHICHIJO
K. HESS
G. E. STILLMAN

21st January 1980

Department of Electrical Engineering & Coordinated Science Laboratory
University of Illinois at Urbana-Champaign
Urbana, Illinois 61801, USA

References

- 1 SHOCKLEY, W.: 'Problems related to p - n junctions in silicon', *Solid-State Electron.*, 1961, **2**, pp. 35-67
- 2 CAPASSO, F., NAHORY, E., and POLLAK, M. A.: 'Hot electron dynamics in GaAs avalanche devices: competition between ballistic behavior and intervalley scattering', *ibid.*, 1979, **22**, pp. 977-979
- 3 SHUR, M. S., and EASTMAN, L. F.: 'Ballistic transport in semiconductor at low temperatures for low-power high-speed logic', *IEEE Trans.*, 1979, **ED-26**, pp. 1677-1683
- 4 COHEN, M. L., and BERGSTRESSER, T. K.: 'Band structures and pseudopotential form factors for fourteen semiconductors of the diamond and zinc-blend structures', *Phys. Rev.*, 1966, **141**, pp. 789-796
- 5 PEARSALL, T. P., CAPASSO, F., NAHORY, R. E., POLLAK, M. A., and CHELIKOWSKY, J. R.: 'The band structure dependence of impact ionization by hot carriers in semiconductors: GaAs', *Solid-State Electron.*, 1978, **21**, pp. 297-302
- 6 LAW, H. D., and LEE, C. A.: 'Interband scattering effects on secondary ionization coefficients in GaAs', *ibid.*, 1978, **21**, pp. 331-340

0013-5194/80/060208-03\$1.50/0

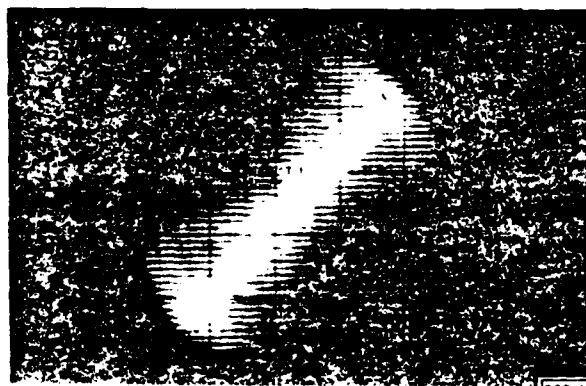
NEAR-FIELD DISTRIBUTIONS IN SELECTIVELY EXCITED ELLIPTICAL OPTICAL FIBRES

Indexing terms: Optical fibres, Wave propagation

Short (1-400 m) multimode fibres were excited by a single-mode fibre. The resulting near-field intensity distributions are generally not circularly symmetric. A calculation based on ray optics shows that slightly elliptical fibres give similar distributions. This calculation assumes a central index-profile dip.

Introduction: Recently the nature of ray propagation in elliptical fibres has been investigated by several authors.^{1,2} In particular, Ankiewicz has plotted diagrams depicting the paths of representative rays in elliptical fibres. In this letter, we will extend these results to profiles containing a central index dip and show that they can be verified experimentally.

Apparatus: Light from a d.h. laser operated below threshold is collimated through a half-metre length of a single-mode fibre with a core radius of $5 \mu\text{m}$ and an n.a. of 0.04. The emerging beam is then coupled to a multimode fibre, typically of core diameter $50 \mu\text{m}$ and n.a. = 0.2. The resulting near-field distribution is focused onto a 100×100 c.c.d. photodiode matrix and displayed on an oscilloscope.



Results: Figs. 1 and 2 are near-field patterns produced by a typical nearly parabolic c.v.d. fibre with a 1-2 μm central index dip and an ellipticity (defined as the ratio of the major to the minor axis) of the order of 1.01. Fig. 1 shows the near-field distribution of a 1 m fibre sample excited near the edge of its core and along one of its principal axes. Fig. 2 is produced by a 40 m length of the same fibre excited near the edge of the core and at an angle of 45° with the major axis. If we excite other

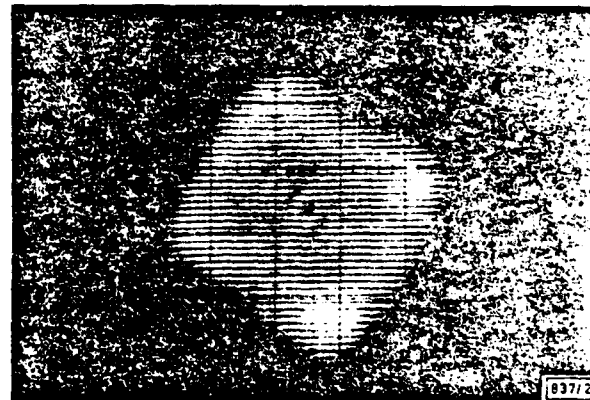


Fig. 2 As in Fig. 1, excitation equidistant from axis



IMPACT IONISATION IN MULTILAYERED HETEROJUNCTION STRUCTURES

Indexing terms: Ionisation, Photoelectric devices, Semiconductors, Charge carriers

Calculations are reported showing that in multilayered heterojunction structures the effective impact ionisation rates for electrons and holes can be very different, even if they are the same in the basic bulk materials. The reason for this is the difference in the band-edge discontinuities for electrons and holes and the lower phonon mean free path for holes in quantum well structures.

As is well known, the signal/noise ratio of an avalanche photodiode (a.p.d.) is influenced by the statistics of the gain process, and, because of feedback effects, significantly more noise is generated when both electrons and holes produce secondary pairs.¹ For lowest excess noise in a.p.d.s it is desirable to have a material in which the ionisation rates for electrons α and for holes β are significantly different, and in addition to have a device structure which results in injection of the carrier with the highest ionisation rate into the multiplication region.² For detection at various wavelengths it is useful to use III-V compounds and ternary and quaternary alloys of these compounds in which the bandgap is only slightly smaller than the energy of the photons to be detected. Unfortunately, preliminary measurements of α and β seem to indicate that in most of these materials the electron and hole impact ionisation rates are nearly equal. It is the purpose of this letter to show that two effects specific to multiheterostructure quantum layers may be useful in the construction of low noise a.p.d.s from materials in which α and β are approximately equal.

The basic physical ideas are as follows:

(i) The impact ionisation rate depends exponentially on the impact ionisation threshold and on the energy from which the electron (hole) starts to be accelerated. Therefore a step-like band structure as shown in Fig. 1, where the discontinuity in the conduction band is greater than that in the valence band, will enhance the ionisation rate for electrons. This can easily be seen by subtracting (adding) the conduction band-edge step to the ionisation threshold in the Baraff theory.³ A rigorous justification for this procedure can only be given for special cases, because in general the effect of the band-edge step on the ionisation rate will depend on the energy which the electron

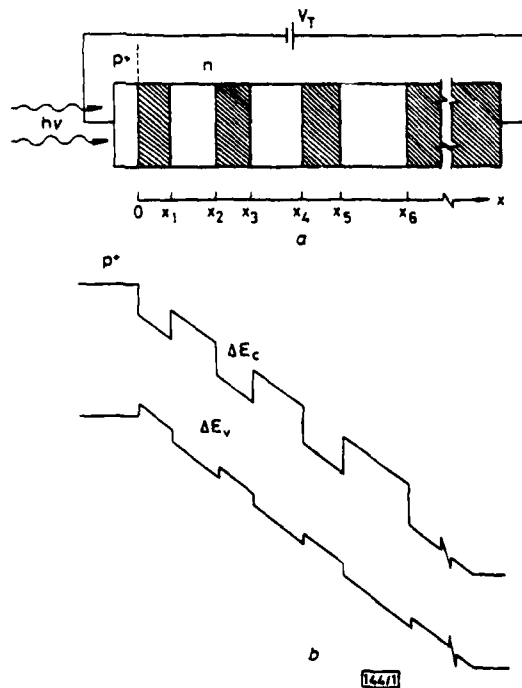


Fig. 1 Basic structure of a.p.d. with quantum well layers
a Shaded regions, GaAs; unshaded regions, Al Ga. As

already has when it approaches the junction.

(ii) As shown by Holonyak and co-workers,^{4,5} the scattering rate in quantum wells is different to that in the bulk and, at low energies at least, holes are scattered more often and thus are collected more effectively in the quantum wells. An analysis of this effect is difficult because it must include the reflection and transmission through the (nonideal) heterojunction. However, inserting different mean free paths in the Baraff theory shows immediately that this effect can strongly change the α/β ratio if it prevails up to the energy of the impact ionisation threshold.

The following estimates are based on a structure appropriate for GaAs-Al_xGa_{1-x}As layers with the material constants adjusted to give α/β when inserted in the Baraff theory for bulk material. A polynomial fit to the Baraff theory is used in the calculations.³ The values of the material constants are listed in Table 1.

The p⁺-n junction is assumed to be steplike with uniform doping densities on each side. The electric field accelerating the electrons and causing impact ionisation has three sources: the external voltage, the built-in voltage and the band-edge step of the heterojunction. The first two are taken into account in the usual way by inserting space dependent electric fields in the Baraff theory. As mentioned above, the band-edge discontinuity has to be treated in a different way because the band-edge energy changes over a distance which is much shorter than the mean free path between collisions. To assess the effect of the band-edge step on the ionisation rate, consider an electron that travels from one Al_xGa_{1-x}As layer into a GaAs layer.

Table 1 MATERIAL CONSTANTS

	E_i	λ	d	ΔE
Electron	2.0 eV	50 Å	150 Å	0.6 eV
Hole	1.5 eV	40 Å	150 Å	0.106 eV

E_i = Threshold ionisation energy (Averaged in different k directions;² λ = optical phonon mean free path; d = impact ionisation mean free path; ΔE = band-edge discontinuity (ΔE_c for conduction band, ΔE_v for valence band))

When it arrives in the GaAs it 'sees' not only the smaller bandgap of the GaAs, but it also starts at an energy ΔE_c (conduction band edge step) above the GaAs band edge. To include this effect, we deduct the 'excess' energy ΔE_c from the GaAs impact ionisation threshold within a distance from the discontinuity equal to the impact ionisation mean free path. This process increases α much more than β since, when the same procedure is followed for holes, the valence band edge step ΔE_v is much smaller.^{4,5}

The thickness of the layers should be chosen so that after an electron impact ionises in the GaAs layer it can gain sufficient energy in this layer to get out of the well, and after the electron

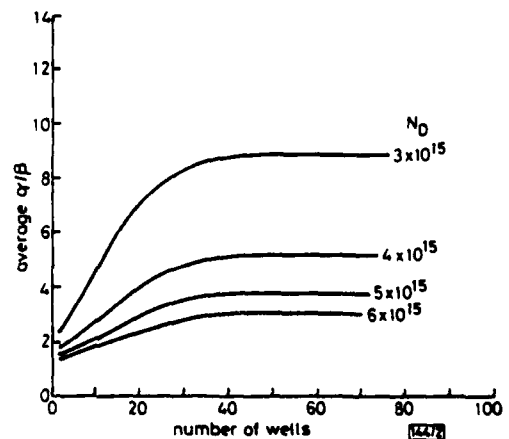


Fig. 2 α/β against number of quantum wells for external voltage of 100V

enters the $\text{Al}_x\text{Ga}_{1-x}\text{As}$ layer with small kinetic energy, it gains the effective threshold energy $E_i(\text{GaAs}) - \Delta E_c$ before arriving at the next GaAs layer. $E_i(\text{GaAs})$ is the impact ionisation threshold for bulk GaAs. Note that the values of the layer width x , vary for different design parameters, i.e., doping concentration N_D , the applied voltage and the position within the structure. However, the calculated value of the thickness is always close to 300 Å for GaAs layers, and 500 Å for the $\text{Al}_x\text{Ga}_{1-x}\text{As}$ layer.

The above procedure gives immediately the α/β ratio at a particular location in the layers. The value of α/β relevant to the multiplication factor in an a.p.d. is given by the spatial average over the whole structure. Our results for the average effective α/β ratio are shown in Fig. 2. As can be seen the enhancement of the α/β ratio is substantial especially for low values of the donor density N_D . The multiplication factor is in an interesting range (i.e., of the order of 10 or larger) only for the two highest doping concentrations shown in Fig. 2. The reasons for this are outlined below.

The second effect which enhances α/β , the higher phonon scattering rate of holes in the heterojunction structures, has not been included in the results of Fig. 2. It is clear that this effect once more increases α/β . In fact the mean free path for phonon scattering enters more sensitively in the impact ionisation rate

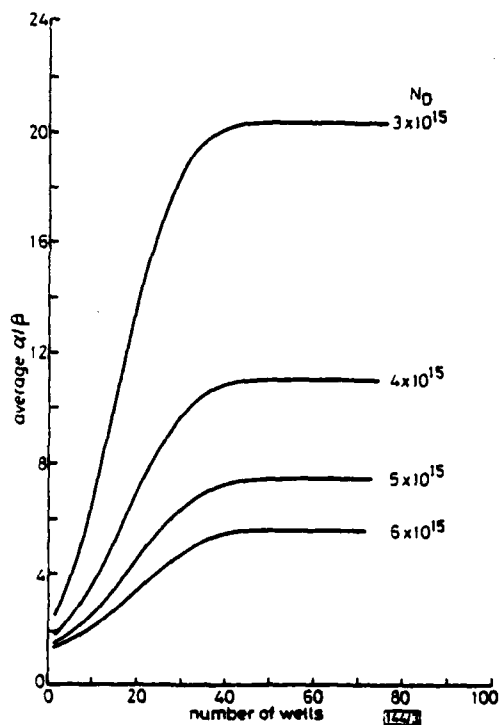


Fig. 3 As Fig. 2 but with reduced optical phonon mean free path for holes (30 Å instead of 40 Å)

than the ionisation threshold. The amount of the reduction of mean free path is not known exactly, as the results of Holonyak and co-workers apply only for electrons with rather low energy. We therefore have changed the hole mean free path

rather arbitrarily from 40 Å to 30 Å in the GaAs quantum wells to demonstrate the effect. The result for the average α/β ratio is shown in Fig. 3, once more against the number of wells.

From the above discussion it is clear that the α/β ratio depends sensitively on the structure and doping concentration. This is due to the fact that α is considerably larger than β only for electric fields $E < 10^6$ V/cm. Therefore, if we choose to increase the multiplication factor, we automatically reduce the α/β ratio. Nevertheless, the above analysis shows that even for multiplication factors above 10 the α/β ratio can be substantially enhanced in quantum well structures, especially because of the second enhancement effect, the reduction of the phonon mean free path. Finally we would like to note that fluctuating fields associated with compositional disorder in ternaries and quaternaries have an effect similar to the band-edge discontinuity at the heterojunction and can increase (decrease) the α/β ratio. Work is in progress on these effects and will be reported later.

Acknowledgments: The authors wish to thank E. M. Kesler, S. B. Marshall, R. T. Gladin and R. F. MacFarlane for technical assistance. The work has been supported by NSF Grants DMR-79-09991 and DMR-23999 and Navy contract N00019-79-C-0768.

R. CHIN*

N. HOLONYAK, JUN.

G. E. STILLMAN

Department of Electrical Engineering
& Materials Research Laboratory
University of Illinois at Urbana-Champaign
Urbana, Ill. 61801, USA

J. Y. TANG

K. HESS

Department of Electrical Engineering
& Coordinated Science Laboratory
University of Illinois at Urbana-Champaign
Urbana, Ill. 61801, USA

* Now at Rockwell International, Thousand Oaks, California, USA

1st May 1980

References

- 1 MCINTYRE, R. J.: 'Multiplication noise in uniform avalanche diodes', *IEEE Trans.*, 1966, ED-13, pp. 164-167
- 2 STILLMAN, G. E., and WOLFE, C. M.: 'Avalanche Photodiodes', in WILLARDSON, R. K., and BEER, A. C. (Eds.): 'Semiconductors and Semimetals' (Academic, New York, 1977), pp. 291-393
- 3 CROWELL, C. R., and SZE, S. M.: 'Temperature dependence of avalanche multiplication in semiconductors', *Appl. Phys. Lett.*, 1966, 9, pp. 242-244
- 4 SHICHIJO, H., KOLBAS, R. M., HOLONYAK, N. JR., DUPUIS, R. D., and DAPKUS, P. D.: 'Carrier collection in a semiconductor quantum well', *Solid State Commun.*, 1978, 27, pp. 1029-1032
- 5 HOLONYAK, N. JR., KOLBAS, R. M., DUPUIS, R. D., and DAPKUS, P. D.: 'Quantum-well heterostructure lasers', *IEEE J. Quantum Electron.*, 1980, QE-16, pp. 170-186

0013-5194/80/120467-03\$1.50/0

Phonon contribution to double-heterojunction laser operation

9

N. Holonyak, Jr., B. A. Vojak, and W. D. Laidig

Department of Electrical Engineering and Materials Research Laboratory, University of Illinois at Urbana-Champaign, Urbana, Illinois 61801

K. Hess

Department of Electrical Engineering and Coordinated Science Laboratory, University of Illinois at Urbana-Champaign, Urbana, Illinois 61801

J. J. Coleman and P. D. Dapkus

Rockwell International Electronics Research Center, Anaheim, California 92803

(Received 21 February 1980; accepted for publication 12 May 1980)

Laser data (77 and 300 K) are presented on two photopumped undoped metalorganic chemically vapor-deposited $\text{Al}_x\text{Ga}_{1-x}\text{As}$ -GaAs heterostructures with active regions consisting of: (i) a thick GaAs layer ($L_{z1} \sim 1500 \text{ \AA}$) coupled to an auxiliary quantum-well array of seven small $L_{z2} \sim 50 \text{ \AA}$ coupled GaAs layers, and (ii) a comparison single thick GaAs layer ($L_z \sim 600 \text{ \AA}$) in the form of a conventional double heterostructure (DH). Because of the strengthening of phonon-assisted recombination with temperature, laser operation of the bulk ($L_z \geq 500 \text{ \AA}$) GaAs layers is shifted from $\hbar\omega \sim E_g$ at 77 K to $E_g - \hbar\omega_{LO} < \hbar\omega < E_g$ at room temperature. This behavior of the bulk DH GaAs layers agrees with that of the reference recombination radiation observed from the auxiliary quantum-well array (wafer #1), which recent work indicates is phonon assisted.

PACS numbers: 42.55.Px, 78.55.Ds, 81.15.Gh, 85.60.Jb

Recent work has shown that phonon involvement in the laser operation of quantum-well heterostructure (QWH) lasers is readily observed¹⁻⁶ and, in fact, should be expected.^{3,6} It is even possible to induce phonon-sideband laser operation of a single larger quantum well with a phonon generating array (a phonon resonator) of smaller quantum wells.⁷ In contrast, phonon-sideband laser operation of a standard double heterostructure (DH), i.e., a DH of active-region thickness $L_z \geq 500 \text{ \AA}$ and here assumed (as is common) lightly doped or undoped ($< 10^{17}/\text{cm}^3$), has not been identified even though laser operation of an undoped DH GaAs active region is commonly observed 30–35 meV below the band gap E_g .^{8,9} It is not uncommon in such a case to propose some sort of model involving unexplained impurities,⁹ which, if acceptors, would have to exceed a density of $10^{17}/\text{cm}^3$ to have much validity.¹⁰ In this letter we describe experiments indicating that for standard DH lasers, with undoped active regions ($n_d - n_a \leq 10^{15}/\text{cm}^3$), it is also phonon participation that accounts for the laser operation at reduced energy ($\hbar\omega < E_g$). The effect of phonons is observed by coupling a quantum-well phonon generating and reflecting array of seven coupled 50- \AA GaAs wells to a bulk DH GaAs active region ($L_z \sim 1500 \text{ \AA}$),⁶ and by comparing the shift with temperature of the recombination radiation of the bulk GaAs and the phonon-sideband marker radiation of the small-well array. At 300 K the recombination radiation is shifted by $\sim \hbar\omega_{LO}$.

The two $\text{Al}_x\text{Ga}_{1-x}\text{As}$ -GaAs heterostructures constructed for this work are grown by metalorganic chemical vapor deposition (MO-CVD).¹¹⁻¹³ A GaAs buffer layer is grown first on a {100} GaAs substrate and is followed by a $\sim 1\text{-}\mu\text{m}$ -thick $\text{Al}_x\text{Ga}_{1-x}\text{As}$ ($x \sim 0.36$) confining layer, then the active region, and finally another confining layer ($x \sim 0.36$) of thickness $\sim 0.3 \mu\text{m}$. The active region of the first wafer consists of a 1500- \AA (bulk) GaAs layer coupled to

an array of seven small GaAs quantum wells ($L_z \sim 50 \text{ \AA}$) which are in turn coupled by $\sim 50\text{-}\text{\AA}$ $\text{Al}_x\text{Ga}_{1-x}\text{As}$ ($x \sim 0.32$) barrier layers. The second wafer is similar to the first except for the active region, which is a single GaAs layer of thickness $L_z \sim 600 \text{ \AA}$. To eliminate the possibility of band-to-impurity laser transitions, all layers in the wafers are

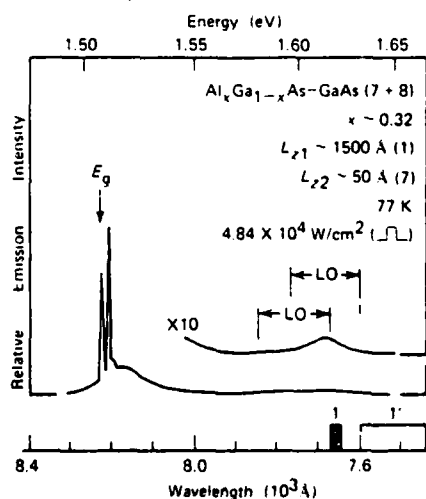


FIG. 1. Pulsed laser operation ($4.8 \times 10^4 \text{ W/cm}^2$, 77 K) of a photopumped undoped ($n_d - n_a \leq 10^{15}/\text{cm}^3$) MO-CVD $\text{Al}_x\text{Ga}_{1-x}\text{As}$ -GaAs multiple-quantum-well heterostructure. The sample is $23 \times 390 \mu\text{m}^2$ in size and has an active region (confined between ~ 1 and $\sim 0.3\text{-}\mu\text{m}$ $x \sim 0.36$ $\text{Al}_x\text{Ga}_{1-x}\text{As}$ layers) consisting of one bulk $L_{z1} \sim 1500\text{-}\text{\AA}$ GaAs layer and seven thin $L_{z2} \sim 50\text{-}\text{\AA}$ GaAs layers, all coupled by 50- \AA -thick $\text{Al}_x\text{Ga}_{1-x}\text{As}$ ($x \sim 0.32$) barriers. At low temperature laser operation is observed on and slightly above the GaAs band edge (band-to-band transitions, $\hbar\omega \sim E_g$). A spontaneous emission reference peak is also observed ($\times 10$ inset) near and on the broadened $n = 1$ electron-to-heavy-hole transitions of the auxiliary quantum-well array (seven coupled 50- \AA GaAs layers).

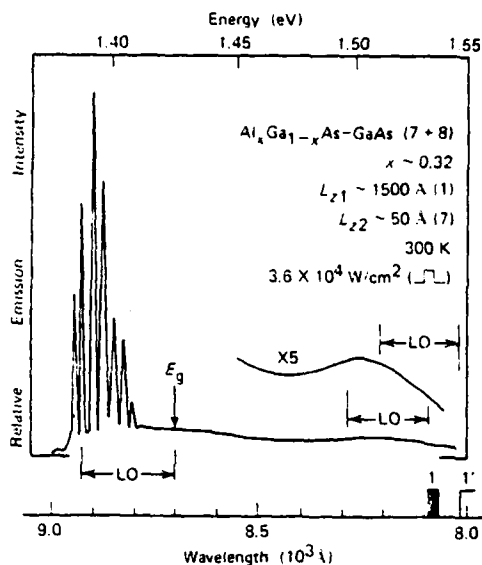


FIG. 2. Room-temperature laser operation ($3.6 \times 10^4 \text{ W/cm}^2$) of the same undoped quantum-well heterostructure as that of Fig. 1. The cleaved rectangular sample ($43 \times 94 \mu\text{m}^2$) is heat sunk in annealed copper under a diamond window and pulse excited to avoid heating effects. The laser modes of the bulk GaAs layer ($L_{z1} \sim 1500 \text{ \AA}$) and the spontaneous reference peak ($\times 5$ inset) of the small ($L_{z2} \sim 50 \text{ \AA}$) quantum-well array are shifted down $\hbar\omega_{LO}$ in energy relative to E_g (GaAs) and relative to the $n = 1$ electron-to-heavy-hole and $n' = 1'$ electron-to-light-hole transitions as shown by the "LO" markers.

grown undoped ($n_d - n_a \leq 10^{15}/\text{cm}^3$). The GaAs substrate is removed by polishing and selective etching; the remaining $\sim 1.4\text{-}\mu\text{m}$ -thick wafer is cleaved into samples of dimensions $\sim 50 \times \sim 150 \mu\text{m}$ (average) which are heat sunk and then photoexcited with an Ar^+ laser ($\lambda \sim 5145 \text{ \AA}$) focused to a circular spot with a diameter comparable to the sample width.⁶

The 77-K emission spectrum of a rectangular sample cleaved from the first wafer is shown in Fig. 1. Two features are apparent: (i) Laser operation occurs on or somewhat above (high excitation, $4.8 \times 10^4 \text{ W/cm}^2$) the band edge E_g of the bulk GaAs layer ($L_z \sim 1500 \text{ \AA}$). (ii) At much shorter wavelength a small emission bump, which serves as a reference, is located very close to the broadened $n = 1$ electron-to-heavy-hole transitions (dark marker) of the seven coupled $50\text{-}\text{\AA}$ GaAs quantum wells. The two "LO" markers show where this bump would be located if, as hot carriers thermalize, much phonon generation occurred in the coupled $50\text{-}\text{\AA}$ quantum wells, as is indeed the case when this section is a bigger fraction of the active region (> 0.5).⁷

The behavior of this material (wafer #1) changes radically at 300 K (Fig. 2). The laser emission shifts to well below the band edge, $E_g - \hbar\omega_{LO} < \hbar\omega < E_g$. This agrees with the shift of the reference emission bump one phonon. $\hbar\omega_{LO}$, below the $n = 1$ electron-to-heavy-hole or the $n' = 1'$ electron-to-light-hole transitions of the auxiliary quantum-well array. The quantum-well transitions are expected to be phonon assisted¹⁻⁷ but, as discussed below, are not very temperature sensitive nor in the present case very heavily excited. Thus, if the emission of the quantum-well array shifts

with temperature, the emission of the bulk GaAs layer is certain to shift, provided phonon-assisted recombination governs its behavior.

The behavior of the second wafer, which is near the boundary in size between bulk and quantum-well dimensions, is shown in Fig. 3. For the $600\text{-}\text{\AA}$ active region, and no auxiliary quantum-well array, the emission is free of the reference emission bump and is peaked (a, spontaneous emission, 10^3 W/cm^2 , 300 K) well above the band edge, or in the region of the $n = 3$ or 4 electron-to-heavy-hole transitions if they could be identified. At high excitation levels, as here, band filling easily reaches into this region. Laser operation at higher excitation (b, $4.7 \times 10^4 \text{ W/cm}^2$) occurs about one phonon below "transition" $n = 3$ (here inserted simply as a reference), which is well below E_g . At 77 K the laser operation (c, $2.5 \times 10^4 \text{ W/cm}^2$, i.e., comparable excitation level) occurs distinctly on the band edge, which indicates that impurities are not important in the recombination process nor carrier-induced band-gap shrinkage.⁶

It is interesting to note that the physical structure of a DH laser is important in respect to the phonon contribution to its operation. First, the major discontinuity in energy gap from the $\text{Al}_x \text{Ga}_{1-x} \text{As}$ confining layers to the GaAs active region requires many LO phonons to be emitted in the process of carrier injection ("hot" carriers) and carrier thermalization. Also, the LO phonons are expected, because of

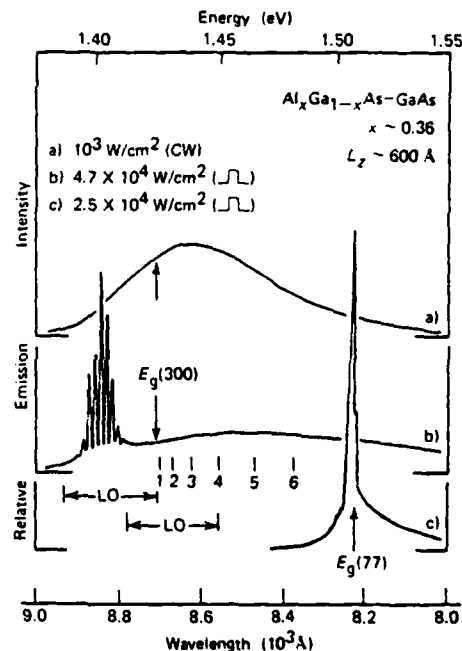


FIG. 3. Emission spectra of a photopumped undoped $\text{Al}_x \text{Ga}_{1-x} \text{As-GaAs}$ DH platelet ($70 \times 94 \mu\text{m}^2$) with a $600\text{-}\text{\AA}$ -thick GaAs active region confined between ~ 1 and $\sim 0.3\text{-}\mu\text{m}$ $x \sim 0.36 \text{ Al}_x \text{Ga}_{1-x} \text{As}$ layers. At room temperature the spontaneous emission at high excitation (a, 10^3 W/cm^2) exhibits a broad peak near the $n = 3$ or 4 electron-to-heavy-hole transitions. Laser operation (b, $4.7 \times 10^4 \text{ W/cm}^2$) occurs approximately one phonon, $\hbar\omega_{LO}$, below the $n = 3$ or 4 peak, which is well below $E_g(300)$. At 77 K (c, $2.5 \times 10^4 \text{ W/cm}^2$) laser operation of another sample ($117 \times 164 \mu\text{m}^2$) occurs distinctly on $E_g(77)$, which rules out as important transitions involving impurities or carrier-induced band-gap shrinkage.

the $\text{Al}_x\text{Ga}_{1-x}\text{As}$ -GaAs interfaces, to be restricted to some extent to the volume of the active region.⁶ That the phonons are generated in such large numbers and are partially confined to such a small volume increases the probability of an electron-LO-phonon interaction and phonon assistance in recombination. Thus large-dimension GaAs ($> 1 \mu\text{m}$), not to mention the case without confining heterobarsriers, when photoexcited a few kT within the energy gap has no basis to operate as a laser on an LO-phonon sideband.¹⁴ In fact, the results of Ref. 14 offer further data in support of the mechanism elucidated here.

As mentioned above, in a "two-dimensional" well ($L_z \lesssim 200 \text{ \AA}$) the phonon emission process is expected to depend only weakly on temperature. There are two reasons for this: (i) The phonon occupation number N_q is expected to be at least $10\times$ higher than the thermal equilibrium value for certain ranges of the wave vector q even at 300 K. (ii) Two-dimensional screening of the phonon emission process is less significant than the screening in three dimensions since the screening constant has a limiting value of $2/a_B$,¹⁵ where a_B is the effective Bohr radius and is independent of temperature.

In a three-dimensional (bulk) region, on the other hand, the perturbation of N_q is estimated to be weaker, and the thermal occupation adds significantly to any "stimulated term," which is proportional to $N_q = N_q^{\text{th}} + N_q^{\text{st}}$ where N_q^{th} is the thermal occupation and N_q^{st} is the additionally generated phonon occupation number. In addition, the phonon emission probability in three dimensions is large only for very small values of $|q|$.¹⁶ Therefore screening of the electron-phonon interaction is already of high importance at rather low carrier concentrations. Also, the classical screening length exhibits a significant temperature dependence. In any case, temperature is expected and is observed to play a major role. It is difficult, however, to calculate explicit expressions for the above effects because the energy distribution of the carriers is not known.

In summary, the data and arguments above indicate that phonon-assisted recombination (300 K) is mainly responsible for lowering the emission energy of a DH laser (lightly doped or undoped active region) to the range

$\hbar\omega < E_g$. This conclusion is consistent with the high excitation level ($\sim 10^{17} \text{ A/cm}^2$) typical of DH laser operation, which provides a basis for large-phonon generation.

The authors are grateful to Yuri S. Moroz, R. T. Gladin, B. L. Marshall, and B. L. Payne (Urbana) for technical assistance, and to G. E. Stillman for helpful discussions. The work of the Illinois group has been supported by NSF Grants DMR 79-09991 and DMR 77-23999 and Navy Contract N00014-79-C-0768; the work of the Rockwell group has been partially supported by the Office of Naval Research, Contract N00014-78-C-0711.

¹N. Holonyak, Jr., R. M. Kolbas, W. D. Laidig, M. Altarelli, R. D. Dupuis, and P. D. Dapkus, *Appl. Phys. Lett.* **34**, 502 (1979).

²E. A. Rezek, R. Chin, N. Holonyak, Jr., S. W. Kirchoefer, and R. M. Kolbas, *Appl. Phys. Lett.* **35**, 45 (1979).

³R. M. Kolbas, N. Holonyak, Jr., B. A. Vojak, K. Hess, M. Altarelli, R. D. Dupuis, and P. D. Dapkus, *Solid State Commun.* **31**, 1033 (1979).

⁴B. A. Vojak, N. Holonyak, Jr., R. Chin, E. A. Rezek, R. D. Dupuis, and P. D. Dapkus, *J. Appl. Phys.* **50**, 5835 (1979).

⁵R. D. Dupuis, P. D. Dapkus, N. Holonyak, Jr., and R. M. Kolbas, *Appl. Phys. Lett.* **35**, 487 (1979).

⁶N. Holonyak, Jr., R. M. Kolbas, W. D. Laidig, B. A. Vojak, K. Hess, R. D. Dupuis, and P. D. Dapkus, *J. Appl. Phys.* **51**, 1328 (1980). See also N. Holonyak, Jr., R. M. Kolbas, R. D. Dupuis, and P. D. Dapkus, *IEEE J. Quantum Electron.* **QE-16**, 170 (1980).

⁷J. J. Coleman, P. D. Dapkus, B. A. Vojak, W. D. Laidig, N. Holonyak, Jr., and K. Hess, *Appl. Phys. Lett.* **37**, 15 (1980).

⁸H. Kressel and H. F. Lockwood, *Appl. Phys. Lett.* **20**, 175 (1972).

⁹W. T. Tsang, C. Weisbuch, R. C. Miller, and R. Dingle, *Appl. Phys. Lett.* **35**, 673 (1979).

¹⁰J. A. Rossi, N. Holonyak, Jr., P. D. Dapkus, J. B. McNeely, and F. V. Williams, *Appl. Phys. Lett.* **15**, 109 (1969).

¹¹H. M. Manasevit, *J. Electrochem. Soc.* **118**, 647 (1971).

¹²R. D. Dupuis and P. D. Dapkus, in *Proceedings of the Seventh International Symposium on Gas and Related Compounds*, St. Louis, 1978, edited by C. M. Wolfe (Institute of Physics, London, 1979), pp. 1-9.

¹³R. D. Dupuis and P. D. Dapkus, *IEEE J. Quantum Electron.* **QE-15**, 128 (1979).

¹⁴S. R. Chinn, J. A. Rossi, and C. M. Wolfe, *Appl. Phys. Lett.* **23**, 699 (1973).

¹⁵F. Stern and W. E. Howard, *Phys. Rev.* **163**, 816 (1967).

¹⁶K. Hess, N. Holonyak, Jr., W. D. Laidig, B. A. Vojak, J. J. Coleman, and P. D. Dapkus, *Solid State Commun.* (to be published).

Ultrasensitive detection of aromatic hydrocarbons by two-photon photoionization

Charles Klimcak and John Wessel

Ivan A. Getting Laboratories, The Aerospace Corporation, Los Angeles, California 90009

(Received 17 March 1980; accepted for publication 5 May 1980)

An optimized multiphoton photoionization detection system has been applied to monitor aromatic-hydrocarbon vapor density as a function of temperature. The density curves established for naphthalene by this procedure permit estimation of a detection limit of 5×10^4 molecules/cm³ in a nitrogen buffer gas. With slight modification this method would be capable of single-molecule detection limits.

PACS numbers: 33.80.Kn, 06.70.Dn, 82.80.Di, 64.70.Hz

Recently several research groups have achieved detection limits in the single-atom regime using photoionization-

and fluorescence-based techniques.¹⁻⁵ Attainment of molecular detection at densities approaching this limit is of consid-

Phonon contribution to metalorganic chemical vapor deposited $\text{Al}_x\text{Ga}_{1-x}\text{As-GaAs}$ quantum-well heterostructure laser operation

B. A. Vojak, N. Holonyak, Jr., and W. D. Laidig
 Department of Electrical Engineering and Materials Research Laboratory, University of Illinois at Urbana-Champaign, Urbana, Illinois 61801

K. Hess
 Department of Electrical Engineering and Coordinated Science Laboratory, University of Illinois at Urbana-Champaign, Urbana, Illinois 61801

J. J. Coleman and P. D. Dapkus
 Rockwell International, Electronics Research Center, Anaheim, California 92803

(Received 16 July 1980; accepted for publication 29 October 1980)

A series of experiments have been conducted to determine the extent of longitudinal optical (LO) phonon contribution to quantum-well-heterostructure (QWH) laser operation. Extensive data are presented on metalorganic chemical vapor deposited (MO-CVD) $\text{Al}_x\text{Ga}_{1-x}\text{As-GaAs}$ QWH's with active regions consisting of larger quantum wells, or in some cases bulk layers ($L_z > 500 \text{ \AA}$), coupled to phonon-generating and -reflecting arrays of coupled smaller quantum wells. Because of the electronic and vibrational coupling of the single larger layer to the array, the spontaneous emission and laser emission from these structures differ from that of QWH's containing either a single well or a multilayer of uniform well thickness. In fact, phonon sideband laser operation of the larger GaAs layer can be induced at $\hbar\omega \sim E_g - \hbar\omega_{\text{LO}}$ (undoped layers, $n_d - n_a \lesssim 10^{15} / \text{cm}^3$). An increase in either the thermal or nonthermal phonon occupation number is shown to cause phonon sideband laser operation in a QWH. A guide to the design of the multilayer array also is presented.

PACS numbers: 78.50.Ge, 78.45.+h, 63.20.-e, 81.15.Gh

I. INTRODUCTION

Until quite recently, the design of III-V semiconductor lasers has involved the optimization of carrier, current, and electromagnetic field confinement in some form of stripe-configuration double-heterostructure laser. As the carriers are better confined, however, so also to some extent are the longitudinal optical (LO) phonons that are emitted during the process of carrier energy relaxation from the wider-energy-gap confining layers (injecting layers) to the narrower-gap active region. The role that phonons might play in double-heterojunction (DH) and quantum-well-heterostructure (QWH) lasers has been poorly understood in spite of the fact that large phonon densities are likely to exist in the active region at threshold, which is typically high ($J \sim 10^3 \text{ A/cm}^2$). For example, in an $\text{Al}_x\text{Ga}_{1-x}\text{As-GaAs}$ ($x \sim 0.4$, $T = 300 \text{ K}$) DH laser approximately $[E_g(\text{AlGaAs}) - E_g(\text{GaAs})] / \hbar\omega_{\text{LO}} = (1.923 - 1.424) / 0.036 \approx 14$ LO phonons are emitted for each electron-hole pair injected into the active region. That LO phonons do modify laser action has been shown in the phonon-sideband operation of AlGaAs-GaAs ,^{1,2} InGaPAs-InP ^{3,4} and InGaPAs-GaAsP ,⁵ quantum-well heterostructures. All of these are III-V semiconductor compounds in which, unlike II-VI compounds, phonon participation in laser operation has not previously been identified. This has been more or less expected because the electron-LO phonon coupling is inherently relatively weak in comparison with II-VI compounds.

The relevant recombination and LO phonon scattering processes for undoped GaAs in the bulk and quantum-well

cases are illustrated in the density of states versus energy diagram of Fig. 1. As electronic carriers are confined to a thin-lower-energy-gap semiconductor layer between two wider-gap layers, the single-particle energy spectrum takes on a particle-in-a-box character in the dimension in which

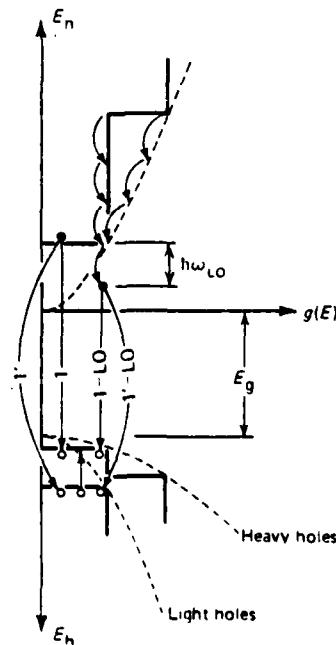


FIG. 1. Density of states diagrams for electrons, heavy holes, and light holes. The step-like cumulative density of states $g(E)$ characteristic of quantum-well heterostructures is contrasted with the density of states of bulk material (dashed curves). The smaller curved arrows indicate electron energy loss (in units of $\hbar\omega_{\text{LO}}$) via electron-LO-phonon scattering. The arrows labeled 1 and 1' represent the recombination of an electron in the $n = 1$ confined-particle state with a heavy hole ($n = 1$) and a light hole ($n' = 1'$), respectively. Light-to-heavy-hole relaxation is indicated by the small upward arrow.

the layer is constricted (e.g., for GaAs $L_z < 500 \text{ \AA}$), and results in a number of quasi-two-dimensional subbands each of which has a constant density of states.⁶ The cumulative densities of states for electrons and for light and heavy holes in the quantum-well regime is steplike as shown in Fig. 1, with each step occurring at the energy of the one-dimensional confined-carrier energy. In the bulk limit, the usual parabolic density of states exists (dashed). The curved arrows on the conduction-band densities of states represent LO-phonon emission by thermalizing electrons while the l , l' , l -LO, l' -LO arrows illustrate the various low-energy confined-carrier radiative recombination transitions in QWH lasers (l is $n = 1$ electron to heavy-hole, l' is $n' = 1'$ electron to light-hole, and l -LO and l' -LO are phonon sidebands of the l and l' transitions). Also shown is the light- to heavy-hole relaxation.

The form of the density of states is fundamental to the process of LO-phonon emission and absorption in polar optical scattering and is so important that, in the two-dimensional limit, the basic electron-LO-phonon interaction is actually slightly enhanced over the bulk case,⁷ making stimulated phonon emission more of a possibility.² Because of this, the nonthermal LO-phonon occupation number is expected to be greatly increased in QWH lasers.⁸ These phonons, however, are extremely difficult to detect. Earlier work⁹ indicates that multiple thin-layer ($L_z \leq 80 \text{ \AA}$) structures, in contrast to single ($L_z \leq 500 \text{ \AA}$) quantum wells, are very efficient in carrier collection and thermalization, and operate readily on LO-phonon sidebands. A valid verification of the role of LO phonons in a QWH is, therefore, the artificial inducing of phonon-sideband laser operation in a larger quantum well ($L_z \sim 200\text{-}500 \text{ \AA}$) or bulk layer by a phonon-generating and -reflecting array of small ($L_z \sim 50\text{-}80 \text{ \AA}$) quantum wells. Also, the identification of phonon-sideband laser operation of a thicker layer ($L_z \geq 200 \text{ \AA}$) is easier because of the advantage that the lowest-energy confined-carrier transitions converge to E_g as L_z increases; the uncertainty in determining L_z and the confined-carrier transitions is thus decreased.

The purpose of the present work is to determine the extent to which LO phonons affect the laser operation (77–300 K) of both QWH and DH $\text{Al}_x\text{Ga}_{1-x}\text{As}$ -GaAs semiconductor lasers. Phonons generated in a thin multiple QWH array are used to induce phonon-sideband emission in a larger, coupled, "phonon-detector" GaAs layer. The extensive data presented on QWH's of various well thicknesses show that $\text{Al}_x\text{Ga}_{1-x}\text{As}$ -GaAs heterostructure lasers can be designed which take advantage of the LO phonons that are inherently generated in these structures.

II. CRYSTAL PREPARATION AND EXCITATION

The $\text{Al}_x\text{Ga}_{1-x}\text{As}$ -GaAs samples of interest here are grown by metalorganic chemical vapor deposition (MOCVD), which has been described extensively elsewhere.^{9,10} The wafers, grown at 750°C on $\{100\}$ GaAs substrates at a calibrated growth rate of $\sim 0.25 \mu\text{m}/\text{min}$ (or slower), consist of a $\sim 1\text{-}\mu\text{m}$ -thick GaAs buffer layer to provide a good crystallographic surface for the succeeding layers, followed by a $\sim 1\text{-}\mu\text{m}$ $\text{Al}_x\text{Ga}_{1-x}\text{As}$ ($x \sim 0.36$) confining layer, then the

QWH active region, and finally a second $\sim 0.3\text{-}\mu\text{m}$ $\text{Al}_x\text{Ga}_{1-x}\text{As}$ ($x \sim 0.36$) confining layer. All layers are undoped ($n_d - n_a \leq 10^{15} \text{ cm}^{-3}$).

Six different QWH active regions composed of thin-layer phonon-generating arrays coupled to larger GaAs quantum wells ($L_z \leq 500 \text{ \AA}$) or standard DH active layers ($500 \text{ \AA} \leq L_z \leq 2000 \text{ \AA}$) are employed. They are (i) a single $L_{z1} \sim 200\text{-}\text{\AA}$ GaAs well and seven $L_{z2} \sim 50\text{-}\text{\AA}$ GaAs wells with all of the wells coupled by seven $\sim 50\text{-}\text{\AA}$ -thick $\text{Al}_x\text{Ga}_{1-x}\text{As}$ ($x \sim 0.32$) barriers [structure denoted as (1-7) 200 – 50 \text{\AA}],¹¹ (ii) a structure identical to (i) with the exception that the thicker GaAs layer is changed to $L_{z1} \sim 500 \text{ \AA}$ [(1-7) 500 – 50 \text{\AA}], (iii) a structure identical to (i) with the exception that the largest GaAs well is increased in size to $L_{z1} \sim 1500 \text{ \AA}$ [(1-7) 1500 – 50 \text{\AA}], (iv) a structure similar to (i) with $L_{z1} \sim 160 \text{ \AA}$, $L_{z2} \sim 80 \text{ \AA}$ and with $\sim 80\text{-}\text{\AA}$ -thick $\text{Al}_x\text{Ga}_{1-x}\text{As}$ ($x \sim 0.32$) coupling barriers [(1-7) 160 – 80 \text{\AA}], (v) a phonon-generating array of seven $L_{z2} \sim 50\text{-}\text{\AA}$ GaAs wells on either side of an $L_{z1} \sim 500\text{-}\text{\AA}$ GaAs layer all of which are coupled by fourteen $\sim 50\text{-}\text{\AA}$ -thick

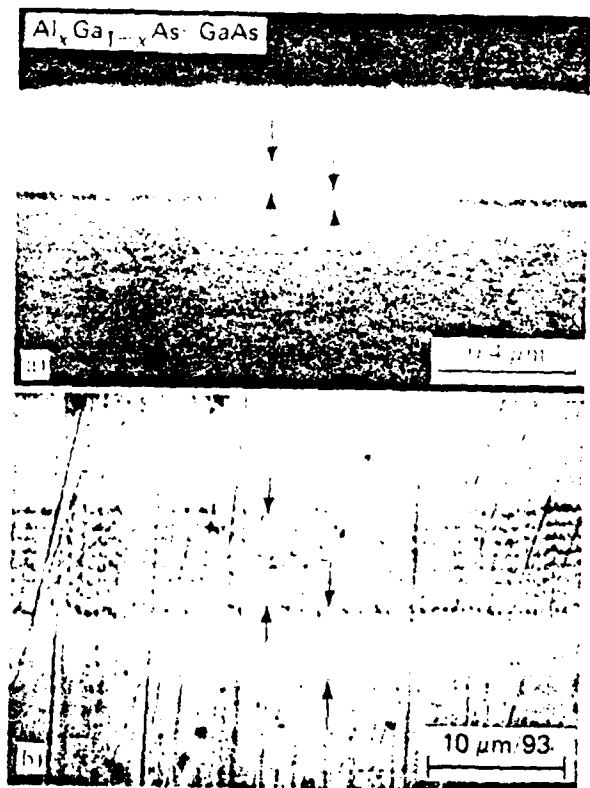


FIG. 2. Scanning-electron microscope photographs of a multiple-quantum-well heterostructure grown by MOCVD with an active region consisting of seven $50\text{-}\text{\AA}$ GaAs wells and one $500\text{-}\text{\AA}$ GaAs well coupled by seven $50\text{-}\text{\AA}$ $\text{Al}_x\text{Ga}_{1-x}\text{As}$ ($x \sim 0.32$) barriers. The cleaved and stained cross section (a) shows the $500\text{-}\text{\AA}$ GaAs layer (right-hand arrows); the left-hand arrows indicate the array of seven $50\text{-}\text{\AA}$ layers, which cannot be individually resolved. Photograph (b) shows a shallow-angle beveled and stained cross section of the same QWH. The shallow-angle bevel and stain causes the layers to appear enlarged (by a factor of 93 for this cross section), allowing the array of seven $50\text{-}\text{\AA}$ wells and seven $50\text{-}\text{\AA}$ barriers to be resolved (left-hand arrows).

Al_xGa_{1-x}As ($x \sim 0.32$) barriers [(7-1-7)50-500-50 Å], and (vi) two $L_{z1} \sim 120$ -Å GaAs wells with one located on either side of an array of six $L_{z2} \sim 80$ -Å GaAs wells with all of the GaAs layers coupled by seven ~ 80 -Å-thick Al_xGa_{1-x}As ($x \sim 0.32$) barrier layers [(1-6-1)120-80-120 Å]. In addition to the undoped wafers described above, four "degenerate" case multilayer structures in which all wells and barriers are the same thickness are used for comparison. These contain undoped active regions which include (a) six $L_z \sim 50$ -Å GaAs wells coupled by five ~ 50 -Å Al_xGa_{1-x}As ($x \sim 0.30$) barriers [(5 + 6) 50 Å or simply (6) 50 Å],¹² (b) four $L_z \sim 80$ -Å GaAs layers coupled by three ~ 80 -Å Al_xGa_{1-x}As ($x \sim 0.35$) barriers [(3 + 4) 80 Å or (4) 80 Å],¹³ (c) six $L_z \sim 80$ -Å-thick GaAs layers coupled by five ~ 80 -Å Al_xGa_{1-x}As ($x \sim 0.30$) barriers with one p -type and one n -type confining layer and a p -type GaAs contact layer to form a p - n junction QWH diode [(5 + 6) 80 Å or (6) 80 Å], and (d) six $L_z \sim 120$ -Å GaAs wells coupled by five ~ 120 -Å Al_xGa_{1-x}As ($x \sim 0.27$) barriers [(5 + 6) 120 Å or (6) 120 Å].¹⁴

Layer thicknesses of the QWH samples are estimated by SEM microphotographs taken on cleaved cross sections or on bevel cross sections ($\sim 1^\circ$ angle).¹⁵ Both of these forms of measurement agree with the growth rate calibration on thicker layers and with sputter-Auger measurements.¹⁶ The bevel angle, and thus also the magnification factor, is precisely determined using a SLOAN DEKTAK surface profilometer. Examples of a SEM microphotograph (a) on a cleaved and (b) on a beveled and stained cross section of the (1-7) 500-50 Å structure [ii] are shown in Fig. 2. Starting from the bottom of photomicrograph (a) is the ~ 1.0 - μm Al_xGa_{1-x}As ($x \sim 0.36$) confining layer. Next, between the right-hand pair of head-to-head arrows is the $L_{z1} \sim 500$ -Å GaAs layer. This is then followed by the seven $L_{z2} \sim 50$ -Å GaAs wells coupled by the ~ 50 -Å-thick Al_xGa_{1-x}As (~ 0.32) barriers, all of which are between the left-hand pair of head-to-head arrows. The individual ~ 50 -Å-thick layers in (a) are not resolvable. Finally, the uppermost portion is the second ~ 0.3 - μm Al_xGa_{1-x}As ($x \sim 0.36$) confining layer. Note that the "large" GaAs layer is indeed ~ 500 Å thick, while the net thickness of the multilayer region is $(7 + 7) \times 50 \text{ Å} = 700 \text{ Å}$. The (b) part of Fig. 2 is a SEM photomicrograph of a beveled ($\sim 0.62^\circ$, $\sim 93 \times$ magnification) and stained portion of the same (1-7) 500-50-Å wafer as that of (a). Here the individual ~ 50 -Å-thick layers, which comprise the multilayer phonon-generating array between the left-hand head-to-head arrows, are resolved as is also the ~ 500 -Å (L_{z1}) GaAs layer between the right-hand head-to-head arrows. The apparent layer nonuniformity and unevenness are due to scratches inherent in the bevel technique and in no way imply poor crystal quality.¹⁷

In order to study small samples with large Fabry-Perot cavity end losses, and undoped samples to avoid the confusion of recombination radiation involving impurities, photo-pumping is used for sample excitation. The data presented here are obtained using an Ar⁺ laser ($\lambda \sim 5145 \text{ Å}$) which can be operated either cavity-dumped or cw. Sample preparation¹⁸ consists of first mechanically polishing the wafer from

the substrate side down to a thickness of $\sim 50 \mu\text{m}$ and then selectively etching off¹⁸ the remaining GaAs substrate and buffer layer. The resulting thin (~ 1.4 - μm -thick) wafer is then cleaved into rectangular samples ~ 10 - $100 \mu\text{m}$ wide by ~ 100 - $300 \mu\text{m}$ long which are imbedded into In under a sapphire window for 77 K operation¹⁹ or into annealed Cu under diamond for 300 K operation.²⁰ Typically, a circular spot of Ar⁺ laser light comparable in diameter to the sample width is used to excite electron-hole pairs in the Al_xGa_{1-x}As confining layers. Since $\alpha L_z \ll 1$, most of the carriers are generated in the confining layers. The carriers diffuse to the active region where they thermalize by emitting LO phonons and then recombine. The one (5 + 6) 80-Å structure that is grown sandwiched between n - and p -type confining layers has been both fabricated into simple stripe-geometry laser diodes and has been processed into a photoluminescence sample by selectively etching off the GaAs substrate and contact layers.

III. EXPERIMENTAL DATA

The emission spectra of a large quantum well ($L_{z1} \geq 200 \text{ Å}$) coupled to an array of small wells ($L_{z2} \leq 80 \text{ Å}$) dif-

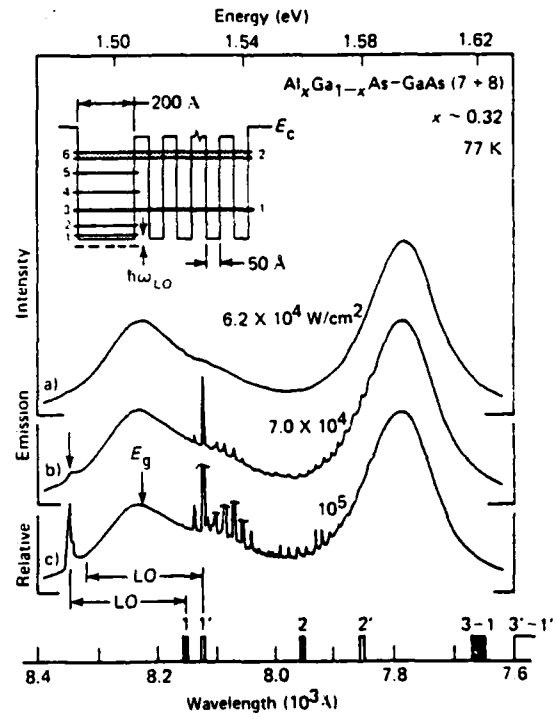


FIG. 3. Pulsed photoluminescence spectra (77 K) of a sample ($55 \times 488 \mu\text{m}^2$) cleaved from a heterostructure similar to that shown in Fig. 2 but with a 200-Å GaAs layer in place of the 500-Å layer. A one-dimensional model of the conduction band and the allowed electron energy levels are indicated by the inset. The heavy and light bars on the horizontal axis mark the transition energies for electrons to recombine with heavy holes ($e \rightarrow hh$, n confined-particle transitions) or with light holes ($e \rightarrow lh$, n' confined-particle transitions) respectively. The spontaneous spectrum shows the emission just below lasing threshold [a, $6.2 \times 10^4 \text{ W/cm}^2$]. At slightly higher excitation power [b, $7.0 \times 10^4 \text{ W/cm}^2$] the main laser mode occurs on the $n = 1'$ transition with the simultaneous occurrence of a small spectral bump at energy $\hbar\omega_{LO}$ below the $n = 1$ transition. At higher power [c, 10^5 W/cm^2] the small bump develops into a well-defined laser mode.

fer markedly from those of a single large well ($L_z \geq 200 \text{ \AA}$), or from a degenerate multilayer structure ($L_z \leq 80 \text{ \AA}$) in which all the quantum wells are the same thickness. The proximity ($\leq 80 \text{ \AA}$) of a larger well to an array (see the inset of Fig. 3) is very important in the electronic and vibrational coupling of the two systems. Both electrons, which have a significant tunneling probability for an $\sim 80\text{-\AA}$ -thick $\sim 400\text{-meV}$ rectangular barrier, and LO phonons, with a $100\text{-}500\text{-\AA}$ mean free path, are likely to be shared in the whole system and affect the recombination and inelastic scattering processes. For example, LO phonons generated in the small-well arrays of these heterostructures influence the recombination in the larger layers.

Typical emission spectra (77 K) of a photopumped, rectangular sample from the (1-7) 200-50- \AA wafer (i) are shown in Fig. 3. The form of the conduction-band edge in the vicinity of the active region is illustrated in the inset. The horizontal lines indicate the electron eigenenergies of this one-dimensional potential. These lines are sketched to correspond to the spatial extent of the wavefunctions. The numbers 1-6 on the left side of the lines and the 1 and 2 on the right side denote those states of the system which arise because of the $L_{z1} \sim 200\text{-\AA}$ -thick well and the $L_{z2} \sim 50\text{-\AA}$ multilayer, respectively. While this numbering scheme is not strictly correct for the complete coupled quantum system, it is very useful since some eigenfunctions are more localized in the $L_{z1} \sim 200\text{-\AA}$ well and others are more localized in the $L_{z2} \sim 50\text{-\AA}$ multilayer. Note that this localization should not restrict the motion of the electrons since the very-small-layer dimensions easily allow electron tunneling between the multilayer and the larger GaAs layer.

The (1-7) 200-50- \AA sample, when pulse excited ($6.2 \times 10^4 \text{ W/cm}^2$) partially across its width, exhibits the high-level spontaneous emission spectrum, Fig. 3(a). Spontaneous emission peaks are observed at slightly lower energies than the first electron-to-heavy-hole $n = 1$ confined-carrier transitions of both the multilayer array and the larger quantum well. With an increase in pump power to $7 \times 10^4 \text{ W/cm}^2$, Fig. 3(b), a laser mode appears abruptly near the first electron-to-light-hole $n' = 1'$ transition of the $L_{z1} \sim 200\text{-\AA}$ GaAs well, and *simultaneously* a small bump emerges $\sim \hbar\omega_{LO}$ lower in energy than the $n = 1$ $L_{z1} \sim 200\text{-\AA}$ confined-carrier transition. Upon further excitation [(c), 10^5 W/cm^2], this bump also lases although it is still much lower in intensity than the higher-energy confined-carrier stimulated emission. The location in energy and the unique manner of turn-on of the bump with the laser line are interpreted as evidence for stimulated phonon emission.

The emission spectrum (77 K) of a second sample from the (1-7) 200-50- \AA wafer is shown in Fig. 4. At low-level cw excitation [curve (a), 250 W/cm^2] the spontaneous emission peaks at very nearly the same energies as the sample of Fig. 3. For pulsed excitation, however, laser operation is observed [curve (b), $5 \times 10^4 \text{ W/cm}^2$] both on a phonon sideband of the lowest-confined-carrier transitions and also near the $n = 2$ transition of the $L_{z1} \sim 200\text{-\AA}$ well. Note that with this sample and excitation geometry the phonon-sideband laser modes can be made to dominate the emission spectrum as opposed to the relatively weak modes at that energy shown

in Fig. 3. That this effect is primarily due to the excitation geometry can be seen by comparing the spectrum of Fig. 4 with that of Fig. 3(b) of Ref. 8. Both spectra are from the same cleaved sample ($28 \times 244 \mu\text{m}^2$) and are excited to the same level ($5 \times 10^4 \text{ W/cm}^2$). However, the pump beam is at a slightly different location of the sample in the two cases: this results in the relative emission intensities of the phonon sideband and the higher-energy laser modes to be different.

As mentioned earlier, this type of emission spectrum, i.e., with stimulated emission occurring $\sim \hbar\omega_{LO}$ lower in energy than the lowest-confined-carrier transition, is not similar to that of a single $\sim 200\text{-\AA}$ -thick well. Depending on sample and pump beam geometry and also the excitation power, laser action has occurred over a very broad energy range in a single $L_z \sim 200\text{-\AA}$ QWH (see Fig. 10 of Ref. 6). However, it has not been observed as low in energy as $\sim \hbar\omega_{LO}$ below the lowest ($n = 1, n' = 1'$) confined-carrier transitions. A direct comparison of pulse-excited room-temperature laser operation of a single $L_z \sim 200\text{-\AA}$ QWH and the (1-7) 200-50- \AA QWH (i) of Figs. 3 and 4 is shown in Fig. 5. At $2.8 \times 10^4 \text{ W/cm}^2$ the single well structure, curve (a), exhibits considerable bandfilling^{6,21} because of its very small active region thickness and relative inability to collect and thermalize hot electrons from the confining layers.^{6,22} Upon coupling of a phonon-generating and reflecting array of smaller $L_{z2} \sim 50\text{-\AA}$ GaAs layers to a single $L_{z1} \sim 200\text{-\AA}$ -thick GaAs well, we observe [curve (b), $7 \times 10^4 \text{ W/cm}^2$] that the carrier collection, thermalization, and bandfilling problems are drastically reduced. Most of the carriers are collected by and scatter to lower energy in the multilayer portion (64% of the GaAs

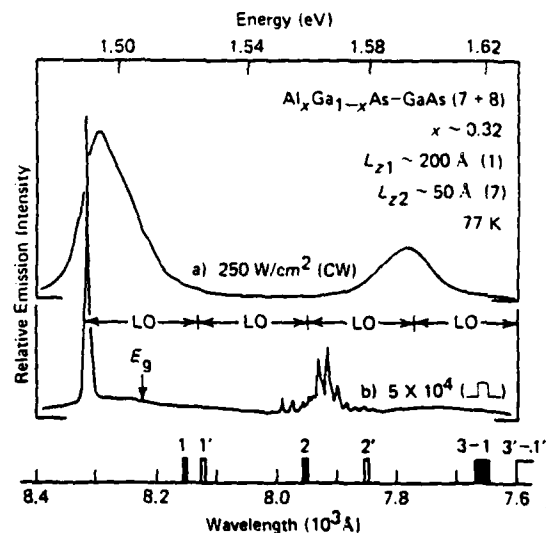


FIG. 4. Spectra (77 K) of a photopumped sample ($28 \times 244 \mu\text{m}^2$) cleaved from the same wafer as that of Fig. 3. Low-level cw excitation [a], 250 W/cm^2] produces a peak at energy $\hbar\omega_{LO}$ below the $n' = 1'$ transitions of the 200- \AA well and another peak ($\lambda \sim 7800 \text{ \AA}$) approximately an LO-phonon below the $n' = 1'$ transitions of the 50- \AA wells. (The $n = 1$ transitions of the 50- \AA well are degenerate with the $n = 3$ transition of the 200- \AA well; see inset of Fig. 3.) Pulsed excitation [b], $5 \times 10^4 \text{ W/cm}^2$] results in laser operation an LO phonon below the $n = 1$ transitions of the 200- \AA well. Smaller laser modes also appear near the $n = 2$ transitions of the 200- \AA well.

in the active region is in the multilayer array) of the heterostructure. In the process, LO phonons are emitted and carriers either recombine or scatter to still lower energy in the larger well and recombine. For the samples of Figs. 3, 4, and 5(b) ($7 \times 10^4 \text{ W/cm}^2$), a sizable portion of the carriers scatter to the lowest-energy confined-carrier states before recombining radiatively, including at energy $\hbar\omega_{\text{LO}}$ below the $n = 1$ or $1'$ transitions. Although other excitation geometries modify the emission spectra of a (1-7) 200-50-Å QWH, these data demonstrate that this design of the active region enables recombination to be observed at lower energies than for the case of a single $L_z \sim 200$ -Å-thick well, or even an $L_z \sim 50$ -Å multilayer array, and that LO-phonon effects therefore play a considerable role in the operation of this form of QWH.

A further interesting feature of the (1-7) 200-50-Å QWH is the presence of emission and laser modes in the range between the lowest-energy confined-carrier transitions of the system and the phonon sidebands. This is demonstrated clearly in the 77 K photoluminescence spectra of Fig. 6. As with the spontaneous emission data of Figs. 3, curve (a), and 4, curve (a), the CW emission at low level [Fig. 6 curve (a), 10 W/cm^2] of this wafer peaks at slightly lower energies than the $n = 1$ confined-carrier transitions of the $L_{z1} \sim 200$ -Å well. In addition, in the case of this sample a shoulder in the emission is observed $\sim 20 \text{ meV}$ lower in energy than the $n = 1$ transition of the $L_{z1} \sim 200$ -Å well. At

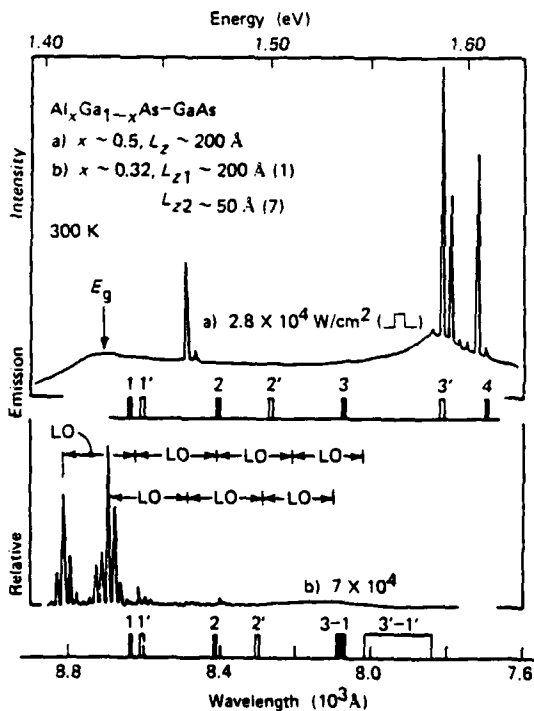


FIG. 5. Comparison of the pulsed photoemission (300 K) of a rectangular sample ($47 \times 234 \mu\text{m}^2$) cleaved from a single 200-Å QWH with a rectangular sample ($62 \times 226 \mu\text{m}^2$) cleaved from the same QWH wafer as the samples of Figs. 3 and 4. The high energy emission a) of a single 200-Å QWH ($2.8 \times 10^4 \text{ W/cm}^2$) is cut off by the 7-well ($L_{z2} \sim 50 \text{ Å}$) array of b) ($7 \times 10^4 \text{ W/cm}^2$).

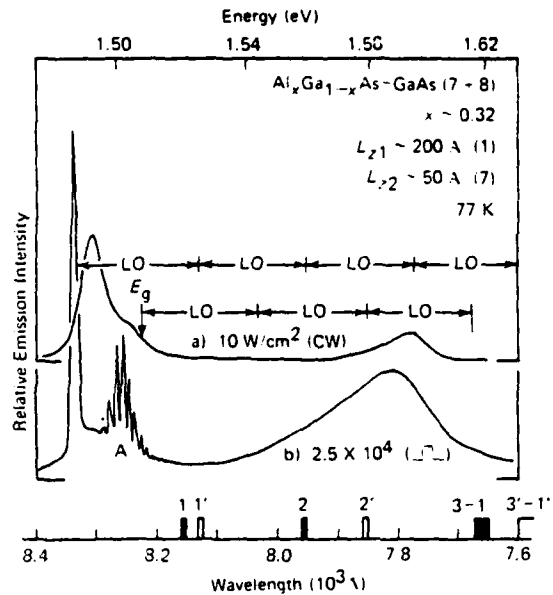


FIG. 6. Photoemission (77 K) of a sample ($94 \times 234 \mu\text{m}^2$) cleaved from the same wafer described in Fig. 3. Besides the low-level (250 W/cm^2) spontaneous peaks of Fig. 4, the low-level spectrum a) (10 W/cm^2) exhibits a shoulder approximately 20 meV below the $n = 1$ transition, corresponding to the expected binding energy of a two-dimensional exciton in GaAs. At higher power [b), $2.5 \times 10^4 \text{ W/cm}^2$] a well-defined group of laser modes (labeled A, 20 meV below the $n = 1$ marker) appears as well as laser operation one phonon below the $n' = 1'$ transition.

higher pulsed photoexcitation [curve (c), $2.5 \times 10^4 \text{ W/cm}^2$], laser operation is observed both on a phonon-sideband of the $n' = 1'$ transition and also $\sim 20 \text{ meV}$ below the $n = 1$ transition, labeled A. The location of A is in excellent agreement with the energy expected of a two-dimensional exciton involving a heavy hole.

The binding energy of a two-dimensional exciton is $4 \times$ larger than for the three-dimensional limit.^{23,24} This results in two-dimensional-exciton binding energies of $\sim 20 \text{ meV}$ for the electron-heavy-hole exciton and $\sim 13 \text{ meV}$ for the electron-light-hole exciton.²⁵ The $4 \times$ increase over the three-dimensional case is expected in the limit of two-dimensional confinement and will be reduced to $1 \times$ as the layer thickness is increased to the bulk limit. For layer thicknesses less than the bulk-exciton diameter ($\sim 240 \text{ Å } e-hh$, $\sim 340 \text{ Å } e-lh$), the factor of $4 \times$ continues to agree well with photoluminescence data; this is in contrast to earlier absorption measurements (on crystals grown by MBE) that indicate an enhancement of only $\sim 2 \times$ in the exciton binding energy for $L_z < 100 \text{ Å}$.²⁶ The data of Fig. 6 and other low-level cw and laser data²⁵ on rectangular cleaved samples indicate that the two-dimensional exciton can be involved in recombination in these quantum-well heterostructures.

In order to determine how closely the low-energy phonon-sideband laser modes observed in the data from the (1-7) 200-50-Å QWH (Figs. 3-6) are related to the confined-carrier transitions, a number of samples with a thicker GaAs layer substituted in place of the "large" $L_{z1} \sim 200$ -Å well have been employed. As the layer size L_{z1} is increased, the

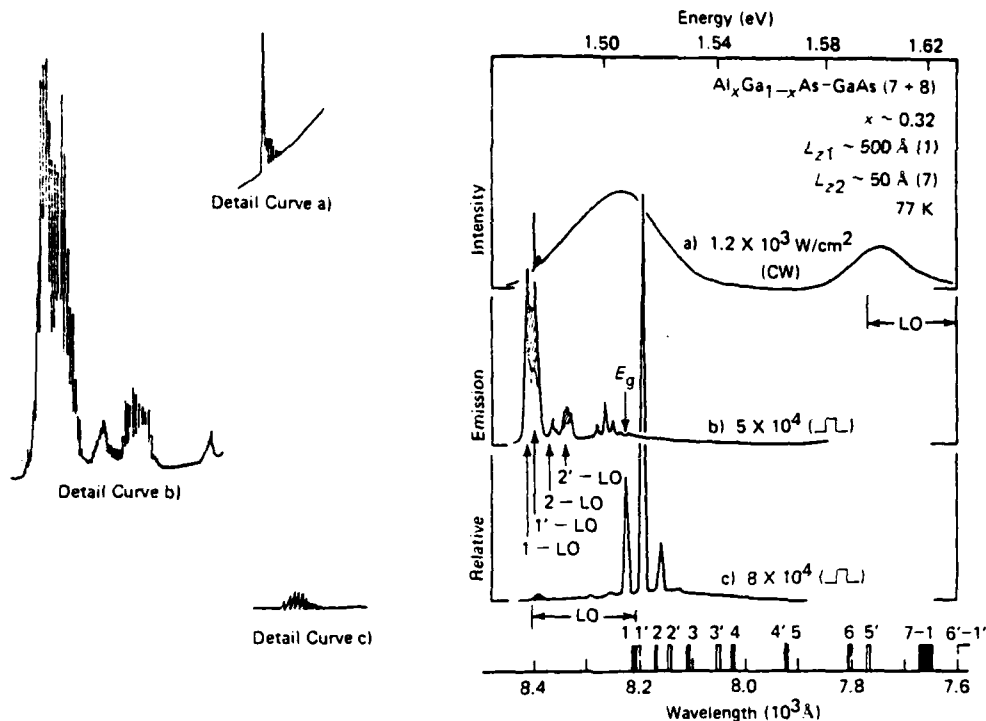


FIG. 7. Induced phonon-assisted recombination (77 K) of the QWH shown in the cross section of Fig. 2. cw emission from a photopumped rectangular sample ($59 \times 254 \mu\text{m}^2$) peaks near the $n' = 1'$ transitions of the 50-Å wells ($\lambda \sim 7800 \text{ \AA}$) and slightly below the $n = 1$ transition of the the 500 Å well [(a), $1.2 \times 10^3 \text{ W/cm}^2$]. At higher excitation [(b), $5 \times 10^4 \text{ W/cm}^2$] laser operation occurs one phonon (ω_{LO}) below the confined-particle transitions 1, 1', 2, 2', 3, and 3'. A narrower sample ($23 \times 211 \mu\text{m}^2$) lases across the sample on the lowest transitions [(c), $8 \times 10^4 \text{ W/cm}^2$] with some end-to-end closely spaced modes apparent one phonon below the $n' = 1'$ transition.

behavior of the larger well shifts more toward bulk GaAs; the confined-carrier states then become very closely spaced and the $n = 1$ transition is very nearly degenerate with E_g . The uncertainty in assigning an edge or origin for phonon-sideband laser operation is thus greatly decreased. This is the case for $L_{z1} \sim 500 \text{ \AA}$.

An example of the emission spectra (77 K) of the (1-7) 500-50-Å QWH sample (ii) is shown in Fig. 7. The cw spectrum [curve (a), $1.2 \times 10^3 \text{ W/cm}^2$] exhibits laser operation on a phonon sideband of the $n' = 1'$ transition of the 500-Å quantum well. Spontaneous emission peaks as seen in Figs. 3, 5, and 6 are also observed. At a pulsed excitation of $5 \times 10^4 \text{ W/cm}^2$, curve (b), the same sample lases strongly in the range of the phonon sidebands of the $n = 1, 1', 2, 2', 3,$ and $3'$ transitions of the $L_{z1} \sim 500\text{-\AA}$ layer. A narrower sample [curve (c), $8 \times 10^4 \text{ W/cm}^2$], with higher cavity losses, is used to force laser operation up in energy to the lowest confined-carrier transitions to enable their identification.

A design modification on the (1-7) 500-50-Å QWH is achieved by introducing a second phonon-generating and -reflecting array of seven $L_{z2} \sim 50\text{-\AA}$ quantum wells on the other side of the $L_{z1} \sim 500\text{-\AA}$ -thick GaAs layer. The result is a (7-1-7) 50-500-50-Å structure in which $\sim 58\%$ of the GaAs in the active region is in the small-well array portion. Any reflection of LO phonons by the twin 50 Å-well arrays should tend to localize the LO phonons in the vicinity of the $L_{z1} \sim 500\text{-\AA}$ -thicker layer and strongly affect the recombination radiation spectrum. Typical pulsed room-temperature photoluminescence spectra are shown in Fig. 8. The bars numbered 1-5 are the locations of the five lowest-energy electron-to-heavy-hole transitions of the 500-Å quantum well. At 10^4 W/cm^2 , curve a), laser threshold occurs $\sim \hbar\omega_{\text{LO}}$

lower in energy than the $n = 1$ transition. Slight ringing is also observed in the energy range of the $n = 2$ transition. An increase in excitation level to $2 \times 10^4 \text{ W/cm}^2$, curve b), results in intense laser operation on the phonon sideband of the lowest confined-particle transitions and also weaker laser modes between the $n = 1$ and $n = 4$ transitions. Note that the data of Figs. 7 and 8 exhibit laser operation $\sim \hbar\omega_{\text{LO}}$ lower in energy than the lowest-energy laser emission expected due to band-to-band recombination in bulk, undoped GaAs. This emission occurs at a transition energy in which no states exist in these structures. As mentioned earlier, both of these samples are undoped ($n_d - n_a \leq 10^{15} \text{ cm}^{-3}$). Therefore this laser operation is not impurity related, since $\approx 10^{17} \text{ cm}^{-3}$ impurities are necessary for GaAs to lase on a band-to-impurity transition.²⁷ The emission spectra of Figs. 7 and 8 establish that phonon-sideband laser operation can be achieved in a GaAs laser of nearly bulk dimensions ($\sim 500 \text{ \AA}$) that is sandwiched between $\text{Al}_x\text{Ga}_{1-x}\text{As}$ confining layers.

Further increase in the size of the larger GaAs well in these coupled array heterostructures begins to decrease the effectiveness of the laser operation of the larger layer. For these heterostructures (inset of Fig. 3), as the single larger well (L_{z1}) is increased in size from 200 to 500 to 1500 Å, the GaAs fraction in the active region represented by the $L_{z2} \sim 50\text{-\AA}$ seven-well array decreases from 0.64 to 0.41 to 0.19. Assuming that this is roughly the percent of injected electrons that thermalize in the small-well array section, we expect the number of LO phonons generated by the seven well $L_{z2} \sim 50\text{-\AA}$ array to decrease rapidly with increasing L_{z1} . Note that the fraction of electrons that recombine in the array is expected to be even less than the above estimate since carriers can tunnel into the larger GaAs layer and scatter to

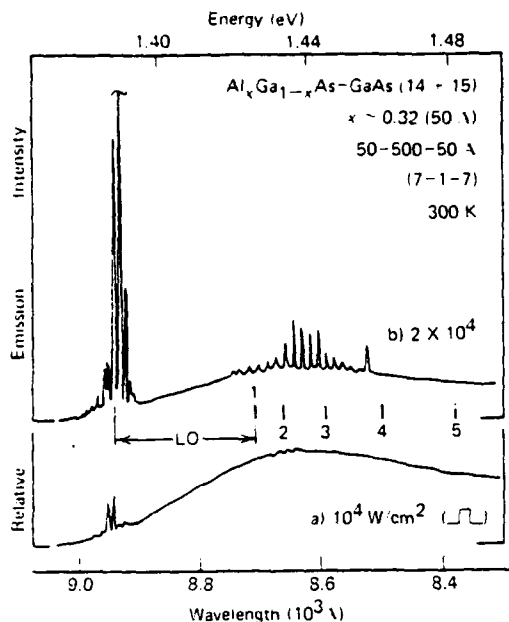


FIG. 8. Pulsed room-temperature laser operation of a rectangular ($68 \times 234 \mu\text{m}^2$) QWH sample with an active region consisting of a 500-Å GaAs well sandwiched between two arrays of seven 50-Å GaAs wells all of which are coupled by 50-Å Al_xGa_{1-x}As ($x \approx 0.32$) barriers. At 10^4 W/cm^2 (a) spontaneous emission is peaked in the range of the lowest transitions of the 500-Å well ($n = 1-4$) with laser modes developing one phonon below the $n = 1$ transition (located almost at E_g). At $2 \times 10^4 \text{ W/cm}^2$, (b) the laser operation is well developed one phonon below the $n = 1$ transition (or E_g), and weaker laser emission is observed between the $n = 1$ and $n = 4$ transitions of the 500-Å well.

still lower energy before recombining. Therefore, in spite of the fact that the small-well array contributes some recombination radiation, which can serve as a reference, this radiation is relatively weak and has little effect on the lasing behavior of the larger GaAs layer for $L_{z1} < 500 \text{ Å}$.

Pulsed room-temperature laser operation of the (1-7) 1500-50-Å QWH sample (iii) is shown in Fig. 9. Since the single $L_{z1} \sim 1500\text{-Å}$ -GaAs layer (coupled to the L_{z2} 50-Å array) is definitely in the bulk limit, only the GaAs energy gap E_g is used as a reference for emission originating in the thick layer. The 1 and 1' bars near 8000 Å in Fig. 9 denote the energies of the first electron-to-light- and -to-heavy-hole transitions for carriers localized in the $L_{z2} \sim 50 \text{ Å}$ seven-well multilayer. One interesting feature of the data in Fig. 9 is the relatively weak spontaneous emission peak located $\sim \hbar\omega_{LO}$ lower in energy than the $L_{z2} \sim 50\text{-Å}$ multilayer transitions $n = 1$ and $n' = 1'$. This emission is weak because of the small fraction (0.19) of the active region GaAs that is contributed by the 50-Å array. The most important feature of this sample is that it too lases at energies below E_g , as far below as $\sim \hbar\omega_{LO}$. At 77 K this heterostructure lases²⁸ at E_g and also exhibits the higher-energy spontaneous reference peak of Fig. 9. This peak, however, is not shifted below the $L_{z2} \sim 50\text{-Å}$ $n = 1$ transition as it is at 300 K, but rather occurs very nearly on the $n = 1$ transition. That both the multilayer array and the larger-layer emission shift down in energy relative to their band-to-band transitions as the lattice

temperature is increased indicates that the thermal LO-phonon occupation number is increased enough to cause both transitions to operate on phonon sidebands. A further experiment on a DH wafer with $L_z \sim 600 \text{ Å}$ (all layers undoped, $n_d - n_a \leq 10^{15} \text{ cm}^{-3}$) has exhibited a similar temperature dependence.²⁸ Therefore laser operation at $\hbar\omega \sim E_g - \hbar\omega_{LO}$ in a DH is considered as originating in phonon-assisted recombination. The thermal phonons present due to the lattice temperature (300 K) plus the nonthermal LO phonons generated during carrier relaxation are sufficient to produce phonon-sideband laser operation at the high injection levels characteristic of DH laser operation.

While the data of Fig. 9 indicate that phonon-sideband laser operation can be induced by changing the thermal LO-phonon occupation number, the spectra of Fig. 10 demonstrate that a similar result can be achieved by increasing the nonthermal phonon occupation number. The cw room-temperature laser spectra of Fig. 10 have both been obtained on samples from an $L_z \sim 80\text{-Å}$ six-well, five-barrier ($x \sim 0.30$) QWH. This undoped multiple quantum-well active region ($n_d - n_a \leq 10^{15} \text{ cm}^{-3}$) is imbedded in an Al_xGa_{1-x}As ($x \sim 0.4$) p - n junction. The (a) spectrum is from a portion of the wafer processed into simple stripe geometry diodes. In contrast, the (b) spectrum is from a smaller portion of the wafer from which both the n -type GaAs substrate and also the p -type GaAs contact layers have been removed. Note that the diode, 10(a), operates on the phonon-sideband of the $n' = 1'$ transition, while the photoexcited sample operates at

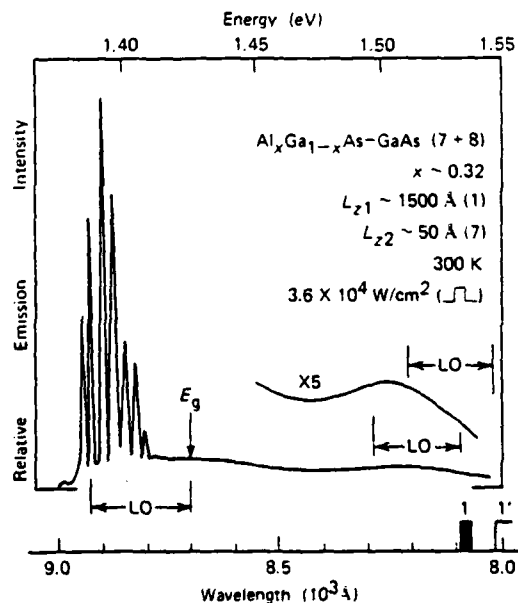


FIG. 9. Pulsed room-temperature photoemission ($3.6 \times 10^4 \text{ W/cm}^2$) of a sample ($43 \times 94 \mu\text{m}^2$) whose active region consists of a 1500-Å layer of GaAs (bulk dimensions) coupled to an array of seven 50-Å GaAs wells. The coupling barriers are 50-Å Al_xGa_{1-x}As ($x \approx 0.32$). A reference spontaneous spectral bump occurs between the 1-LO and 1'-LO transitions of the 50-Å array, and the sample lases in the range $\hbar\omega_{LO}$, below the energy gap of bulk material, indicating (from the 50-Å-array reference) that phonon-assisted recombination contributes to emission in heterostructures with layers as thick as 1500 Å.

much lower energy, $\sim 2x\hbar\omega_{LO}$ below the $n = 1$ transition. The important difference between the diode and the photoluminescence sample, other than the method of excitation, is the optical cavity size. The diode is $223 \mu\text{m}$ long, while the photoexcited sample is $22 \mu\text{m}$ in width and has nearly ten times larger cavity end loss than the diode. Two factors enter into the laser operation of very narrow samples: (1) bandfilling tends to increase the lasing energy, and (2) the increased density of electron-hole-pairs necessary to attain laser threshold gives rise to an increase in the nonthermal LO phonon occupation number and increases the probability of phonon-assisted laser operation, thus decreasing the lasing energy. In order to achieve laser threshold [10(a), $\sim 2.4 \times 10^3 \text{ A/cm}^2$; 10(b), $\sim 7.9 \times 10^3 \text{ A/cm}^2$ equivalent current density], the narrow photoexcited sample must be driven to more than three times the power density necessary for laser operation of the diode. Therefore in this sample the larger nonthermal phonon occupation number made possible by the higher laser threshold density induces lower-energy phonon-assisted laser operation.

While the data of Figs. 3-10 have focused on the laser behavior of QWH's, the low-level spontaneous emission spectra of these samples also provide insight into the QWH behavior. Typical 77 K spontaneous emission spectra for six

various QWH's are shown in Fig. 11. Curves (a), (b), and (c) are from the quantum-well structures consisting of a large GaAs quantum well [or wells as in (c)] coupled to a phonon-generating and -reflecting array of thinner GaAs layers. The remaining three spectra are from degenerate-case structures of uniform layer thickness [curve (d), six wells + five barriers, $L_z \sim 120 \text{ \AA}$; curve (e) four wells + three barriers, $L_z \sim 80 \text{ \AA}$; curve (f), six wells + five barriers, $L_z \sim 50 \text{ \AA}$] and serve as comparisons for the emission from the first three QWH's. The confined-carrier transitions are labeled for each spectrum, as are phonon spacings, and the two-dimensional exciton transitions relative to $n = 1$ (A) and to $n' = 1'$ (B).

A noticeable feature of these spectra is that the samples containing GaAs layers of different sizes (L_{z1} and L_{z2}) exhibit two emission peaks, one related to each well size, while the degenerate case samples [curves (d), (e), (f)] each have one dominant peak. Only in the case of the six-well (6) 50- \AA degenerate structure, curve (f) is the spontaneous peak lower ($2x\hbar\omega_{LO}$) in energy than the lowest confined-carrier transition ($\lambda \sim 7600 \text{ \AA}$). This behavior is possibly due to the better phonon confinement that is believed to exist in a 50- \AA -layer QWH as discussed below. It is interesting to compare this emission [(f), six-well, $L_z \sim 50 \text{ \AA}$] with that of the (1-7) 200-50- \AA structure, curve (a), which also contains a 50- \AA multilayer array. Note that the spontaneous emission from the multilayer array portion of curve (a), $\lambda \sim 7800 \text{ \AA}$, is not as low in energy as that from the degenerate case curve (f), $\lambda \sim 8000 \text{ \AA}$, indicating that the carriers in the (1-7) structure are more likely to scatter to the 200 \AA well than recombine on a sideband $2x\hbar\omega_{LO}$ lower in energy than the 50- \AA $n = 1$ transitions.

An important feature of these spectra is that the existence of two peaks in the (1-7) and (1-6-1) QWH's are likely (because of spectral broadening) to lead to relatively inefficient laser operation of these structures. The broadening of the emission into two peaks is due to the spatial separation of the electron-hole pairs in the QWH (in L_{z1} and in nL_{z2}). This broadened emission implies both a spatial and an energetic line broadening (an inhomogeneous line). As the L_{z1} and L_{z2} GaAs layer sizes are chosen to approach the same thickness [(a) to (b) to (c)], the broadening in the emission is decreased until finally the degenerate case [$(L_{z1} = L_{z2} = L_z)$; (d), (e), and (f)] results. Thus while the case of nondegenerate structures can be designed to demonstrate LO-phonon effects and are interesting light emitters, their usefulness as efficient lasers is questionable because the emission linewidth is artificially broadened.

IV. DISCUSSION

A complete theoretical description of the effects described above is difficult for several reasons. For example, not much is known about the mean free path of phonons under the condition of high excitation,²⁹ or about multiphonon emission, or in general about indirect optical transitions in a direct semiconductor. Usually it is agreed that indirect transitions, i.e., transitions involving phonons and photons, are negligible in direct materials if the electron-phonon coupling constant is small as it is in GaAs.³⁰ This

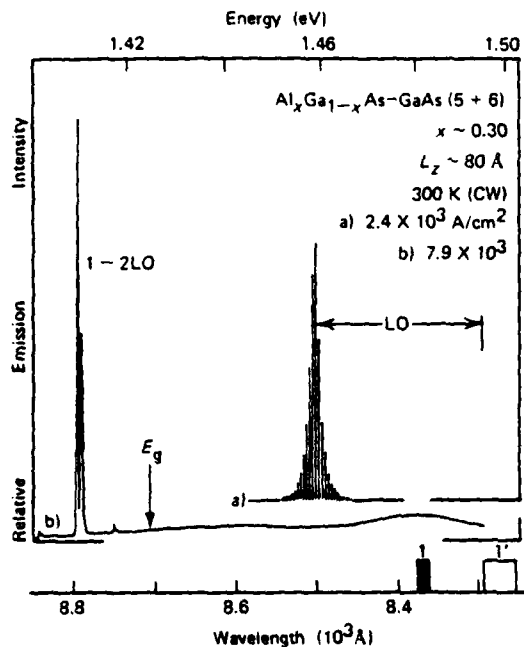


FIG. 10. Comparison of cw room-temperature laser operation of a diode and a photoexcited sample from the same QWH material. The active region consisting of six 80- \AA GaAs quantum wells separated by five 80- \AA Al_xGa_{1-x}As ($x \approx 0.30$) barriers is undoped ($n_d = n_a < 10^{15} \text{ cm}^{-3}$) and is sandwiched between an n - and p -type confining layer of Al_xGa_{1-x}As ($x \approx 0.40$). The diode [a], $2.4 \times 10^3 \text{ A/cm}^2$ lases $\hbar\omega_{LO}$ below the $n' = 1'$ transition, while the photopumped sample [b], $7.9 \times 10^3 \text{ A/cm}^2$, with the substrate and contact layers removed, lases at energy $2\hbar\omega_{LO}$ below the $n = 1$ transition (1-2LO transition). Note also the spontaneous bump near the $n = 1$ transition on the photopumped emission spectrum.

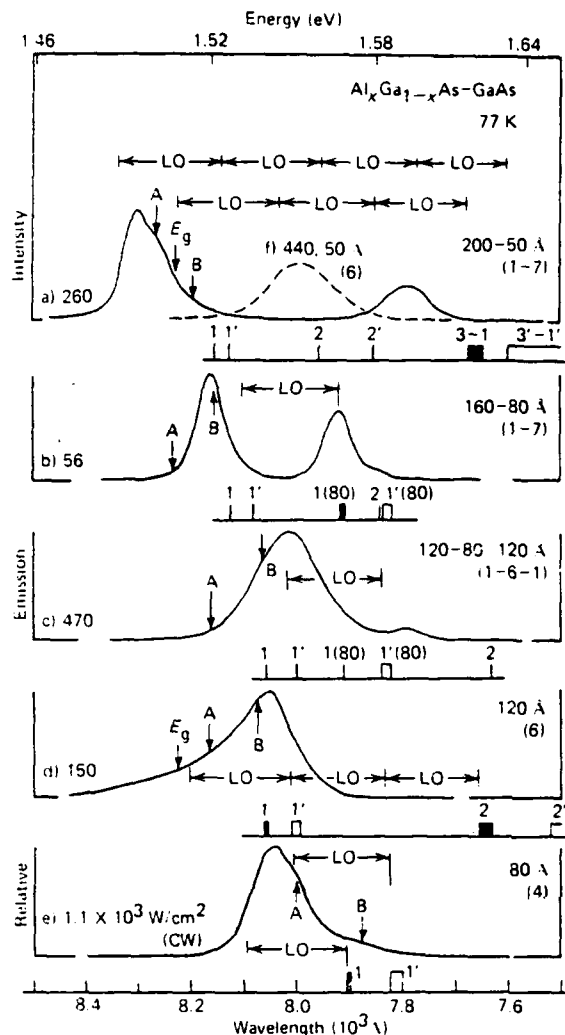


FIG. 11. Photopumped spontaneous emission spectra (cw, 77 K) of six different multiple-quantum-well heterostructures. The arrows marked A are located 20 meV below the $n = 1$ electron-to-heavy-hole transitions, corresponding to the estimated binding energy of a two-dimensional electron-heavy-hole exciton. Similarly, the arrows marked B are located 13 meV below the $n = 1'$ electron-to-light-hole transitions, corresponding to the estimated binding energy of a two-dimensional electron-light-hole exciton. The confined-particle-transition markers for each heterostructure are located beneath each spectrum; the active-layer structure is designated to the right of each spectrum. For example, spectrum a) (260 W/cm^2) is from a heterostructure with an active region consisting of one 200-Å GaAs well and seven 50-Å GaAs wells, all of which are coupled by 50-Å Al_xGa_{1-x}As barriers.

argument does not hold for high excitation levels since the average phonon occupation number which appears in the matrix elements for indirect transitions increases rapidly, resulting in a high "effective" electron-phonon interaction.

This should be generally true and the effect should give important contributions to the optical constants under high excitation conditions, for example, as encountered in the parallel case of laser annealing. Before describing our choice of sample geometries to enhance the phonon effects, we would like to emphasize that previous studies have shown that size-quantization effects tend to favor a nonthermal phonon occupation. This occurs because of the two-dimensional density of states,² a slight increase in the electron-

phonon coupling constant,⁷ and the high-power densities "compressed" into a relatively small volume^{2,6,28} (the QWH active region). Below we describe the criteria that have guided the choice of the sample geometry.

In spite of the fact that not much is known about phonon-phonon interactions, the phonon mean free path at high excitation levels, and the direction of maximum emission intensity, we assume that layers with dimensions of a multiple of the phonon wavelength at the maximum phonon intensity would reflect and confine most. The wavelength of maximum intensity of phonons emitted perpendicular to the layers can be determined in the following way: Previous calculations⁸ show that the emission probability for phonons (perpendicular to the layers) is a monotonically decreasing function of q if free-carrier screening is not taken into account. A two-dimensional analysis shows that all wavelengths longer than $2a_b^* \approx 160 \text{ Å}$ are effectively screened, where a_b^* is the effective Bohr radius. Therefore we expect a maximum in the phonon intensity at wavelengths near $2a_b^*$. The emission probability parallel to the layers (again for quasi-two-dimensional electrons) shows two distinct peaks.⁸ The peak at the longer wavelength is again almost certainly screened. The peak at the shorter wavelength occurs as given in Ref. 8 at

$$q = 2.52 \times 10^{-6} m^{1/2} [1 + (1 - 1/m)^{1/2}] \text{ cm}^{-1}. \quad (1)$$

Here we have used the material constants of GaAs. The integer m corresponds to the energy $m\hbar\omega_{\text{LO}}$ above the bottom of the quantum-well subband from where the electron cascades downward in thermalizing. Using the above expression, we obtain as a typical wavelength and thus layer or well size the values shown in Table I. These values have been used as guidelines in the choice of sample dimensions.

V. CONCLUSIONS

A series of experiments have been described above to determine the extent of LO-phonon contribution to metalorganic chemical vapor deposited Al_xGa_{1-x}As-GaAs quantum-well-heterostructure (QWH) laser operation. The undoped photoluminescence structures studied have active regions consisting of a large GaAs quantum well (L_{z1}), or in some cases a bulk layer ($L_{z1} > 500 \text{ Å}$), coupled to a small-well (L_{z2}) multilayer array. Phonons generated during carrier

TABLE I. Phonon wavelengths at which the emission probability parallel to QWH layers exhibits a short wavelength peak (Eq. 1). (Owing to screening, longer wavelength peaks are not included. The $m = 1$ $\lambda \sim 250 \text{ Å}$ phonon is also expected to be screened while the rest are not.)

m	$\lambda = 2\pi/q \text{ (Å)}$
1	250
2	103
3	79
4	67
5	58
6	53
7	49
8	45
9	42
10	40

thermalization in the multilayer array have been shown to induce phonon-sideband laser operation of the larger GaAs layer. In undoped structures with the large-well dimension $L_{z1} \sim 500\text{\AA}$, the phonon-sideband emission is in the range $\hbar\omega \sim E_g - \hbar\omega_{LO}$; that is, the emission is $\sim \hbar\omega_{LO}$ lower in energy than the lowest transition allowed in bulk (undoped) GaAs. Phonon-sideband laser operation has been shown to be induced by an increase in either the thermal or the non-thermal LO-phonon occupation number. In fact, the increase in the thermal phonon occupation number at 300 K over that at 77 K has been shown to result in phonon-sideband laser operation of a bulk GaAs active layer in the size range of standard double heterojunctions ($L_{z1} \sim 1500\text{\AA}$). While these heterostructures, which contain a large quantum well coupled to a thin multilayer array, are useful in understanding phonon-sideband laser operation, they are not likely to be the most efficient lasers because of the artificially created line broadening resulting from two different quantum-well sizes. The MO-CVD QWH wafers used in this work have been designed to optimize the auxiliary phonon-generating and -reflecting arrays coupled to the larger GaAs quantum-well active layers. The optimization has been accomplished by choosing the array layer size equal to the wavelengths of the phonons with maximum emission probability.

ACKNOWLEDGMENTS

The authors are grateful to Yuri S. Moroz, R. T. Gladin, B. L. Marshall, and B. L. Payne (Urbana) for technical assistance, and to G. E. Stillman for helpful discussions. The work of the Illinois group has been supported by NSF Grants DMR 79-09991 and DMR-77-23999 and Navy Contract N00014-79-C-0768; the work of the Rockwell group has been partially supported by the Office of Naval Research, Contract N00014-78-C-0711.

¹N. Holonyak, Jr., R. M. Kolbas, W. D. Laidig, M. Altarelli, R. D. Dupuis, and P. D. Dapkus, *Appl. Phys. Lett.* **34**, 502 (1979).

²N. Holonyak, Jr., R. M. Kolbas, W. D. Laidig, B. A. Vojak, K. Hess, R. D. Dupuis, and P. D. Dapkus, *J. Appl. Phys.* **51**, 1328 (1980).

- ³E. A. Rezek, R. Chin, N. Holonyak, Jr., S. W. Kirchoefer, and R. M. Kolbas, *Appl. Phys. Lett.* **35**, 45 (1979).
- ⁴E. A. Rezek, R. Chin, N. Holonyak, Jr., S. W. Kirchoefer, and R. M. Kolbas, *J. Electron. Mater.* **9**, 1 (1980).
- ⁵R. Chin, N. Holonyak, Jr., and B. A. Vojak, *J. Appl. Phys.* **51**, 4017 (1980).
- ⁶N. Holonyak, Jr., R. M. Kolbas, R. D. Dupuis, and P. D. Dapkus, *IEEE J. Quantum Electron.* **QE-16**, 170 (1980).
- ⁷K. Hess, *Appl. Phys. Lett.* **35**, 484 (1979).
- ⁸K. Hess, N. Holonyak, Jr., W. D. Laidig, B. A. Vojak, J. J. Coleman and P. D. Dapkus, *Solid State Commun.* **34**, 749 (1980).
- ⁹H. Manasevit, *J. Electrochem. Soc.* **118**, 647 (1971).
- ¹⁰R. D. Dupuis and P. D. Dapkus, *Seventh International Symposium on GaAs and Related Compounds, St. Louis, 1978*, edited by C. M. Wolfe (Institute of Physics, London, 1979), pp. 1-9.
- ¹¹J. J. Coleman, P. D. Dapkus, B. A. Vojak, W. D. Laidig, N. Holonyak, Jr., and K. Hess, *Appl. Phys. Lett.* **37**, 15 (1980).
- ¹²R. M. Kolbas, N. Holonyak, Jr., B. A. Vojak, K. Hess, M. Altarelli, R. D. Dupuis, and P. D. Dapkus, *Solid State Commun.* **31**, 1033 (1979).
- ¹³N. Holonyak, Jr., R. M. Kolbas, W. D. Laidig, B. A. Vojak, R. D. Dupuis, and P. D. Dapkus, *Appl. Phys. Lett.* **33**, 737 (1978).
- ¹⁴B. A. Vojak, N. Holonyak, Jr., R. Chin, E. A. Rezek, R. D. Dupuis, and P. D. Dapkus, *J. Appl. Phys.* **50**, 5835 (1979).
- ¹⁵N. Holonyak, Jr., B. A. Vojak, R. M. Kolbas, R. D. Dupuis, and P. D. Dapkus, *Solid State Electron.* **22**, 431 (1979).
- ¹⁶R. D. Dupuis, P. D. Dapkus, C. M. Garner, C. Y. Su, and W. E. Spicer, *Appl. Phys. Lett.* **34**, 335 (1979).
- ¹⁷E. A. Rezek, N. Holonyak, Jr., B. A. Vojak, and H. Shichijo, *J. Appl. Phys.* **49**, 69 (1978).
- ¹⁸R. A. Logan and F. K. Reinhart, *J. Appl. Phys.* **44**, 4172 (1973).
- ¹⁹N. Holonyak, Jr. and D. R. Scifres, *Rev. Sci. Instrum.* **42**, 1855 (1971).
- ²⁰N. Holonyak, Jr., R. M. Kolbas, R. D. Dupuis, and P. D. Dapkus, *Appl. Phys. Lett.* **33**, 73 (1978).
- ²¹N. Holonyak, Jr., R. M. Kolbas, E. A. Rezek, R. Chin, R. D. Dupuis, and P. D. Dapkus, *J. Appl. Phys.* **49**, 5392 (1978).
- ²²H. Shichijo, R. M. Kolbas, N. Holonyak, Jr., R. D. Dupuis, and P. D. Dapkus, *Solid State Commun.* **27**, 1029 (1978).
- ²³A. Shinada and S. Sugano, *J. Phys. Soc. Jp.* **21**, 1936 (1966).
- ²⁴A. M. Kazaryan and E. M. Kazaryan, *Fiz. Tekh. Poluprov.* **11**, 1383 (1977) [*Sov. Phys. Semicond.* **11**, 813 (1977)].
- ²⁵B. A. Vojak, N. Holonyak, Jr., W. D. Laidig, K. Hess, J. J. Coleman, and P. D. Dapkus, *Solid State Commun.* **35**, 477 (1980).
- ²⁶R. Dingle, in *Festkörperprobleme, Advances in Solid State Physics*, Vol. XV, edited by H. J. Queisser (Pergamon/Vieweg, Braunschweig, 1975), pp. 21-48.
- ²⁷J. A. Rossi, N. Holonyak, Jr., P. D. Dapkus, J. B. McNeely, and F. V. Williams, *Appl. Phys. Lett.* **15**, 109 (1969).
- ²⁸N. Holonyak, Jr., B. A. Vojak, W. D. Laidig, K. Hess, J. J. Coleman, and P. D. Dapkus, *Appl. Phys. Lett.* **37**, 136 (1980).
- ²⁹J. Shah, *Solid State Electron.* **31**, 43 (1978).
- ³⁰H. B. Bebb and E. W. Williams, in *Semiconductors and Semimetals* edited by R. K. Willardson and A. C. Beer (Academic Pr., New York, 1972), Vol. 8, pp. 321-392.

Alloy Clustering in $\text{Al}_x\text{Ga}_{1-x}\text{As-GaAs}$ Quantum-Well Heterostructures

N. Holonyak, Jr., W. D. Laidig, and B. A. Vojak

Department of Electrical Engineering and Materials Research Laboratory, University of Illinois at Urbana-Champaign, Urbana, Illinois 61801

and

K. Hess

Department of Electrical Engineering and Coordinated Science Laboratory, University of Illinois at Urbana-Champaign, Urbana, Illinois 61801

and

J. J. Coleman and P. D. Dapkus

Rockwell International, Electronics Research Center, Anaheim, California 92803

and

J. Bardeen

Department of Physics, University of Illinois at Urbana-Champaign, Urbana, Illinois 61801

(Received 28 July 1980)

Data on spontaneous and stimulated emission, in the photon-energy range $E_g + 5\hbar\omega_{LO} \geq \hbar\omega \geq E_g$, are presented on $\text{Al}_x\text{Ga}_{1-x}\text{As-GaAs}$ quantum-well heterostructures with $\text{Al}_x\text{Ga}_{1-x}\text{As}$ ($x \sim 0.4-0.5$) coupling barriers of size $L_B \sim 40-70 \text{ \AA}$ and GaAs wells of size $L_x \sim 30-40 \text{ \AA}$. For $L_x, L_B \leq 50 \text{ \AA}$, Al-Ga disorder (clustering) in the alloy barriers is consistent with the observed spectral broadening and downward energy shift of the confined-particle transitions. A simple substitution of binary (AlAs) for ternary (AlGaAs) barriers eliminates alloy clustering and its effects, and makes unambiguous the identification of clustering in alloy barriers.

PACS numbers: 73.40.Lq, 71.50.+t, 78.45.+h

In contrast to earlier work,^{1,2} stimulated emission has been observed recently at energy $5\hbar\omega_{LO}$ to $6\hbar\omega_{LO}$ below the confined-particle transitions of $\text{Al}_x\text{Ga}_{1-x}\text{As-GaAs}$ multiple-quantum-well heterostructures (QWH) with narrow wells ($L_x \leq 50 \text{ \AA}$) and narrow alloy barriers ($L_B \leq 50 \text{ \AA}$). An example is illustrated in Fig. 1, *a*. The lowest energies are a little above that of the GaAs energy gap, E_g . With increased pump power, stimulated emission is transferred to the neighborhood of the confined-particle states [Fig. 1, *b*]. In this paper, we show that because of disorder and clustering in the narrow ternary barriers (which can be removed by the use of binary barriers, AlAs), a continuum of states may exist in the QWH, the lowest with energies extending down to the band edge of pure GaAs. It is suggested that real phonon transitions take the electrons down to these levels, from which stimulated emission then occurs. With higher power, emission from the confined-particle states is enhanced and electrons do not have time to cascade to the lower levels.

The $\text{Al}_x\text{Ga}_{1-x}\text{As-GaAs}$ quantum-well heterostructures of interest here are grown by metalorganic chemical vapor deposition.^{3,4} Gas flow rates and

layer growth times are electronically controlled to ensure layer reproducibility. Growth rates are controllable in the range 2–50 $\text{\AA}/\text{sec}$ for GaAs and in the range 2.5–100 $\text{\AA}/\text{sec}$ for AlGaAs ($x \sim 0.40$), which makes it practical to grow layers as thin as 10 \AA . The first layer grown on the {100} GaAs substrate is a GaAs buffer layer to provide a good crystallographic surface for succeeding layers. The next layer is a relatively thick ($\sim 1 \mu\text{m}$) $\text{Al}_x\text{Ga}_{1-x}\text{As}$ ($x \sim 0.50$) confining layer. This is followed by the QWH active region, which consists of a series of GaAs quantum wells and $\text{Al}_x\text{Ga}_{1-x}\text{As}$ (or AlAs) barrier layers. The final layer is a second relatively thick ($\sim 0.3 \mu\text{m}$) $\text{Al}_x\text{Ga}_{1-x}\text{As}$ ($x \sim 0.50$) confining layer. All layers are undoped ($n_d - n_a \leq 10^{15}/\text{cm}^3$). Samples for photoluminescence experiments are prepared by polishing and selectively etching off⁵ the GaAs from the substrate side. Cleaved portions ($20-100 \times 100-300 \mu\text{m}^2$) of the remaining thin wafer ($\sim 1.3 \mu\text{m}$ thick) are imbedded for heat sinking into In under a sapphire window (77-K experiments)⁶ or into annealed Cu under a diamond window (300-K experiments),⁷ and are photoexcited with an Ar^+ (5145 \AA) or a dye-tunable (6540- \AA)

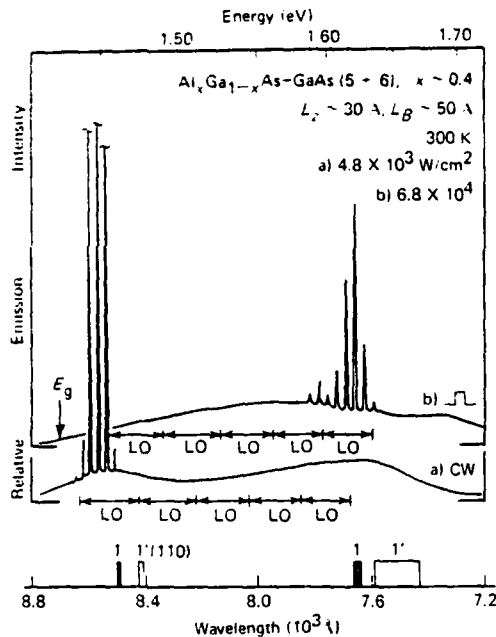


FIG. 1. Laser spectra (300 K) of a photopumped QWH grown by metalorganic chemical vapor deposition with an active region consisting of six ~ 30 Å GaAs wells and five ~ 50 Å $\text{Al}_x\text{Ga}_{1-x}\text{As}$ ($x \sim 0.40$) barriers. The 1 and 1' markers indicate the allowed electron-to-heavy-hole and electron-to-light-hole transitions, respectively, for 30 Å wells separated by perfect 50-Å barriers (i.e., no alloy clustering). The 1 and 1' (110) markers indicate the lowest transitions of a 110-Å well. Typical cw laser operation (a, 4.8×10^3 W/cm²) occurs slightly below the 1 (110) marker, while the spontaneous background extends to higher energy. Pulsed operation of a narrower sample (b, 6.8×10^4 W/cm²) produces lasing at the expected energy of the $n = 1$ transition (30-Å well).

laser.

The 300-K laser data of Fig. 1 demonstrate the range of laser mode energies attainable from a QWH with an active region consisting of six $L_x \sim 30$ Å GaAs quantum wells coupled by five $L_B \sim 50$ Å, $\text{Al}_x\text{Ga}_{1-x}\text{As}$ ($x \sim 0.4$) barrier layers. At 4.8×10^3 W/cm² cw excitation (a), a 39×110 μm² sample exhibits laser operation at $\lambda \sim 8560$ Å, which is in the anomalous range $\sim 5\hbar\omega_{LO}$ lower in energy than the lowest ($n = 1$) confined-carrier electron-to-heavy-hole ($e-hh$) or lowest ($n' = 1'$) electron-to-light-hole ($e-lh$) transitions of ~ 30 Å GaAs quantum wells coupled by ideal (microscopically uniform) ~ 50 Å, $\text{Al}_x\text{Ga}_{1-x}\text{As}$ ($x \sim 0.4$) barriers. By exciting narrower samples at high level, we observe laser emission as high as 1.63

eV ($\lambda \sim 7600$ Å) as is shown by the 23×94 μm² sample of curve b (6.8×10^4 W/cm², pulsed). This high emission energy, which is expected ($L_x \sim 30$ Å), serves to identify the lowest confined-carrier transitions ($n = 1, n' = 1'$) of an ideal structure.

Alloy clustering in the $\text{Al}_x\text{Ga}_{1-x}\text{As}$ barrier layers, which is a form of disorder and is inevitable, allows further interpretation of these spectra. In the extreme case of very large scale clustering, which would allow GaAs to extend across a barrier (~ 50 Å) and connect two or even more wells, the carrier recombination can approach $E_g(\text{GaAs})$ or $\lambda \sim 8707$ Å (300 K). Even for a smaller average cluster size it is possible that regions exist in the $\text{Al}_x\text{Ga}_{1-x}\text{As}$ barriers where the Al concentration is nearly zero. The resulting local potential-well size is effectively increased from $L_x \sim 30$ Å to as much as $L_x + L_B + L_x \sim 110$ Å. The location (energy) of the lowest confined-carrier transitions of a ~ 110 -Å GaAs quantum well are also labeled in Fig. 1. Note that alloy clustering in the barrier layers sufficient to create GaAs paths through the $\text{Al}_x\text{Ga}_{1-x}\text{As}$ barriers is expected to have a drastic effect in broadening and lowering the energy spectrum of this quantum system. For example, the $n = 1$ confined-electron state shifts downward by ~ 140 meV for a size shift from $L_x \sim 30$ Å to $L_x + L_B + L_x \sim 110$ Å.

A result of this shift is that the density of states of a QWH with alloy clustering in the barriers will not exhibit an abrupt step to zero at energies below the lowest confined-particle states of an ideal structure. Instead, the density of states is expected to be small but significant below these "lowest" confined-carrier states, and then drop to zero for energies less than $E_g(\text{GaAs})$. Besides depending upon the barrier size L_B , the exact form of the density of states will depend on the average cluster size, the form of the cluster size distribution, and on the composition x of the $\text{Al}_x\text{Ga}_{1-x}\text{As}$. Also, cluster-induced quantization in the x, y dimensions will play a role.

These additional lower-energy states are expected to play an important part in radiative emission from a QWH. The existence of small areas or patches within the active region with lower-energy states (areas that increase in number with the number of barriers) increases the probability of LO-phonon-assisted recombination processes⁸ at energies $E_{1,1'} > \hbar\omega > E_g$ since virtual transitions are no longer required. Instead, real transitions in this range at multiples of $\sim \hbar\omega_{LO}$ below the $n = 1$ and $n' = 1'$ transitions of the $L_x \sim 30$ Å well are possible.

Further evidence for alloy clustering in the $\text{Al}_x\text{Ga}_{1-x}\text{As}$ barriers is shown (Fig. 2) by the form of the high-level spontaneous emission spectra of a two-well, one-barrier ($x \sim 0.5$) QWH (a different QWH wafer) with all three layers ~ 40 Å thick. Note that in this case the barrier size is smaller (40 Å) and approaches and helps identify the average cluster size. As in Fig. 1, the confined-carrier transitions of the ideal $L_z \sim 40$ Å quantum well and also of the larger $L_z + L_B + L_z \sim 120$ Å composite quantum well are labeled in Fig. 2. The two samples (a, $4 \times 10^4 \text{ W/cm}^2$, $90 \times 360 \mu\text{m}^2$; b, 10^5 W/cm^2 , $56 \times 195 \mu\text{m}^2$) exhibit very similar spectra as, in fact, do all of the samples from this wafer. A large peak in the range of $n' = 1'$ is observed. The emission does not drop to zero just below the $n = 1$ $e-hh$ transition, as would be expected in the ideal cluster-free limit, but extends downward in energy to nearly the location of the $n = 1$ (120) and $n' = 1'$ (120) transitions, which are near a distinct shoulder in the emission. An increase in the barrier thickness to ~ 70 Å results in cutoff of most of this lower energy emission.⁹ As the barrier thickness L_B is decreased from ~ 70 Å (Ref. 9) to ~ 50 Å (Fig. 1) to ~ 40 Å (Fig. 2) and approaches the average cluster size, tunneling filaments are likely to appear in the $\text{Al}_x\text{Ga}_{1-x}\text{As}$ barriers, which results in a major increase of the effective

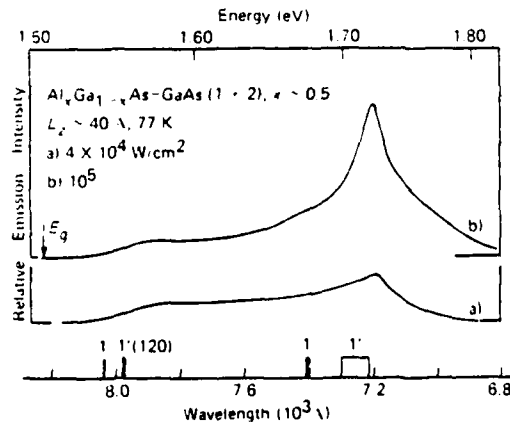


FIG. 2. Photoemission (77 K) of two QWH samples with active regions consisting of two 40-Å GaAs wells separated by one 40-Å $\text{Al}_x\text{Ga}_{1-x}\text{As}$ ($x \sim 0.50$) barrier. These spectra (a, $4 \times 10^4 \text{ W/cm}^2$; b, 10^5 W/cm^2) exhibit a peak near the $n' = 1'$ transition of a 40-Å well, with emission extending to lower energy. Note that this emission rolls off near the lowest-energy transitions of a composite-layer 120-Å well, indicated by the 1 and 1' (120) markers.

well dimension from $\sim L_z$ to $\sim L_z - L_B + L_z$. The observation of spectra such as those of Fig. 2 allow an estimate to be made of the cluster size (≈ 40 Å).

Further 300-K laser data on a 29-barrier, 30-well $L_z \sim 30$ Å, $L_B \sim 50$ Å superlattice structure (not shown) demonstrate that laser operation below E_g is also attainable. This fact, along with recent laser data on QWH's consisting of a large quantum well (or in some cases a bulk layer) coupled to a phonon-generating and -reflecting array of smaller quantum wells,⁹ indicate that *virtual* phonon-assisted recombination processes with $\hbar\omega < E_g$ can occur and are not inconsistent with the present data. Alloy clustering (*in ternary barriers*), however, allows actual states to exist between the bulk band edge and the lowest quantum states characteristic of an ideal QWH and thus permits *real* phonon processes to scatter the electrons to lower energies before recombining.

It is worth mentioning that a reinterpretation of previous investigations of disorder scattering¹⁰⁻¹³ indicates that cluster models might have to be involved to explain successfully the experimental results for electron mobilities in III-V alloys. For example, negligible alloy scattering seems to exist¹² in $\text{In}_{1-x}\text{Ga}_x\text{As}$ and strong alloy scattering in the quaternary system $\text{In}_{1-x}\text{Ga}_x\text{P}_{1-x}\text{As}_x$,¹³ which (for the latter) cannot be explained on the basis of random-compositional-disorder models alone. In addition, these models do not take into account, in detail, the peculiarities of crystals such as $\text{Al}_x\text{Ga}_{1-x}\text{As}$ or $\text{GaAs}_{1-x}\text{P}_x$ that undergo a direct-indirect transition in the range $x \approx x_c = 0.4-0.5$, nor whether such crystals are particularly prone to clustering. It is also worth mentioning that data are not presently available indicating how sensitive cluster formation is to the specific process (vapor-phase epitaxy, liquid-phase epitaxy, molecular-beam epitaxy) used to grow a III-V alloy.

In any case, the basic features of the $\text{Al}_x\text{Ga}_{1-x}\text{As}$ alloy clustering described above are clear since, besides the data of Figs. 1 and 2, simple substitution of binary barriers (including very narrow barriers, ~ 10 Å) for the ternary barriers employed here eliminates recombination below the expected (ideal) confined-particle transitions of a QWH. These further data are shown in Fig. 3, which is for the case of a QWH with twelve GaAs wells ($L_z \sim 50$ Å) interleaved in the active region with thirteen *binary* (nonclustered) AlAs barriers ($L_B \sim 10$ Å). The laser operation of the sample ($50 \times 90 \mu\text{m}^2$) occurs exactly on the $n = 1$,

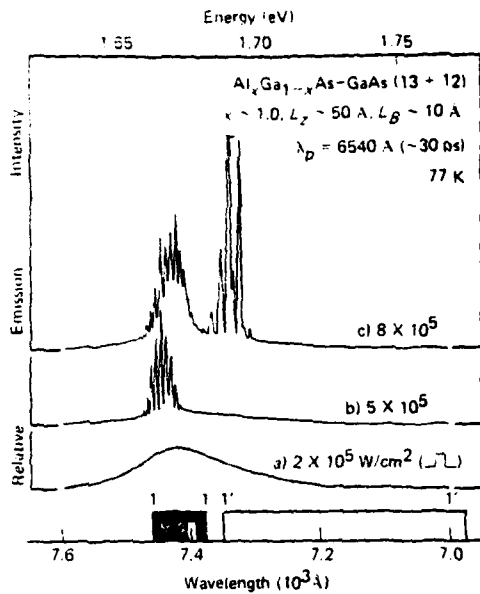


FIG. 3. Photoluminescence (laser) spectra (77 K) of a QWH sample with an all-binary (cluster-free) active region consisting of twelve $\sim 50\text{-\AA}$ GaAs wells alternating with thirteen $\sim 10\text{-\AA}$ AlAs barriers. The excitation power densities are high ($\sim 10^5$ W/cm 2) since absorption of the incident pump beam ($\lambda_p \sim 6540$ Å) occurs only at the 50-\AA GaAs wells. Spontaneous (a) and stimulated (b, c) emission occur only on the $n = 1$ and $n' = 1'$ transitions, and not at lower energy as in Figs. 1 and 2.

$e-hh$ and $n' = 1'$, $e-lh$ "bands" with no recombination radiation between $E_2(\lambda \sim 8224$ Å) and $E_1(\lambda \sim 7460$ Å), and with only minor spectral broadening just below E_1 , as would occur for small growth fluctuations in layer size.

Finally we emphasize that the consequences of alloy clustering are very different for QWH layers and for bulk semiconductors. In a bulk III-V alloy the changes in the scattering rates (e.g., decrease in carrier mobility) due to clusters are quite small,¹⁰ whereas in layered structures size-quantization effects can be totally destroyed. It is exactly these effects of size quantization that are probed with QWH laser emission, which is therefore a sensitive new tool to investigate clustering.

The authors are grateful to Yuri S. Moroz, R. T. Gladin, B. L. Marshall, and B. L. Payne (Urbana) for technical assistance, and to G. E. Stillman for various discussions. This work has been supported by the National Science Foundation under Grants No. DMR-79-09991 and No. DMR-77-23999 and by U. S. Navy Contract No. N00014-79-C-0768; the work has also been partially supported by the U. S. Office of Naval Research under Contract No. N00014-78-C-0711.

¹N. Holonyak, Jr., R. M. Kolbas, R. D. Dupuis, and P. D. Dapkus, IEEE J. Quantum Electron. **QE-16**, 170 (1980).

²N. Holonyak, Jr., R. M. Kolbas, W. D. Laidig, B. A. Vojak, K. Hess, R. D. Dupuis, and P. D. Dapkus, J. Appl. Phys. **51**, 1328 (1980).

³H. M. Manasevit, J. Electrochem. Soc. **118**, 647 (1971).

⁴R. D. Dupuis and P. D. Dapkus, in *Proceedings of the Seventh International Symposium on GaAs and Related Compounds*, St. Louis, 1978, edited by C. M. Wolfe (Institute of Physics, Bristol, 1979), pp. 1-9.

⁵R. A. Logan and F. K. Reinhart, J. Appl. Phys. **44**, 4172 (1973).

⁶N. Holonyak, Jr., and D. R. Scifres, Rev. Sci. Instrum. **42**, 1885 (1971).

⁷N. Holonyak, Jr., R. M. Kolbas, R. D. Dupuis, and P. D. Dapkus, Appl. Phys. Lett. **33**, 73 (1978).

⁸J. J. Coleman, P. D. Dapkus, B. A. Vojak, W. D. Laidig, N. Holonyak, Jr., and K. Hess, Appl. Phys. Lett. **37**, 15 (1980).

⁹R. D. Dupuis, P. D. Dapkus, N. Holonyak, Jr., R. M. Kolbas, W. D. Laidig, and B. A. Vojak, Pis'ma Zh. Tekh. Fiz. **5**, 132 (1979) [Sov. Tech. Phys. Lett. **5**, 52 (1979)].

¹⁰J. W. Harrison and J. R. Hauser, Phys. Rev. B **13**, 5347 (1976).

¹¹M. A. Littlejohn, J. R. Hauser, T. H. Glisson, D. K. Ferry, and J. W. Harrison, Solid State Electron. **21**, 107 (1978).

¹²T. P. Pearsall, R. Bisaro, P. Merenda, G. Lauren- cin, R. Ansel, J. C. Portal, C. Houlbert, and M. Quil- lec, in *Proceedings of the Seventh International Sym- posium on GaAs and Related Compounds*, St. Louis, 1978, edited by C. M. Wolfe (Institute of Physics, Bristol, 1979), pp. 94-102.

¹³P. D. Greene, S. A. Wheeler, A. R. Adams, A. N. El-Sabbahy, and C. N. Ahmad, Appl. Phys. Lett. **35**, 78 (1979).

THE EXCITON IN RECOMBINATION IN $Al_xGa_{1-x}As$ -GaAs QUANTUM-WELL HETEROSTRUCTURES

B.A. Vojak, N. Holonyak, Jr, and W.D. Laidig

Department of Electrical Engineering and Materials Research Laboratory,
 University of Illinois at Urbana-Champaign, Urbana, IL 61801

K. Hess

Department Of Electrical Engineering and Coordinated Science Laboratory,
 University of Illinois at Urbana-Champaign, Urbana, IL 61801

J.J. Coleman and P.D. Dapkus

Rockwell International, Electronics Research Center,
 Anaheim, California 92803

(Received 15 May 1980 by A.A. Maradudin)

Low temperature (4.2-77 K) photoluminescence and laser data on metal-organic chemical vapor deposited $Al_xGa_{1-x}As$ -GaAs quantum-well heterostructures are presented that exhibit emission peaks between the lowest energy confined-carrier transitions and their phonon sidebands. These data indicate the involvement of the two-dimensional exciton in recombination in quantum-well heterostructures.

Although confined-carrier as well as phonon-assisted recombination transitions have been identified in the emission spectra of quantum-well heterostructure (QWH) lasers,¹⁻⁴ a number of unexplained emission peaks still remain. While the phonon-sideband laser operation occurs $\hbar\omega_{LO}$ -36 or even 2×36 meV lower in energy than the lowest ($n=1$) confined-particle transitions ($\Delta n=0$),⁵ other spontaneous and stimulated peaks have been observed in the range (≈ 20 meV) between the phonon peaks and the lowest confined-carrier transitions. In the present work low temperature (4.2-77 K) photoluminescence and laser data on thin (1.3-1.5 μm) rectangular samples of MO-CVD $Al_xGa_{1-x}As$ -GaAs quantum-well heterostructures indicate the involvement in recombination, probably with phonon enhancement, of the two-dimensional exciton.

Emission spectra on two different MO-CVD $Al_xGa_{1-x}As$ -GaAs QWH wafers are presented. Both wafers are grown on (100) GaAs substrates as described elsewhere.^{6,7} The first structure consists of a 1 μm $Al_xGa_{1-x}As$ ($x=0.42$, $n_d \approx 10^{18} cm^{-3}$) confining layer, an undoped ($n_d \approx n_a \approx 10^{15} cm^{-3}$) active region consisting of 6 $L_z \approx 120 \text{ \AA}$ thick GaAs layers coupled by 5 $\times 120 \text{ \AA}$ $Al_xGa_{1-x}As$ ($x=0.27$) layers, and a second 0.5 μm $Al_xGa_{1-x}As$ ($x=0.42$, $n_d \approx 10^{18} cm^{-3}$) confining layer. The second wafer contains a 1 μm thick $Al_xGa_{1-x}As$ ($x=0.36$) confining layer, 7 $L_z \approx 50 \text{ \AA}$ GaAs layers and one $L_z \approx 200 \text{ \AA}$ GaAs layer with all of the GaAs quantum wells coupled by 50 \AA thick $Al_xGa_{1-x}As$ ($x=0.37$) barriers, and finally a second 0.3 μm thick $Al_xGa_{1-x}As$ ($x=0.36$) confining layer. The second wafer is undoped ($n_d \approx n_a \approx 10^{15} cm^{-3}$). The substrate GaAs of each wafer is removed, and the remaining thin wafer is cleaved into small rectangles (20-50 $\mu m \times 100$ -200 μm) that are then imbedded into In under a sapphire window for heat sinking.

An example of low temperature (4.2 K) QWH

emission in the range $E_n' = 1' - \hbar\omega_{LO} \leq \hbar\nu \leq E_{n'} = 1'$ is shown in Fig.1, which is for the case of the δ -well, 5-barrier $L_z \approx 120 \text{ \AA}$ wafer. At a CW photoexcitation (Ar^+ , $\lambda \approx 5145 \text{ \AA}$) level of $100 W/cm^2$, curve a, an emission peak at $\lambda \approx 8085 \text{ \AA}$ with a shoulder B at higher energy is observed. As the pump power is increased to $600 W/cm^2$, curve b, laser operation occurs on a phonon sideband of the $n'=1'$ transition ($1'-LO$), i.e., below peaks A and B, with the spontaneous background remaining peaked at both $\lambda \approx 8085 \text{ \AA}$ and $\lambda \approx 8020 \text{ \AA}$. With further increase in excitation level (c, $6.6 \times 10^3 W/cm^2$, pulsed excitation), the spontaneous emission spectrum exhibits a noticeable bump or replica at longer wavelength in the region $E_A - \hbar\omega_{LO}$ ($A-LO$) and $E_B - \hbar\omega_{LO}$ ($B-LO$).

The two arrows A and B in Fig.1 are located 20 meV and 13 meV lower in energy than the $n=1$ electron-to-heavy hole ($e-hh, n$) and $n'=1'$ electron-to-light hole ($e-lh, n'$) transitions, respectively. The positions of the $n=1$ and $n'=1'$ transitions have been determined by calculations based on measured layer thicknesses, which agree with the MO-CVD growth calibration, and by narrow-sample photoluminescence data that distinctly exhibit laser operation on the confined-particle transitions. (As examples, see Fig.6 of Ref.8 and curve c in Fig.3 of Ref.9.) The 20 meV (A) and 13 meV (B) downshifts are the expected two-dimensional free-exciton binding energies for electron-heavy hole and electron-light hole excitons, respectively. The two-dimensional binding energy of the exciton is 4x larger than for the three dimensional case,^{10,11} so that

$$E_{Ex2D} = 4(13.6/e^2)(\mu/m_0) \text{ meV.} \quad (1)$$

where $1/\mu = (1/m_e^*) + (1/m_h^*)$.

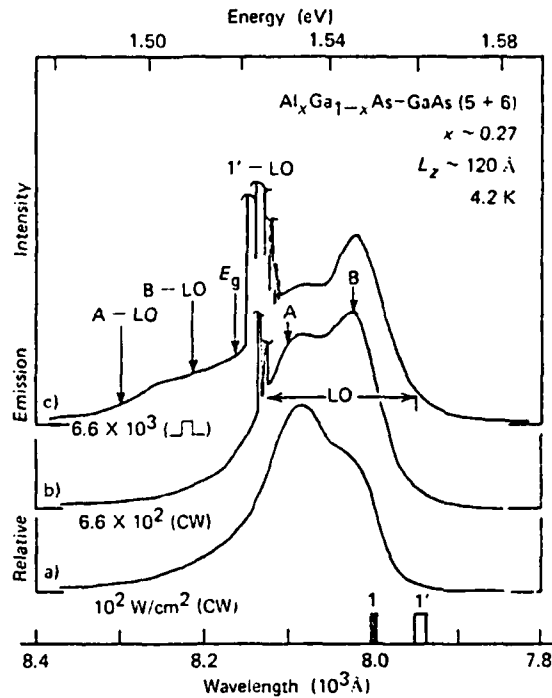


Fig.1 Photoluminescence spectra (4.2 K) of an Al_xGa_{1-x}As-GaAs multiple-quantum-well heterostructure grown by metalorganic chemical vapor deposition. The active region, sandwiched between two Al_xGa_{1-x}As (*x*~0.42) confining layers, consists of six 120 Å GaAs wells separated by five 120 Å Al_xGa_{1-x}As (*x*~0.27) barriers. Low-level CW emission (10^2 W/cm², curve a) occurs primarily at energies below those of the lowest confined-particle transitions indicated on the horizontal axis by the heavy (*n*=1, *e*+*hh*) and light (*n*'=1', *e*+*lh*) markers. At slightly higher CW excitation (6.6×10^2 W/cm², curve b) stimulated emission occurs at $\hbar\omega_{LO}$ -phonon energy ($\hbar\omega_{LO} = 36$ meV) below the *n*'=1' *e*+*lh* transition, as indicated by the LO label. With pulsed excitation (6.6×10^3 W/cm², curve c) the emission spectrum from the same sample shows structure at still lower energy. The arrows marked A and B designate energies 20 meV below the *n*=1 *e*+*hh* transition energy and 11 meV below the *n*'=1' *e*+*lh* transition energy, respectively. Similarly, the arrows marked A-LO and B-LO correspond to energies 36 meV below those designated by the A and B arrows.

Values of the parameters used are: $m_e^* = 0.45 m_0$,¹² $m_{lh}^* = 0.087 m_0$,¹³ $m_e^* = 0.0665 m_0$,¹⁴ and for the relative static dielectric constant $\epsilon = 12.6$.¹⁵ The location of the two emission peaks A and B are in very close agreement with the calculated two-dimensional exciton energies. Note that two separate exciton peaks are expected in this case since at $k_x = k_y = 0$ ($k_z = \pi/L_z$ for $n=1$) the light- and heavy-hole valence bands are not degenerate as they are at $k=0$ in the bulk limit. That the light-hole exciton location is in better agreement with the estimate than that of the heavy hole could be due to the difference in the extent of their two-dimensionality. An electron-heavy hole exciton has a bulk Bohr radius of $\sim 120 \text{ \AA}$ while the electron-light hole exciton has a bulk Bohr radius of $\sim 170 \text{ \AA}$. The light-hole exciton is thus expected to be closer to the two-dimensional limit than the heavy-hole exciton. The low energy shoulder observed on

curve c of Fig.1 (between arrows A-LO and B-LO) is in the range $\hbar\omega_{LO}$ below the A and B emission peaks and could be a phonon sideband of the exciton emission since it appears only at higher excitation level when the phonon density is expected to be quite high.

Emission spectra from the second wafer, which is designed with a 7-well phonon-generating array (7 $L_{z2} \sim 50 \text{ \AA}$ GaAs wells) coupled to a single large well ($L_{z1} \sim 200 \text{ \AA}$),⁹ are shown in Figs.2 and 3. At low excitation level (Fig.2a, 10 W/cm^2), a spontaneous peak is observed $\sim \hbar\omega_{LO}$ below the $n'=1'$ transitions of the 50 \AA wells,⁹ which are degenerate with the $n'-3'$ transition of the 200 \AA well. Another peak, the main peak, occurs at $\lambda \sim 8280 \text{ \AA}$ with a shoulder at $\lambda \sim 8260 \text{ \AA}$ that previously has not been identified. Upon increased excitation of the sample, curve b, laser operation occurs

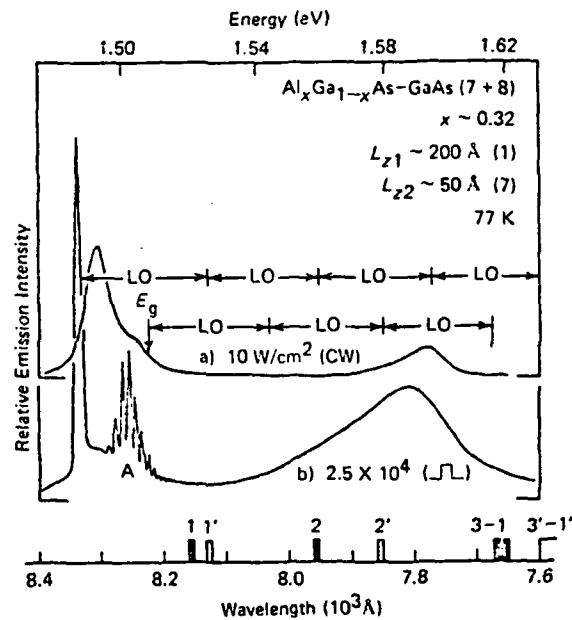


Fig.2 Comparison of CW (10 W/cm^2) and pulsed ($2.5 \times 10^4 \text{ W/cm}^2$) emission spectra (77 K) of a photopumped multiple-quantum-well heterostructure with an active region composed of one 200 \AA and seven 50 \AA GaAs wells coupled by seven 50 \AA Al_xGa_{1-x}As ($x=0.32$) barriers. Note the shoulder (curve a) near the A arrow, which is located 20 meV below the lowest confined-particle transition ($n=1$, $e+hh$) of the 200 \AA well. Pulsed excitation of the same sample (curve b) results in narrowly spaced end-to-end laser modes (not resolved in this curve) in LO phonon energy below the $n'=1'$ $e+2h$ transition, and widely spaced edge-to-edge modes at approximately the same energy as the shoulder (and the A arrow) observed on curve a.

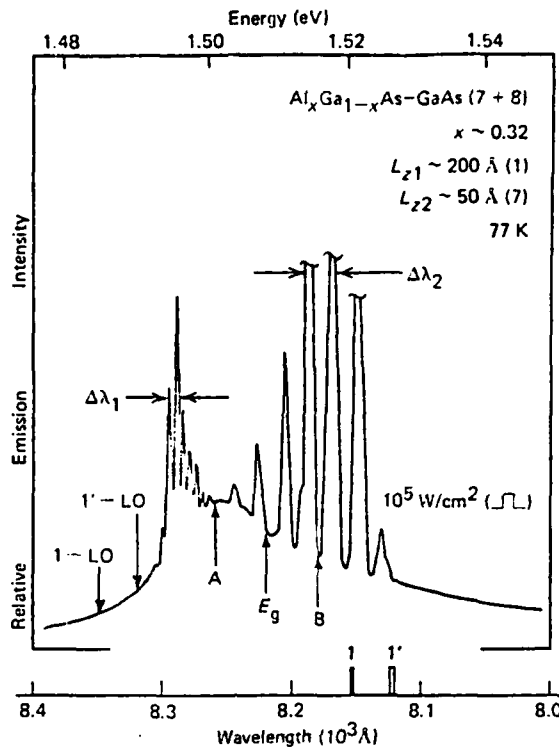


Fig.3 Stimulated emission (77 K) of a sample obtained from the same wafer described in Fig.2. The relatively high-level pulsed excitation (10^5 W/cm^2) produces emission in the energy range between the lowest confined-particle transitions ($n=1$ and $n'=1'$) and an LO phonon energy below these transitions, allowing observation of two distinct sets of modes. The narrowly spaced end-to-end modes labeled by $\Delta\lambda_1$ (corresponding to the sample length, $160 \mu\text{m}$) occur at energies in a region of very low absorption. For emission at energies higher than 20 meV below the $n=1$ e-hh transition (A arrow), absorption is stronger in the region of the two-dimensional exciton, resulting in the widely spaced edge-to-edge laser modes labeled by $\Delta\lambda_2$ (corresponding to the sample width, $46 \mu\text{m}$).

on a phonon sideband of the $n'=1'$ transition of the 200 \AA quantum well⁹ and also $\sim 20 \text{ meV}$ below the $n=1$ transition (modes A). Although the mode detail is not resolved in the figure, the phonon sideband ($1'-\text{LO}$, largest peak) lases in the lengthwise cavity (narrowly-spaced modes), while the laser operation at A occurs in the edge-to-edge direction of the rectangular sample. This difference in cavity oscillation for a rectangular sample, excited fully across its width but not entirely along its length, is consistent with

$\alpha(E_A) > \alpha(E_{n'=1'} - \hbar\omega_{\text{LO}})$. Since the stimulated emission on peak A occurs at $E_A < E_g$, the origin of this emission cannot be confused with confined-carrier transitions, which are all above E_g and have been positively identified in other work.⁹

At very high excitation levels, excitons are not expected to exist in simple form. At large power densities, phonon effects are expected to be large, and emission below the confined-particle transitions is due mainly to phonon-shifted recombination from the lowest energy portions of

the $n=1$ subband of the 200 Å well.⁹ This does not mean that exciton absorption in the unpumped regions of the sample can have no effect on laser operation. For example, Fig. 3 shows the high level laser operation of a rectangular sample from the same wafer as that of Fig. 2 (similar excitation). A continuous set of laser modes is observed in the 36 meV range from the $n=1$ transition of the 200 Å well down to the phonon-sideband of the $n=1$ transition. Note, however, that the cavity oscillations switch rather abruptly from narrowly spaced modes ($\Delta\lambda_1$) to widely spaced modes ($\Delta\lambda_2$) at an energy slightly higher than but very near λ (i.e., 20 meV below the $n=1$ confined-carrier transition). The closely spaced modes $\Delta\lambda_1$ identify laser oscillations along the length of the sample while the broader spaced modes $\Delta\lambda_2$ are due to oscillations across the width. This switch in the cavity oscillations is an indication of a step in the absorption of the unexcited portion of the sample.

The type of mode behavior shown in Fig. 3 in the range 20 meV below the lowest confined-carrier transition ($n=1$) has been observed also on samples from other QWH wafers. With slight modification of the pumping beam geometry relative to the sample, particularly for a single 200 Å GaAs well,^{1,2} this behavior can be observed to extend up to the $n=1$ confined-carrier transition, presumably due to less absorption on the exciton compared to the first subband. For the samples of the present work (Figs. 2 and 3), it should be noted that the phonon generation in the 7-well array is very efficient,⁹ more so than for a single 200 Å GaAs quantum well. Thus resonant enhancement involving LO phonons should be quite significant in the range between the two-

dimensional exciton and the first confined-carrier subband of the auxiliary 200 Å GaAs well, which is closely coupled to the phonon-generating array.

Two more items are worth mentioning: The " E_g " labels in Fig. 1-3 are merely references. We know from other work that by simply reducing the GaAs well size the recombination at E_g can be cut-off but not the -20 meV band of recombination radiation located just below the lowest confined-particle transitions. The second is that for a variety of reasons the exciton band below the lowest recombination transitions ($1, 1'$) is not expected to be as narrow or as sharp as for the bulk crystal case. Various scattering and relaxation processes over a considerable energy range play a role, as well as poorly understood high-density particle interactions. In addition, the particle distribution across the GaAs well is not uniform nor the effect of the confining layers, and thus the degree of two-dimensional shift in exciton binding energy. Also, if coupled wells are employed, they are not expected to be totally identical. Nor are the wells (single or multiple) necessarily entirely planar. Finally, it is worth mentioning that the narrowest QWH recombination lines are observed on phonon sidebands ($E_1 - \hbar\omega_{LO}$ or $E_{1'} - \hbar\omega_{LO}$) of the lowest confined-particle transitions.

The authors wish to thank Yuri S. Moroz, R.T. Gladin, B.L. Marshall, and B.L. Payne (Urbara) for technical assistance, and G.E. Stillman for various discussions. The work of the Illinois group has been supported by NSF Grants DMR 79-09991 and DMR 77-23999, and Navy Contract N00014-79-C-0766; the work of the Rockwell group has been partially supported by the Office of Naval Research, Contract N00014-14-78-C-0711.

REFERENCES

1. KOLBAS, R.M., HOLONIYAK, N., JR., DUPUIS, R.D., and DAPKUS, P.D., Pis'ma v Zh. Tekh. Fiz. 1, 69 (1978) Sov. Tech. Phys. Lett. 4, 28 (1978).
2. HOLONIYAK, N., JR., KOLBAS, R.M., DUPUIS, R.D., and DAPKUS, P.D., IEEE J. Quantum Electron. QE-16, 170 (1980).
3. HOLONIYAK, N., JR., KOLBAS, R.M., LAIDIG, W.D., ALTERELLI, M., DUPUIS, R.D., and DAPKUS, P.D., Appl. Phys. Lett. 34, 502 (1979).
4. HOLONIYAK, N., JR., KOLBAS, R.M., LAIDIG, W.D., VOJAK, B.A., HESS, K., DUPUIS, R.D., and DAPKUS, P.D., J. Appl. Phys. 51, 1328 (1980).
5. SHIK, A. YA., Pis'ma Zh. Tekh. Fiz. 5, 869 (1979) Sov. Tech. Phys. Lett. 2, 358 (1979).
6. MANASEVIT, H.M., J. Electrochem. Soc. 118, 647 (1971).
7. DUPUIS, R.D. and DAPKUS, P.D., 7th Intl. Symp. on GaAs and Related Compounds, St. Louis, 1978, ed. C.M. Wolfe (Institute of Physics, London, 1979), pp. 1-9.
8. VOJAK, B.A., HOLONIYAK, N., JR., CHIN, R., REZEK, E.A., DUPUIS, R.D., and DAPKUS, P.D., J. Appl. Phys. 50, 5835 (1979).
9. COLEMAN, J.J., DAPKUS, P.D., VOJAK, B.A., LAIDIG, W.D., HOLONIYAK, N., JR., and HESS, K., Appl. Phys. Lett. 36, to be published (15 June 1980).
10. SHINADA, M. and SUGAWA, S., J. Phys. Soc. Japan 21, 1936 (1956).
11. KAZARYAN, A.M. and KAZARYAN, E.M., Fiz. Tekh. Poluprov. 11, 1383 (1977) Sov. Phys.-Semicond. 11, 813 (1977).
12. VREHEN, Q.H.F., J. Phys. Chem. Solids 29, 129 (1968).
13. MEARS, A.L. and STRADLING, R.A., J. Phys. C. 4, L22 (1971).
14. STILLMAN, G.E., WOLFE, C.M. and DIRMACK, J.O., Solid State Commun. 7, 921 (1969).
15. STILLMAN, G.E., LARSON, D.M., WOLFE, C.M. and BRANDT, R.C., Solid State Commun. 9, 2245 (1971).

13

TEMPERATURE DEPENDENCE OF THRESHOLD CURRENT FOR A QUANTUM-WELL HETEROSTRUCTURE LASER

K. HESS, B. A. VOJAK, N. HOLONYAK, Jr. and R. CHIN

Department of Electrical Engineering, University of Illinois, Urbana-Champaign, Urbana, IL 61801, U.S.A.

and

P. D. DAPKUS

Rockwell International, Electronic Devices Division, Electronics Research Center, Anaheim, CA 92803, U.S.A.

(Received 1 October 1979; in revised form 5 December 1979)

Abstract—The threshold current density, J_{th} , of a quantum-well laser diode is calculated taking into account the quasi-two-dimensional nature of the heterostructure. The calculated value of $J_{th}(T)$ for a quantum-well laser diode is found, in agreement with experiment, to be less temperature sensitive than that of a conventional double heterojunction laser. The step-like densities of states and the perturbed (hot) carrier distribution of a quasi-two-dimensional structure are responsible for the weaker temperature dependence. Supporting data on quantum-well $Al_xGa_{1-x}As$ -GaAs heterostructure laser diodes grown by MO-CVD are presented showing that in the conventional expression $J_{th}(T) = J_{th}(0) \exp(T/T_0)$, T_0 can be as high as $\sim 437^\circ C$.

INTRODUCTION

Although the study of quantum size effects (QSE) in solids [1], including semiconductors [2], is not particularly a new area of investigation, quantum-well laser diodes (which exhibit QSE) have existed only since 1977 [3]. Two kinds of quantum-well heterostructure laser diodes have been constructed, the first in the InP - $In_{1-x}Ga_xP_{1-x}As$, [3, 4] system and the second in the more highly developed $Al_xGa_{1-x}As$ -GaAs system [5-7]. In the case of the latter, continuous room temperature (CW, $300^\circ K$) laser operation has been achieved in both single [6] and multiple-quantum-well heterostructures [7], which, with promising reliability data [8], indicates that this form of laser diode is practical and more than a curiosity.

The quasi-two-dimensional nature of quantum-well heterostructures introduces several unique features to semiconductor laser operation: A step-like density of states replaces the usual bulk-crystal parabolic density of states, and phonon participation in recombination, which is not important below the bulk-crystal band edge, plays an observable role in quantum-well lasers [9, 10]. Among other effects, the step-like density of states of a quantum-well heterostructure changes the basic form of the current threshold for laser operation. Experimental data show that the current threshold, $J_{th}(T)$, of a quantum-well laser diode is less temperature sensitive than that of the typical double heterojunction [7, 11]. In this paper the step-like density of states of a quasi-two-dimensional heterostructure is shown to be the basis of this improved temperature behaviour.

The temperature dependence of the threshold current density is sensitive to both the form of the density of states and the carrier (electron and hole) distribution functions. Previous analyses of $J_{th}(T)$ have employed a parabolic density of states [12] to model a bulk semiconductor while band tail effects have been incorporated in the form of a Gaussian [13] or exponential [14] distribution. Fermi-Dirac

carrier distributions have been used in previous analyses. The use of a quasi-two-dimensional active region in a laser diode produces fundamental changes in this model. Below expressions for the temperature dependence of J_{th} for a quantum-well-heterostructure are determined assuming a constant density of states in the limits of strong and weak electron-electron interactions. Experimental evidence for the weak dependence of J_{th} on temperature is presented for single-quantum-well heterostructure diodes with GaAs regions of thickness $L_z \sim 200 \text{ \AA}$.

MODEL

The electronic energy spectrum of a confined carrier in a thin GaAs layer sandwiched between AlGaAs confining layers has been shown by absorption measurements [15] to correspond to that expected of a one dimensional finite square potential well defined by the GaAs and AlGaAs band edges. Additionally, and of more importance to this work, radiative recombination from the lowest confined-particle transitions of a quantum-well heterostructure can be moved up in energy as high as $\sim 150 \text{ meV}$ above $\hbar\omega \sim E_g(L_z \sim 50 \text{ \AA})$, which agrees with calculations [16]. The parabolic energy-band dispersion in the x - y plane normal to the direction of quantization results in a constant density of states

$$g_{c,v} = m_{c,v}^* / (\pi \hbar^2 L_z) \quad (1)$$

for each subband. As shown in Fig. 1, the first step in the density of states begins at the lowest confined-electron state and is followed by another subband (step) with a constant (upward, $E \uparrow$) block of states, etc. This behaviour also applies to heavy holes and to light holes ($E \downarrow$) as is clear from the lower part of Fig. 1.

The energy distribution of electrons in the quantum well during laser operation is difficult to calculate. Electrons (and holes) cascade down (up) the quantum well by phonon emission and thermalize by electron-

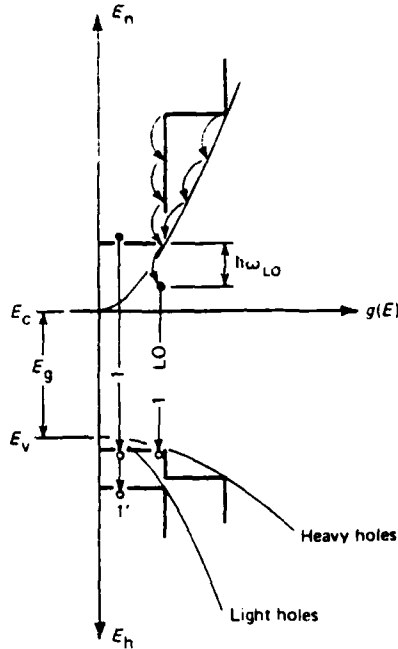


Fig. 1. Density of states diagram for electrons, E_n , and holes, E_h , for an $\text{Al}_x\text{Ga}_{1-x}\text{As-GaAs}$ quantum-well heterostructure. The half-parabolas that originate from the conduction band edge E_c and valence band edge E_v correspond to the densities of state of bulk crystal (thickness $L_z \approx 500 \text{ \AA}$). The step-like densities of states are characteristic of a two-dimensional or quantum-well structure (e.g. $L_z \approx 200 \text{ \AA}$). Also shown is the downward scattering of electrons via LO phonon emission (curved arrows, energy increments $\hbar\omega_{\text{LO}}$) in a quantum-well heterostructure and in a bulk semiconductor.

electron interactions. In the limit of strong electron-electron interaction a Fermi-Dirac distribution is established:

$$f_c(\epsilon) = 1 / \{1 + \exp(\epsilon - F_c)\}, \quad (2)$$

where ϵ and F_c , the electron quasi-Fermi level, are normalized to kT_c . T_c is the electron temperature, which is always higher than the temperature of the crystal lattice. A method to calculate T_c has been described by Shah [17]. Applied to the quantum-well case, this method gives $T_c \approx 300 \text{ K}$ also for rather low lattice temperatures.

Next, in the limit of weak electron-electron interaction, a distribution function composed of "spikes" spaced $\hbar\omega_{\text{LO}} \sim 36 \text{ meV}$ apart is expected because of the strong polar optical phonon scattering. (This can be easily seen from the Boltzmann equation if only scattering by optical phonons is important.) These spikes should occur at the locations of the arrow heads shown in Fig. 1. The curved arrows represent the process of electrons cascading downward by emission of LO phonons. Modeling these spikes as delta functions results in the following form for the distribution function

$$f_c(\epsilon) = \sum_{m=0}^{\infty} C_m \delta(\epsilon - [\Delta E_c - m\hbar\omega_{\text{LO}}] / [kT_c]), \quad (3)$$

where the C_m are constants determined by the scattering rates, and normalization, and $r = \text{int}(\Delta E_c / \hbar\omega_{\text{LO}})$. The experimental basis for this model is shown in Fig. 2 of Ref. [10], which shows laser emission peaks spaced at $\hbar\omega_{\text{LO}}$ intervals above the bottom of the lowest energy subband. That these peaks are not associated with higher energy subbands is based on the fact that the next highest energy subband step is higher in energy than the GaAs L minima. Since eqn (3) is just a weighted sum of delta functions, it is sufficient to consider one of them to determine the form of the temperature dependence of J_{th} . Taking the spike with lowest energy, we simplify eqn (3) to

$$f_c(\epsilon) = \{(\pi n L_z \hbar^2) / (m^* k T_c)\} \delta(\epsilon - [\Delta E_c - \hbar\omega_{\text{LO}}] / [k T_c]), \quad (4)$$

where n is the electron density in the well.

Since the valence-band discontinuity ($\Delta E_v = \Delta E_g - \Delta E_c$) between AlGaAs and GaAs is of the order of $\sim \hbar\omega_{\text{LO}}$, the hole distribution function is expected to be close to a Fermi-Dirac distribution even for weak hole-hole interaction. Thus we assume

$$f_v(\epsilon - E) = 1 / \{1 + \exp(\epsilon - E - F_v)\}. \quad (5)$$

The hole quasi-Fermi level, F_v , is normalized to kT_c and is measured with respect to the minimum of the lowest energy confined-electron state. Of course, generally the hole temperature is not equal to T_c , but the use of T_h for

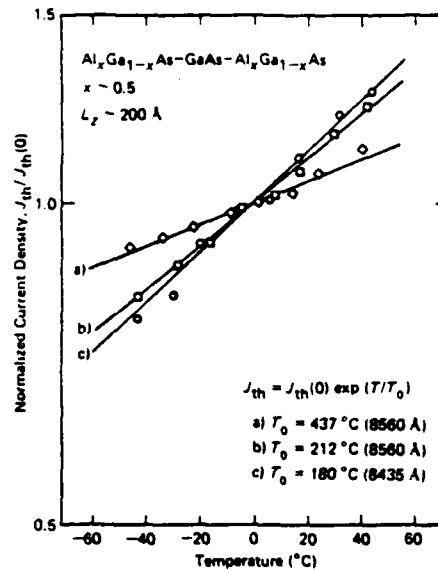


Fig. 2. Normalized threshold current density as a function of temperature for three single-quantum-well $\text{Al}_x\text{Ga}_{1-x}\text{As-GaAs}$ heterostructure laser diodes with GaAs active regions of size $L_z \sim 200 \text{ \AA}$. The solid lines represent the least squares fit of the data to the expression $J_{\text{th}}(T) = J_{\text{th}}(0) \exp(T/T_0)$. The device of curve (a) demonstrates that values of T_0 as high as 437°C are possible in quantum-well diodes. The decreased temperature dependence of J_{th} in all three diodes is consistent with calculated expressions for $J_{\text{th}}(T)$.

the hole temperature expressions and we assume $T_h = T_c$.

Using the densities described above, (situation) the net rate of spontaneous emission is the rate of spontaneous emission minus the rate of absorption, "k-selection-rule"

$$r_{\text{sp}}(E) = kT_c B \int_0^{\infty} \dots$$

$$r_{\text{sp}}(E) = kT_c B \int_0^{\infty} \dots$$

where B is related to the transition probability squared. E_{th} is the energy of the lowest energy confined-electron state. E_{ph} is the photon energy.

Following the rate equations for the number of photons, N

$$dn/dt = J / (eL_z) - \dots$$

$$dN/dt = -N/\tau + \dots$$

where η is the internal quantum efficiency, τ is the photon lifetime, and W is the volume of the laser. The number of photons per unit energy per unit volume is N/V .

where μ is the chemical potential. The first mode is assumed to be dominant, the second mode is neglected. Now that the threshold current density is given by J_{th} , we can write the rate equations as follows:

These two equations can be solved for N and J_{th} , which contain F_c , F_v , and n . So that an expression for J_{th} can be derived.

the hole temperature would give only more complicated expressions and no important new features. Therefore we assume $T_h = T_c$.

Using the densities of states and distribution functions described above, we calculate (assuming $\Delta n = 0$ transitions) the net rate of stimulated emission, $r_{st}(E)$, and the rate of spontaneous emission, $r_{sp}(E)$, using the "no k -selection-rule" model of Lasher and Stern[12]. Thus

$$r_{st}(E) = kT_c B \int_0^{E-E_{th}} dg_c(\epsilon) g_v(\epsilon - E) f_c(\epsilon) - f_v(\epsilon - E) \quad (6)$$

$$r_{sp}(E) = kT_c B \int_0^{E-E_{th}} dg_c(\epsilon) g_v(\epsilon - E) \times \{1 - f_v(\epsilon - E)\} f_c(\epsilon) \quad (7)$$

$$R_{sp} = kT_c \int_0^\infty dE r_{sp}(E), \quad (8)$$

where B is related to the average of the matrix element squared, E_{th} is the energy difference between the lowest energy confined-electron and confined-hole states, and E is the photon energy.

ANALYSIS

Following the method of Adams[14], we begin with the rate equations for the electron density, n , and the number of photons, N_M , in the M th lasing mode or

$$dn/dt = J/(eLz) - R_{sp}/\eta - \{mN_M r_{st}(E_M)\}/\{LWLz\Phi(E)} \quad (9)$$

$$dN_M/dt = -N_M/\tau_M + \{LWLz R_{sp}\}/M' + \{N_M r_{st}(E_M)\}/\Phi(E), \quad (10)$$

where η is the internal quantum efficiency of the spontaneous radiation, m is the number of lasing modes, L and W are the length and width of the device, τ_M is the photon lifetime in the lasing mode, and M' is the number of spontaneous modes. The number of modes per unit energy per unit volume is given by

$$\Phi(E) = \{\mu^3 E^2\}/\{\pi^2 \hbar^3 c^3\}, \quad (11)$$

where μ is the refractive index. For simplicity one lasing mode is assumed ($m = 1$) and since M' is typically quite large, the second term on the right side of eqn (10) is neglected. Now a steady state condition is assumed so that at threshold the two rate eqns (9) and (10) become:

$$J_{th} = R_{sp} e Lz / \eta \quad (12)$$

$$r_{st}(E_M) = \Phi(E) / \tau_M. \quad (13)$$

These two equations contain two unknowns, $r_{st}(E_M)$ and R_{sp} , which contain the unknown quasi-Fermi levels F_c and F_v . F_c and F_v can be used to relate $r_{st}(E_M)$ and R_{sp} so that an expression for J_{th} can then be obtained.

(a) *Strong electron-electron interaction (Fermi-Dirac distribution)*

In the limit of strong electron-electron interaction eqns (1), (2) and (5) can be used in eqns (6) and (7) and result in

$$r_{st} = -kT_c B g_c g_v \cdot \ln A \quad (14)$$

$$r_{sp} = -\{kT_c B g_c g_v \ln A\} / \{1 - \exp(E' + F'_v - F_c)\}, \quad (15)$$

where

$$A = \{[\exp(F_c) + \exp(E')][\exp(F'_v + E') + 1]\} / \{[\exp(F'_v + E') + \exp(E')][\exp(F_c) + 1]\} \quad (16)$$

and where $F'_v = F_v + E_{th}$, $E' = E - E_{th}$, and $a = F_c - F'_v$. In order to calculate R_{sp} , $\ln A$ is approximated in a piecewise linear fashion, giving

$$\ln(A) = \beta E' \quad \text{for } E' \approx 0 \quad (17a)$$

$$= (E' - a)/2 \quad \text{for } E' \approx a \quad (17b)$$

$$= E' - \ln(\gamma) \quad \text{for } E' \gg a. \quad (17c)$$

where

$$\beta = \{\exp(F'_v) / [\exp(F'_v) + 1] - \exp(F_c) / [\exp(F_c) + 1]\} \quad (18)$$

and

$$\gamma = [1 + \exp(-F'_v)] [1 + \exp(F_c)]. \quad (19)$$

Typically $F'_v \approx 0$ and $F_c > 1$ so that $\beta \approx -1/2$. Evaluation of eqn (8) yields

$$R_{sp} \approx (kT_c)^2 B g_c g_v \{3a/4 + \exp(-a)[2a + 1 - \ln(\gamma)] - (\beta a^2) / [8(1 - \exp(-a))]\}. \quad (20)$$

If the exponential term in eqn (20) dominates, we are left with

$$R_{sp} \approx (kT_c)^2 B g_c g_v [2a \exp(-a)]. \quad (21)$$

This gives the strongest temperature dependence of the threshold current. As can be seen from the following, the threshold current is almost independent of temperature if the a^2 term dominates. We now have to express r_{st} as a function of the quasi-Fermi levels, eliminate these terms, and solve for J_{th} . This can easily be done numerically. However, an explicit solution, which contains all the essential features, can be obtained by assuming that $E'_M = a/2$, so that

$$r_{st}(E'_M) = (kT_c) B g_c g_v a/4. \quad (22)$$

Relating eqns (12) and (13) through eqns (21) and (22) results in the following expression for J_{th} :

$$J_{th} = \{[8eLz\Phi(E)] / [\eta\tau_M]\} (kT_c) \exp(-T^*/T_c). \quad (23)$$

$$J_{th}(T_c) \quad (29)$$

approximately
weakly with the

quantum-well
insensitive to
s (23) and (29).
les with single
As described
consist of five
ganic chemical
C employing
present work
the following
 $10^{18}/\text{cm}^3$), (2)
 $\times 10^{17}/\text{cm}^3$), (3)
, (4)
 $10^{17}/\text{cm}^3$), and
the first layer is
ate. The quan-
configuration
m temperature

odes is deter-
sity measure-
res between
perature held
defined as the
the high level
ent curve with
2 effects, the

as a function
quantum-well-
2. In order to
 J_{th} for these
function (DH)
ent the least-
expression

$$(30)$$

ance. A high
temperature
 T_0 is in the
m-well struc-
be observed.
ble. For (b)
is is thought
sion process
and (c) to
contacts. It is
ature wafer

sity, $J_{th}(T)$,
ative region

typical of a quantum-well heterostructure laser diode has been presented. In this analysis a step-like density of states has been used, and not the usual bulk-crystal parabolic density of states, which does not fit quantum-well heterostructures. Two limiting cases of weak and strong electron-electron interaction of the injected carriers have been considered. In both limits the threshold current density has been found to vary approximately linearly with carrier temperature, and to be only weakly dependent on lattice temperature which agrees with experiment. Data on single-quantum-well $\text{Al}_x\text{Ga}_{1-x}\text{As}$ - GaAs heterostructure diodes ($L_x \sim 200 \text{ \AA}$) have been presented showing that in the conventional expression $J_{th}(T) = J_{th}(0) \exp(T/T_0)$ the temperature parameter T_0 can be as high as at least 437°C .

Acknowledgements—For assistance in portions of this work we wish to thank Yuri S. Moroz, R. T. Gladin, B. L. Marshall and B. L. Payne (Urbana), and J. E. Cooper, N. L. Lind, L. A. Moudy, T. J. Raab and J. J. Yang (Anaheim). We are particularly grateful to R. D. Dupuis for his contributions to the earlier phase of this work, and to J. J. Coleman and G. E. Stillman for helpful conversations. The work of the Illinois group has been supported by the national Science Foundation, primarily Grant DMR 76-81432 and to a lesser extent DMR 77-23999, and also Navy Contract N00014-79-C-0768; the work of the Rockwell group has been supported by the Office of Naval Research, Contract N00014-78-C-0711.

REFERENCES

1. V. N. Lutsikii, *Phys. Stat. Sol.* (a)1, 199 (1970).
2. F. Stern and W. E. Howard, *Phys. Rev.* 163, 816 (1967).
3. E. A. Rezek, N. Holonyak, Jr., B. A. Vojak, G. E. Stillman, J. A. Rossi, D. L. Keune and J. D. Fairng, *Appl. Phys. Lett.* 31, 288 (1977).
4. E. A. Rezek, N. Holonyak, Jr., B. A. Vojak and H. Shichijo, *J. Appl. Phys.* 49, 69 (1978).
5. R. D. Dupuis, P. D. Dapkus, N. Holonyak, Jr., E. A. Rezek, and R. Chin, *Appl. Phys. Lett.* 32, 295 (1978).
6. R. D. Dupuis, P. D. Dapkus, R. Chin, N. Holonyak, Jr. and S. W. Kirchoefer, *Appl. Phys. Lett.* 34, 265 (1979).
7. R. D. Dupuis, P. D. Dapkus, N. Holonyak, Jr. and R. M. Kolbas, *Appl. Phys. Lett.* 35, 487 (1979).
8. R. D. Dupuis, *Appl. Phys. Lett.* 35, 311 (1979).
9. N. Holonyak, Jr., R. M. Kolbas, W. D. Laidig, M. Altarelli, R. D. Dupuis and P. D. Dapkus, *Appl. Phys. Lett.* 34, 502 (1979).
10. R. M. Kolbas, N. Holonyak, Jr., B. A. Vojak, K. Hess, M. Altarelli, R. D. Dupuis and P. D. Dapkus, *Solid-St. Commun.* 31, 1033 (1979). See also N. Holonyak, Jr., R. M. Kolbas, W. D. Laidig, B. A. Vojak, K. Hess, R. D. Dupuis and P. D. Dapkus, *J. Appl. Phys.* 51 (To be published) (1980).
11. R. Chin, N. Holonyak, Jr., B. A. Vojak, K. Hess, R. D. Dupuis and P. D. Dapkus, *Appl. Phys. Lett.* 36, 19 (1980).
12. G. Lasher and F. Stern, *Phys. Rev.* 133, A553 (1964).
13. F. Stern, *Phys. Rev.* 148, 186 (1966).
14. M. J. Adams, *Solid-St. Electron.* 12, 661 (1969).
15. R. Dingle, W. Wiegmann and C. H. Henry, *Phys. Rev. Lett.* 33, 827 (1974).
16. R. D. Dupuis, P. D. Dapkus, N. Holonyak, Jr., R. M. Kolbas, W. D. Laidig and B. A. Vojak, *Pis'ma Zh. Tekh. Fiz.* 5, 132 (1979) (*Sov. Tech. Phys. Lett.* 5, 52 (1979)).
17. J. Shah, *Solid-St. Electron.* 21, 43 (1978).
18. I. Hayashi, M. B. Panish and F. K. Reinhart, *J. Appl. Phys.* 42, 1929(1971).

Induced phonon-sideband laser operation of large-quantum-well $\text{Al}_x\text{Ga}_{1-x}\text{As-GaAs}$ heterostructures ($L_z \sim 200\text{--}500 \text{ \AA}$)

14

J. J. Coleman and P. D. Dapkus

Rockwell International, Electronics Research Center, Anaheim, California 92803

B. A. Vojak, W. D. Laidig, and N. Holonyak, Jr.

Department of Electrical Engineering and Materials Research Laboratory, University of Illinois at Urbana-Champaign, Urbana, Illinois 61801

K. Hess

Department of Electrical Engineering and Coordinated Science Laboratory, University of Illinois at Urbana-Champaign, Urbana, Illinois 61801

(Received 29 January 1980; accepted for publication 8 April 1980)

Data are presented on photopumped metalorganic chemically vapor-deposited $\text{Al}_x\text{Ga}_{1-x}\text{As-GaAs}$ quantum-well heterostructures with active regions consisting of a large GaAs quantum well ($L_{z1} \sim 200, 500 \text{ \AA}$) coupled to a phonon generating array of seven small GaAs wells ($L_{z2} \sim 50 \text{ \AA}$). Phonon-sideband laser operation below the confined-carrier transitions of the large GaAs quantum well(s) is induced by the large number of phonons generated in the smaller GaAs wells. The induced phonon-sideband laser operation (of a larger quantum well by an array of smaller wells) leads to a measurement of the energy difference between the first-state light- and heavy-hole energies of a 200- \AA GaAs quantum well (4.9 meV) and directly to the GaAs LO-phonon energy $\hbar\omega_{\text{LO}} \approx 41.0 - 4.9 = 36.1 \text{ meV}$.

PACS numbers: 42.55Px, 78.55 - m, 71.38 + i, 81.15Gh

In contrast to the usual bulk crystal form of double-heterostructure (DH) lasers, quantum-well heterostructures (QWH's), as recently shown,¹⁻⁶ are capable of laser operation on phonon sidebands. This is a consequence of the quasi-two-dimensional nature of quantum-well heterostructures and their steplike density of states.^{2,5,6} In previous work the possibility has been raised that stimulated phonon emission can occur in QWH lasers^{2,5,6} and should be most apparent in a multiple-well structure that forms a phonon resonator or cavity. To study these effects, in the present work we have constructed (and photopumped) two different metalorganic chemically vapor-deposited (MO-CVD) $\text{Al}_x\text{Ga}_{1-x}\text{As-GaAs}$ multiple-quantum-well heterostructures, one with a single large GaAs well of size $L_z \sim 200 \text{ \AA}$ coupled to a phonon generating array of seven small GaAs wells of size $L_z \sim 50 \text{ \AA}$ and the second the same in form but with a single large well of size $L_z \sim 500 \text{ \AA}$. As shown below, in both heterostructures laser operation is observed one phonon below the lowest confined-particle states of the large wells, which is a much weaker or even nonexistent effect in a single-large-well heterostructure.^{6,7} The induced phonon-sideband laser operation of the larger wells leads to the result $\hbar\omega_{\text{LO}} = 36.1 \text{ meV}$, which is in good agreement with other measurements of $\hbar\omega_{\text{LO}}$ (GaAs).^{8,9}

The $\text{Al}_x\text{Ga}_{1-x}\text{As-GaAs}$ QWH's of interest here are grown by metalorganic chemical vapor deposition¹⁰⁻¹² on {100} GaAs substrates. Layer reproducibility is insured by electronically controlled gas flow rates and growth times. Following the growth of a GaAs buffer layer, a $\sim 1\text{-}\mu\text{m}$ -thick $\text{Al}_x\text{Ga}_{1-x}\text{As}$ ($x \sim 0.35$) confining layer is grown. Next follows the multiple-quantum-well active region as described above with $\text{Al}_x\text{Ga}_{1-x}\text{As}$ barrier layers of composition $x \sim 0.32$. The resulting effective electron potential in the active region is shown in the inset of Fig. 1. Last is a $\sim 0.3\text{-}\mu\text{m}$ $\text{Al}_x\text{Ga}_{1-x}\text{As}$ confining layer ($x \sim 0.35$) like the first. All

layers are undoped ($n_i - n_j \leq 10^{15}/\text{cm}^3$); their sizes in all cases have been verified by SEM photomicrographs of shal-

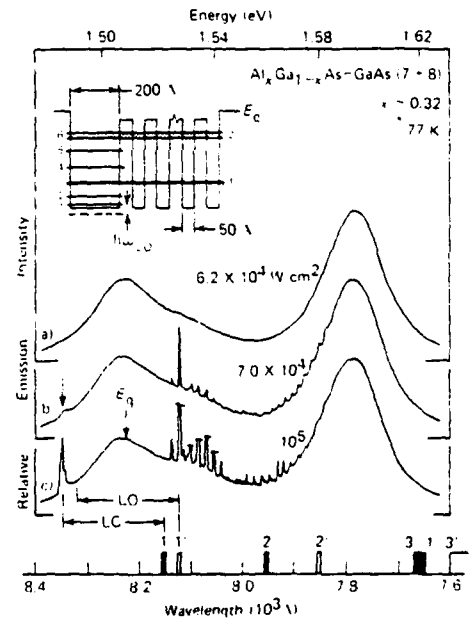


FIG. 1. Emission spectra (77 K) of a photopumped multiple-quantum-well $\text{Al}_x\text{Ga}_{1-x}\text{As-GaAs}$ heterostructure grown by MO-CVD. The rectangular sample is undoped ($n_i - n_j \leq 10^{15}/\text{cm}^3$) and contains an active region consisting of one 200- and seven 50- \AA GaAs wells coupled by seven 50- \AA $\text{Al}_x\text{Ga}_{1-x}\text{As}$ ($x \sim 0.32$) barriers as illustrated in the inset. The confined-electron energy levels of the 200- \AA GaAs well (left-hand side, 1-6) and the 50- \AA multilayer (right-hand side, 1 and 2) are shown in the inset. With increase in photopumping ($\lambda \sim 5145 \text{ \AA}$) from (a) $6.2 \times 10^4 \text{ W/cm}^2$ to (b) $7.0 \times 10^4 \text{ W/cm}^2$ the $n = 1$ transition begins to lase while simultaneously a spontaneous bump appears (b,) one phonon below the $n = 1$ transition. With higher pump power (c, 10^5 W/cm^2) the induced phonon-sideband transition (LO) also lases.

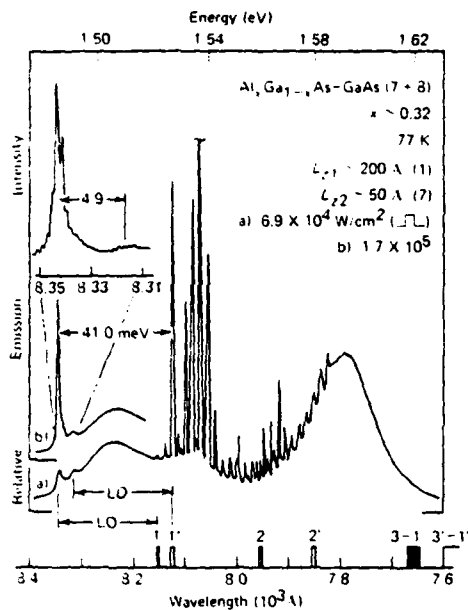


FIG. 2. Pulsed laser operation (77 K) of the same sample as in Fig. 1, with the excitation adjusted to permit observation of induced phonon-sideband emission $\hbar\omega_{LO}$ below both the $n = 1$ and $n' = 1'$ transitions [(a) 6.9×10^4 W/cm²]. With an increase in pump power along with a slight adjustment of the excitation spot on the sample the 1-LO sideband can be made to lase [(b) 1.7×10^5 W/cm²]. From the expanded part of the spectrum in the inset the light-hole-heavy-hole energy difference is determined to be 4.9 meV for a 200-Å GaAs layer and, as shown, $\hbar\omega_{LO} \approx 41.0 - 4.9 = 36.1$ meV.

low-angle cross sections,¹³ which agree with experimental observations (spectra) of the confined-particle transitions (identified on narrow samples 10–20 μm).^{5,6}

The MO-CVD $\text{Al}_x\text{Ga}_{1-x}\text{As-GaAs}$ quantum-well heterostructures described above and shown in part in the inset of Fig. 1 are a design modification of the six-well ($L_z \sim 50$ Å) quantum-well heterostructure corresponding to curve (b) of

Fig. 1 in Ref. 2. These and related data,^{2,5} as well as recent analytical results and further data,¹⁴ show that the nonthermal phonon occupation number N_q^{nt} can, in quantum-well heterostructures, be increased well above ($\geq 500\times$, 77 K) the equilibrium value. This behavior has a profound effect in the present case because the large nonthermal phonon density generated in the closely coupled small wells can influence (stimulate) phonon generation and carrier scattering to lower energies in the larger coupled auxiliary (or "detector") quantum well(s). For example, a highly excited large lone quantum well delivers recombination radiation from collected hot carriers from near E_g to high above the band edge, as high as ~ 300 meV,⁷ but does not exhibit equally strong emission below the lowest confined-particle states (or E_g) unless assisted, as in the present work (Figs. 1–3).

The multiple-quantum-well heterostructures of interest here do not deliver appreciable recombination radiation higher than one phonon below the lowest states of the small wells, which in Figs. 1–3 is at $\lambda \sim 7750$ Å (or $E_g + 90$ meV). The coupled small wells cut off recombination from higher in the larger single 200-Å well (Figs. 1 and 2) or single 500-Å well (Fig. 3). Photogenerated higher-energy carriers are collected (from the confining layers) in the active region and tunnel into the small-well section; scatter downward, generating phonons in an efficient layered structure (seven coupled 50-Å GaAs wells) that can act as a phonon cavity^{2,5,6}; and then at much lower energy tunnel back into the big well for further scattering and recombination. The phonons generated in the small-well section assist the further downward scattering in the single large well, and lead to the unique form of low-energy laser operation shown at $\lambda \approx 8343$ Å in Figs. 1 and 2 and $\lambda \approx 8400$ Å in Fig. 3.

The data of Fig. 1 are unique. The high-level spontaneous emission intensity, obtained by photopumping across part of the width of a rectangular sample,^{1,2,5,6} is given by curve (a). When the photopumping is slowly increased from

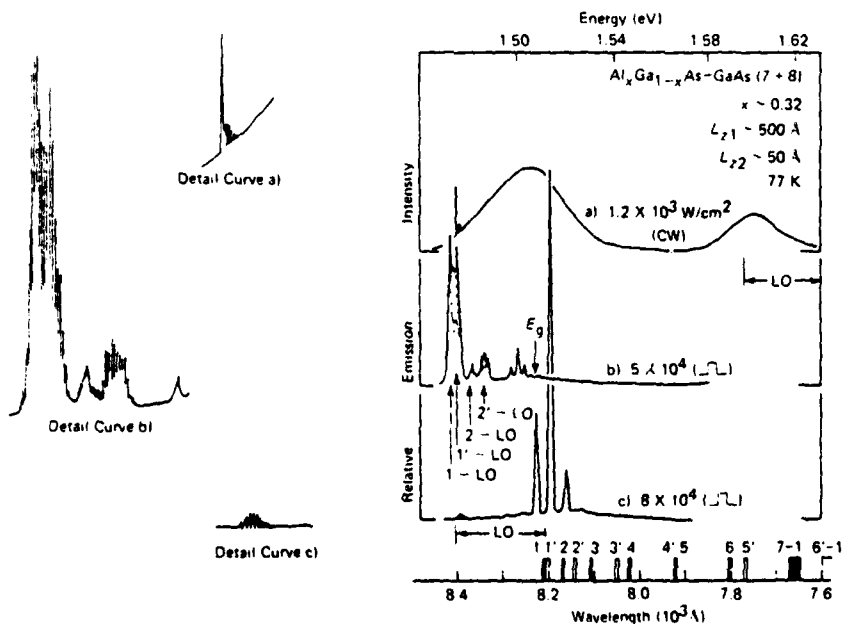


FIG. 3. Induced phonon-sideband laser operation (77 K) of a 500-Å GaAs well closely coupled to a phonon-generating multiple-quantum-well heterostructure consisting of seven GaAs wells coupled with 50-Å $\text{Al}_x\text{Ga}_{1-x}\text{As}$ ($x \sim 0.32$) barriers (see inset of Fig. 1). With cw excitation [(a) 1.2×10^3 W/cm²] the phonon sideband of the $n' = 1'$ transition lases from end to end along the rectangular sample ($254 \times 59 \mu\text{m}^2$). The emission peak at $\lambda \sim 7750$ Å occurs on the phonon sideband of the $n' = 1'$ transitions of the small-well section, which are degenerate with the larger well $n' = 6'$ transition. With pulsed excitation of 5×10^4 W/cm² (b) the sample lases on 1-LO, 1'-LO, 2-LO, 2'-LO, and edge to edge in the range 3-LO to 3'-LO. A narrower sample [(c) $23 \mu\text{m}$, 8×10^4 W/cm²], with large cavity end losses, shows that laser operation can be forced up in energy to the confined carrier transitions while phonon sideband emission is still observed in the range 1-LO to 1'-LO.

6.2×10^4 to 7.0×10^4 W/cm², a single laser mode emerges abruptly on the first electron-to-light-hole ($n' = 1'$) transition and simultaneously a prominent bump appears on the (b) curve one phonon below the first electron-to-heavy-hole ($n = 1$) transition ($E_1 - \hbar\omega_{LO}$). At still higher pumping (c) the $n' = 1'$ mode still predominates, and the transition at $E_1 - \hbar\omega_{LO}$ narrows into stimulated emission. The excitation can be adjusted on the sample slightly, giving the data of Fig. 2. The $n' = 1'$ mode is still identifiable and an LO phonon below $n' = 1'$ and below $n = 1$ two bumps appear due to rapid light-hole-to-heavy-hole relaxation ($\sim 10^{-12}$ s). We can expand this portion of the spectrum (inset) and measure, accurately, as shown, the $1' - 1$ spacing and in turn the LO phonon energy, which is $\hbar\omega_{LO} \approx 41.0 - 4.9 = 36.1$ meV.

It is clear that if the data and ideas above are correct, by merely increasing the size of the larger well we should be able to shift the lower confined-particle transitions (to still lower energy) and with them the induced phonon-sideband emission lines. This is what is observed in Fig. 3 for a larger well of size $L_z \sim 500$ Å. At a fairly high level just above the threshold for stimulated emission [(a) 1.2×10^4 W/cm², cw], length-to-length ($l \sim 254$ μm) laser modes appear abruptly on $n' = 1'$ (or $1'$ -LO). Then at higher pulsed excitation [(b), 5×10^4 W/cm²], further end-to-end modes appear at 1-LO, 2-LO, 2'-LO, which is quite remarkable, and still one more set of modes appears (edge to edge, $w \sim 59$ μm) at $\lambda \sim 8260$ Å, which is in the range one phonon below transitions 3 and 3'. These transitions (3, 3') have a higher density of states and higher oscillator strength, which could explain their involvement in edge-to-edge laser operation.

Note that the laser emission on the phonon sidebands in (b) of Fig. 3 is the dominant recombination radiation, i.e., is not a weak effect if the sample is of sufficient size. If we reduce the sample width sufficiently (to $w \sim 23$ μm) and thus increase the cavity end losses, as in Fig. 3(c), the main laser operation, on widely spaced edge-to-edge modes, moves up to the region of the lowest confined-particle transitions and the band edge, which is nearby (~ 2.4 meV). Even in this case weak end-to-end ($l \sim 211$ μm) laser modes are observed

in the region $1'$ -LO, 1-LO.

We interpret the unique location and manner of turn-on of the spectral bump and emission line marked by the arrow in Fig. 1 and the various LO arrows on Fig. 3(b) as a sign of stimulated phonon emission. In addition, we have been able to measure the first-state light-hole-heavy-hole quantum-well energy separation and measure directly the LO phonon energy in GaAs ($\hbar\omega_{LO} = 36.1$ meV).

We wish to thank Yuri S. Moroz, R.T. Gladin, B.L. Marhsall, and B.L. Payne (Urbana) for technical assistance. The work of the Illinois group has been supported by NSF Grants DMR 79-09991 and DMR 77-23999 and Navy Contract N000 14-79-C-0768; the work of the Rockwell group has been partially supported by the Office of Naval Research, Contract N000-14-78-C-0711.

¹N. Holonyak, Jr., R. M. Kolbas, W. D. Laidig, M. Altarelli, R. D. Dupuis, and P. D. Dapkus, Appl. Phys. Lett. 34, 502 (1979).

²R. M. Kolbas, N. Holonyak, Jr., B. A. Vojak, K. Hess, M. Altarelli, R. D. Dupuis, and P. D. Dapkus, Solid State Commun. 31, 1033 (1979).

³B. A. Vojak, N. Holonyak, Jr., R. Chin, E. A. Rezek, R. D. Dupuis, and P. D. Dapkus, J. Appl. Phys. 50, 5835 (1979).

⁴E. A. Rezek, R. Chin, N. Holonyak, Jr., S. W. Kirchoefer, and R. M. Kolbas, J. Electron. Mater. 9, 1 (1980).

⁵N. Holonyak, Jr., R. M. Kolbas, W. D. Laidig, B. A. Vojak, K. Hess, R. D. Dupuis, and P. D. Dapkus, J. Appl. Phys. 51, 1328 (1980).

⁶N. Holonyak, Jr., R. M. Kolbas, R. D. Dupuis, and P. D. Dapkus, IEEE J. Quantum Electron. QE-16, 170 (1980).

⁷N. Holonyak, Jr., R. M. Kolbas, E. A. Rezek, R. Chin, R. D. Dupuis, and P. D. Dapkus, J. Appl. Phys. 49, 5392 (1978).

⁸K. Hess, Appl. Phys. Lett. 35, 484 (1979).

⁹A. Mooradian and G. Wright, Solid State Commun. 4, 431 (1966).

¹⁰H. M. Manasevit, J. Electrochem. Soc. 118, 647 (1971).

¹¹R. D. Dupuis and P. D. Dapkus, in Proceedings of the Seventh International Symposium on GaAs and Related Compounds, St. Louis, 1978, edited by C. M. Wolfe (Institute of Physics, London, 1979), pp. 1-9.

¹²R. D. Dupuis and P. D. Dapkus, IEEE J. Quantum Electron. QE-15, 128 (1979).

¹³N. Holonyak, Jr., B. A. Vojak, R. M. Kolbas, R. D. Dupuis, and P. D. Dapkus, Solid State Electron. 22, 431 (1979). Note that this measuring technique has been further refined with Dektak (Sloan Instruments) angle and SEM layer measurements and now gives good size estimates.

¹⁴K. Hess, N. Holonyak, Jr., W. D. Laidig, B. A. Vojak, J. J. Coleman, and P. D. Dapkus, Solid State Commun. (to be published).

Hot electrons in layered semiconductors

The size of semiconductor devices has decreased so much that classical treatments of semiconductor physics become invalid and effects involving supra-thermal electrons take on a new importance.

Karl Hess and Nick Holonyak, Jr

As electronic systems—and especially computers—are used more and more widely in almost all areas of endeavor and daily life, the semiconductor technology on which they are based is being pushed to ever larger-scale integration and ever greater miniaturization. As the devices get smaller, and smaller, new problems (and maybe new opportunities) appear.¹

One consequence of the reduction in size is that the fields accelerating electrons and holes through the crystal become very large, so that the carriers acquire large kinetic energies. The equations of motion for an energetic electron in the lattice can be appreciably different from Newton's laws; its (inertial) mass can, for example, appear to be infinite or even negative. This has nothing to do with relativistic effects but is due to Bragg reflection. The non-linearity of the equation of motion is illustrated in figure 1, which shows lines of equal energy in momentum space (*k*-space) for the semiconductor gallium arsenide.² For a free particle, these lines would be circles, as they are near the origin in figure 1, because the energy depends only on the magnitude of the momentum. The complicated shapes of the curves for large *k* indicates that the relation between energy and momentum is anisotropic and not quadratic. Electrons then do not necessarily move in the direction of the electric field and their average speed is

not simply proportional to the field strength; that is, Ohm's law breaks down. We shall discuss this point more extensively later.

To illustrate the reduction in size that has accompanied the progress of semiconductor technology, we show in figure 2 the original point-contact transistor and a modern layered quantum-well heterostructure. (We should point out, though, that the point-contact transistor was a much smaller device than the junction transistors that were subsequently most widely used in practical devices.)

As we mentioned, the electric fields in small devices can become very large. If we assume that operating voltages of semiconductor devices are around 5 V, then the maximum electric fields in a typical device of twenty years ago was on the order of 10–100 V/cm. In a present-day integrated circuit the average fields are 10^3 V/cm and maximum fields are an order of magnitude larger. At such field strengths silicon and germanium become non-Ohmic at room temperature.³ Fields on the order of 10^5 V/cm are encountered between neighboring gates of charge-coupled devices and in quantum-well layered devices. Such large fields may also be approached in the very-large-scale integrated circuits that are now being developed.

At fields larger than 1000 volts/cm the charge carriers in a semiconductor are accelerated far above their thermal-equilibrium energy (given by the lattice temperature). Under these circumstances so-called "hot-electron effects" become important and many of the familiar concepts of semiconductor physics lose their validity. In this

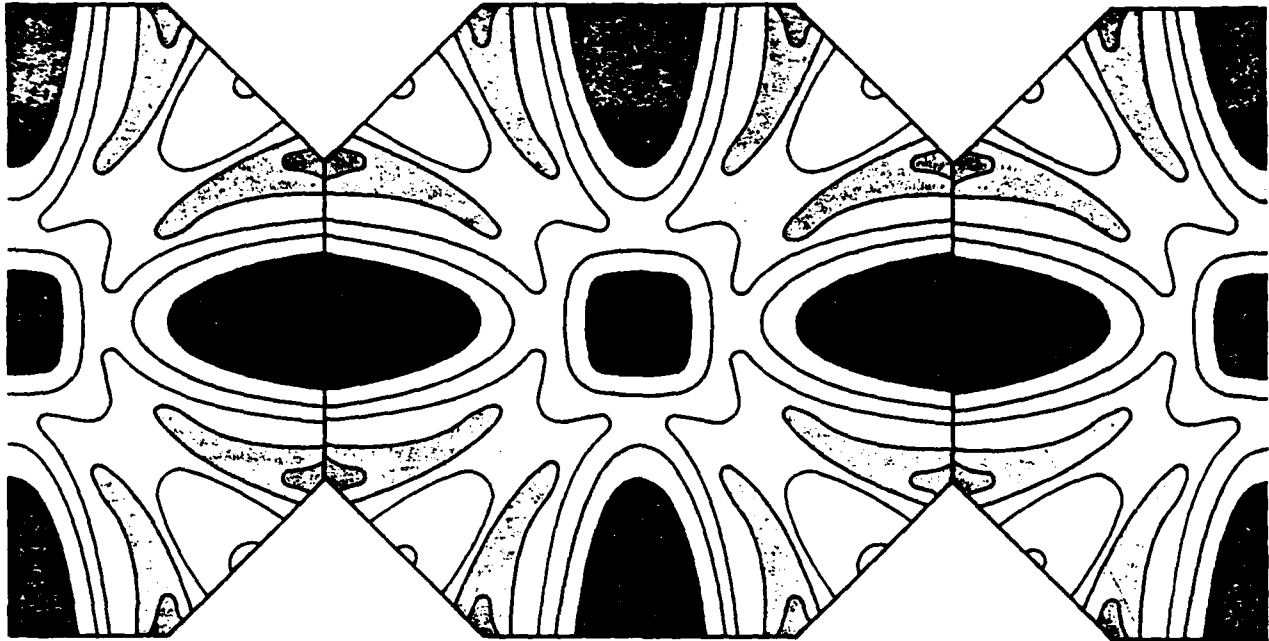
article we will discuss some of the effects that will be important in future very-large-scale integrated circuits and in optoelectronic devices.

Hot electrons

As electrons move through the crystal lattice, they interact both with each other and with the lattice. In electronic devices, the applied electric field supplies energy to the electrons. If electron–electron collisions randomize the carrier energy, one can define a temperature for the electrons even for very high fields. This temperature T_e is always higher than the temperature of the crystal lattice T_L . The difference between T_e and T_L depends strongly on the electric field (actually on the square of the field because reversal of the field must not lead to negative temperatures) and on the details of how the electrons lose their energy. In all practical cases the electrons lose their energy to lattice vibrations. We thus have a picture of a highly mobile fluid at high temperature (the "electron gas") moving through the cooler crystal lattice and losing energy to it.

We know that conducting wires begin to glow if too much energy is transferred from the electron gas to the crystal lattice. We would like to emphasize, however, that even if the lattice remains cold (a situation that often can be arranged), the temperature of the electrons can be exceedingly high and cannot be controlled by any cooling mechanism (other than the slow heat loss to the lattice). A typical example would be a piece of silicon, let us say, to which an electric field of 2×10^4 V/cm is applied; the electron temperature rises to 1000 K no matter what the

The authors are professors of Electrical Engineering at the University of Illinois, Urbana. Karl Hess is also a member of the Coordinated Science Laboratory and Nick Holonyak is also a member of the Materials Research Laboratory at the University.



Surfaces of equal energy in the Brillouin zone of gallium arsenide calculated by the empirical pseudopotential method. (The Brillouin zone is the hexagonal area; the figure shows a somewhat extended

zone.) Ohm's Law holds only for electrons at the lowest energy (dark gray). The carrier energy increases from gray (center) to white to red to dark red in steps of 0.5 eV. Figure 1

temperature of the surrounding medium or heat sink attached to the sample. One consequence of this rise in temperature is that the conductivity drops because of the Bragg reflection mentioned earlier and because hot electrons can excite more lattice vibrations than cooler (lower-energy) electrons. The electrons are thus less mobile, being scattered more often. The conductivity therefore depends on the field strength and Ohm's law is not valid at these high fields. It is worth mentioning that the heating of the electron gas (not the lattice) is very fast: Typically, the time constant is 10^{-12} sec.⁴

Keeping the electron gas in equilibrium with the lattice would mean using smaller electric fields. As the devices get smaller, the voltages would thus also have to get smaller. However, for various reasons it is unlikely that the supply voltages applied to semiconductor devices can be reduced below one volt. One reason is the variation in threshold voltages of the component devices. Another is that the built-in voltages (or potentials) of semiconductor devices are of the order of the semiconductor energy gap, which is a property of the crystal, and cannot be scaled down. We can therefore expect that future semiconductor devices will inevitably involve hot-electron effects in their operation. It is not clear, however, which of the various hot-electron effects will be most important. Current device concepts that might

involve hot-electron effects are carrier (electron or hole) drift, diffusion, generation-recombination, and thermionic emission over potential barriers.⁵

Clearly it will not be possible to cover all possibilities in a short article. We therefore concentrate, as examples, on effects specific to hot electrons in potential wells. The reason for this choice is that with shrinking crystal size the charge carriers become increasingly confined to narrow potential wells as defined by the size of the components.

Layered devices

To illustrate the effects one expects with narrow potential wells and high electric fields, consider the layered structure shown in figure 2. The general properties of such a structure are sketched in figure 3. The layers could be InP and InGaPAs (as in the sample shown in figure 2) or (as in figure 3) GaAs and $\text{Al}_x\text{Ga}_{1-x}\text{As}$; these layers have now been produced by several different methods, including molecular-beam epitaxy, metal-organic chemical vapor deposition and liquid-phase epitaxy. The layers in these structures range from 10^{-6} to 10^{-5} cm in thickness. Such structures are in many ways prototypes of a variety of devices including field-effect transistors and charge-coupled devices.

On the small scale of these layers, charge-neutrality is not preserved because electrons move from one layer

into another without creating substantial electric fields, that is, they leave regions of high potential energy and move into potential minima.

In the sandwich shown in figure 3, $\text{Al}_x\text{Ga}_{1-x}\text{As}$ -GaAs- $\text{Al}_x\text{Ga}_{1-x}\text{As}$, the properties of the electrons change substantially in the middle layer:

► Because of the constraining AlGaAs layers the electrons are not free to move perpendicular to the layers and hence form a two-dimensional gas. As a consequence, their minimum energy (remember the famous quantum-mechanical problem of a particle in a box) lies above the GaAs conduction band edge (E_c). We refer to this effect as "size quantization."⁶

► The electrons in their motion are scattered either by lattice vibrations (phonons) or by various impurity centers, which can be small in number in the GaAs. The "remote" impurities (electron donors or acceptors) in the layers of $\text{Al}_x\text{Ga}_{1-x}\text{As}$ do not influence the electron motion. As a consequence, the electrons in the GaAs layer are more mobile as compared to bulk material if the donors are mainly in the $\text{Al}_x\text{Ga}_{1-x}\text{As}$ layers. This notion was proposed originally by Raphael Tsu and Leo Esaki (IBM) and recently demonstrated by Raymond Dingle, Arthur Gossard, Horst Stormer and William Wiegmann (Bell Labs).⁷

Less well known than the impurity-scattering case above is the fact that the scattering of electrons by lattice

vibrations also is different in layered structures from what is normally expected.⁵ As an example consider a GaAs-Ge heterostructure, that is, a germanium layer epitaxially grown on gallium arsenide. A polarized lattice vibration propagates in the gallium arsenide and creates macroscopic electric fields that extend near the interface into the germanium. This behavior is reminiscent of the fringing fields of a parallel-plate capacitor. The fields

fringing from the gallium arsenide scatter the electrons in the neighboring germanium, which is a covalent non-polar material and normally would not exhibit polar scattering. In other words, the electrons in the germanium are scattered by the "remote" lattice vibrations of the gallium arsenide.

In some systems (such as the InSb-SiO₂ structures designed for infrared applications) the remote scattering mechanism may reduce significantly

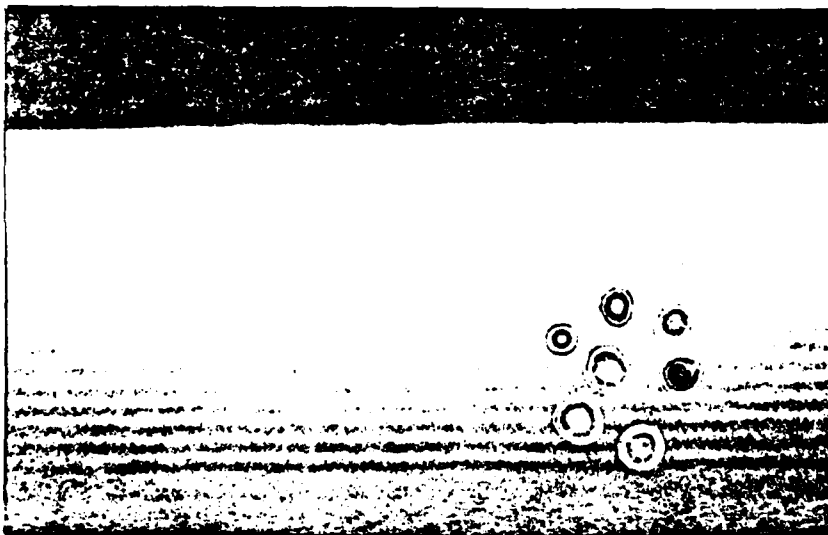
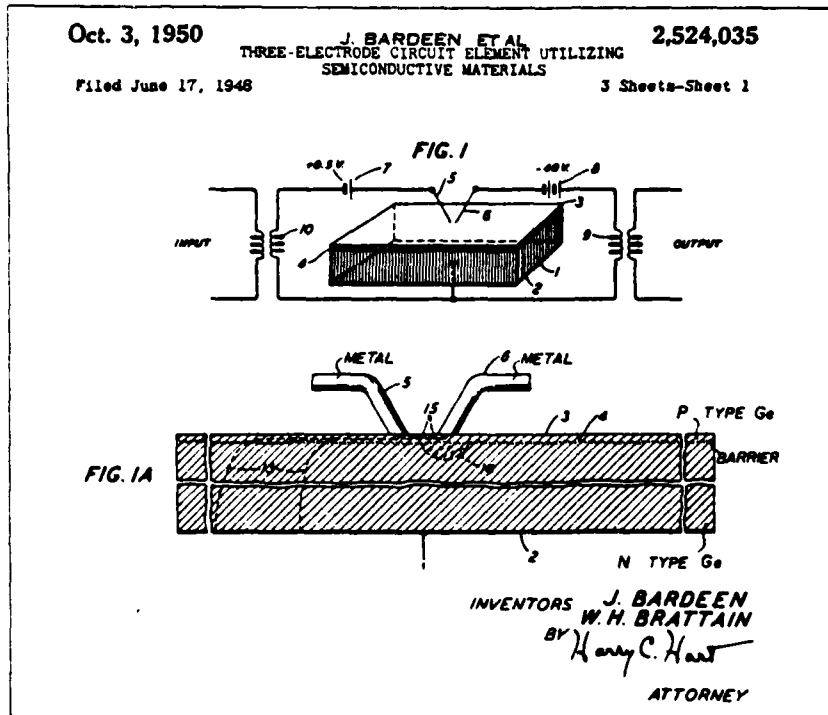
the interface mobility of electrons and hence the device speed.

Let us return to the layers of GaAs and Al_xGa_{1-x}As (figure 3) and assume the electrons are in the middle layer (GaAs) before we apply an electric field parallel to the interfaces. As long as the applied electric field is small, the electrons will stay in the GaAs. For large electric fields, however, the electrons will be heated, and move up in energy, and finally when their energy approaches the band edges in the surrounding Al_xGa_{1-x}As, they can transfer out into the adjacent layers. It is clear that this effect has a close analogy to thermionic electron emission out of glowing wires, as in a vacuum tube, or to the momentum-space electron transfer that occurs in the Gunn effect, which is the basis for useful microwave devices. A Monte Carlo simulation of the electron trajectory for carrier transport in a thin (400 Å) GaAs layer is shown in figure 4. For an under-critical field, the electron stays in the GaAs well. For a field above a critical threshold, the electron can transfer out into the surrounding Al_xGa_{1-x}As. A variety of effects perhaps can be created using the mechanism of hot-electron transfer out of thin layers.⁹ Some of these have just recently been verified experimentally.

Very-large-scale integration

At this point let us turn to more established ground and consider the hot-electron effects that occur in very-large-scale integrated circuits. Tak H. Ning at IBM has shown¹⁰ that in the metal-oxide-semiconductor system (so important in present-day integrated circuitry) electrons can be emitted from silicon into the silicon dioxide over potential barriers that are quite large. In the silicon dioxide the electrons are finally trapped and give rise to unwelcome changes in the interface potential, causing instabilities in the device performance. These effects occur on long time scales, but are important in general.

An even more pronounced example is the so-called "buried-channel structure," which is diagrammed in figure 5. This structure was conceived to avoid trapping of electrons at the silicon-silicon-dioxide interface. The crucial feature is that of an ion-implanted layer which creates the potential-energy profile shown in the lower part of the figure. As in the case of the GaAs-AlGaAs layers discussed above, the electrons are at minimum potential energy (between x_n and x_p) far away from the silicon-silicon-dioxide interface. Structures such as this are used for charge-coupled devices and metal-oxide-semiconductor transistors. If we now shrink the device, we obtain much higher electric fields, which,



Evolution of the size of electronic devices. (a) Original transistor patent of John Bardeen and Walter Brattain: The germanium crystal is about 0.1-0.5 cm in size, while the spacing between the emitter and the collector (labelled 5 and 6) is considerably smaller. (b) Layered structure: a quantum-well heterostructure laser, of InGaPAs quaternary compounds grown by liquid-phase epitaxy. To illustrate the layer sizes, leukemia viruses of about 500 to 1000 Å diameter are shown superimposed on the crystal layers. Figure 2

when the device is in operation, accelerate and heat the electrons. The consequence is that electrons can be thermionically emitted to the interface, again as occurred for the GaAs-AlGaAs layers. The device then loses its advantage of being a buried-channel device; we have reached a limit in how much we can reduce the size of the device.

Of course, high electric fields also influence the electron drift within the potential wells themselves, even before thermionic emission occurs. In metal-oxide-semiconductor devices, therefore, the drift velocity of electrons always saturates with increasing electric field. The reason for this is the enhanced scattering of hot electrons by lattice vibrations, as has long been known.

The mechanisms described above have drastic effects on device properties. We should also expect a dramatic influence of high fields on carrier diffusion. Steep concentration gradients and high electric fields totally invalidate the basic concept of particle diffusion as described by the classic Einstein relation, $D = \mu kT/e$. Preliminary investigations show that the usual diffusion constant, D , has to be replaced by a rather complex expression even if the device is large enough that the electron is not able to traverse it without collisions, which clearly violates the basic ideas about diffusion.¹¹ This brings us to the limiting size of small devices: If we shrink the size still further, how long do we have enough electrons to apply familiar statistical concepts, and what is the limit of size for ballistic transport of charge carriers? That is, where does the semiconductor become like a vacuum for the electron? The answers to these questions are urgently needed; a number of commercial semiconductor products touch these borders already, and clearly many more will in the near future.

Before turning to opto-electronic layered-structure devices, specifically quantum-well lasers, which so clearly show a strong deviation from bulk crystal behavior, we summarize in the box on the right the deviations from well-known physics and engineering principles that we expect for small devices. We cannot give a comprehensive description of all the effects we list. We have discussed quantization, velocity saturation, and hot-electron emission. The overshoot effects listed in the box are connected with energy and momentum relaxation by collisions. Some of the effects (such as the Franz-Keldysh effect) have been known for a long time but up to now have been unimportant in device applications. The rest are connected with the unusual boundary conditions (interfaces) in small devices and layers, and with the small number

of charge carriers and impurities in the extremely small volume.¹

Opto-electronics

So far we have discussed hot-electron effects that are driven or engendered by an applied electric field, as in a transistor or Gunn-effect oscillator. As a prototype for various forms of semiconductor lasers, and perhaps other optoelectronic or integrated-optics devices, let us assume that the middle

Effects expected for small devices

Drift

- Deviations from Ohm's Law
- Saturation of current
- Velocity overshoot
- Ballistic transport
- Mobility increased or decreased by size effects (remote point charges, phonons)
- Scattering—high electric fields
- Generation of high phonon intensities

Diffusion

- Hot-electron diffusion and invalidation of the Einstein relation
- Enhancement of diffusion constant by high electric fields
- Anisotropy of diffusion
- Diffusion and reduced dimensionality
- Diffusion overshoot

Carrier generation and recombination

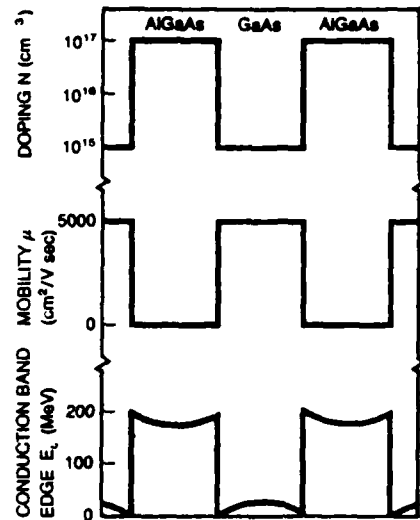
- Poole-Frenkel enhancement of emission out of potential wells (traps)
- Hot electron "thermionic" emission
- Effects of hot electrons on the Lax cascade mechanism
- Franz-Keldysh effect
- Impact ionization (inverse Auger process) can determine ultimate limits of speed, and so forth.
- Generation-recombination noise for non-stationary case (Langevin)

Size effects

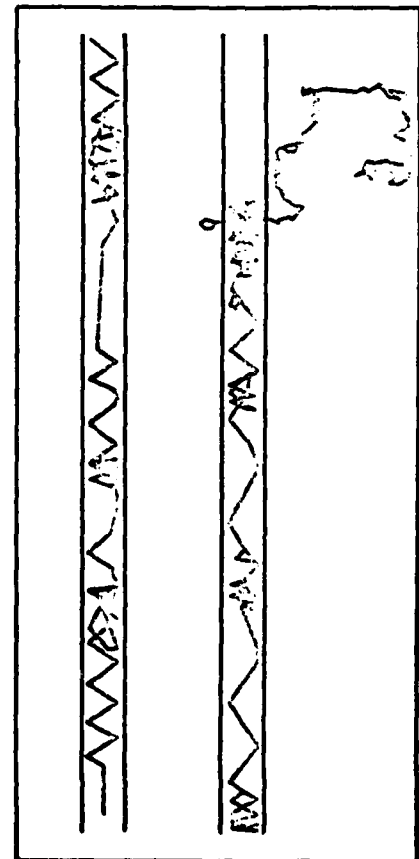
- Size quantization (two-dimensional, one-dimensional electrons)
- Quantum resonances
- Interfaces, surfaces, metal boundaries and influence of these boundaries on important semiconductor parameters.
- Image force (metal boundaries)
- Non-ideal interfaces
- Contacts as boundaries

Density-size relations

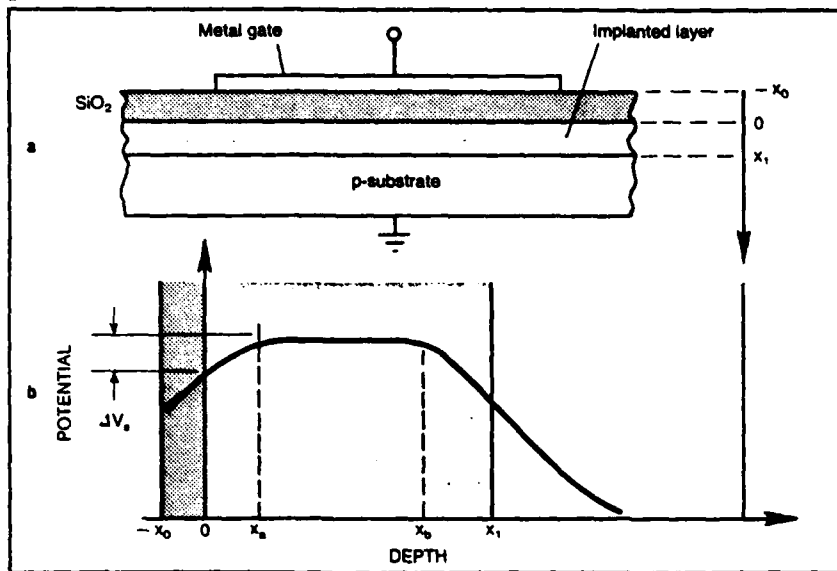
- Steep concentration gradients and high electric fields. (See diffusion)
- Alloy effects (atom disorder)
- Low-level radiation effects (α -particles from package)
- Interconnection problems (sheet resistance)



Layered structure, consisting of gallium arsenide and aluminum gallium arsenide. The graphs show the impurity doping concentration, the carrier mobility and the energy of the conduction band of this modulation-doped structure. Figure 3



Electron motion, computed by a Monte Carlo simulation, in a potential well formed by a gallium arsenide layer. The wells are broad enough (400 Å) that they show no effects due to size quantization. On the left the field strength is 2 kV/cm, below the threshold for jumping out of the well; on the right the field is 6 kV/cm. Figure 4



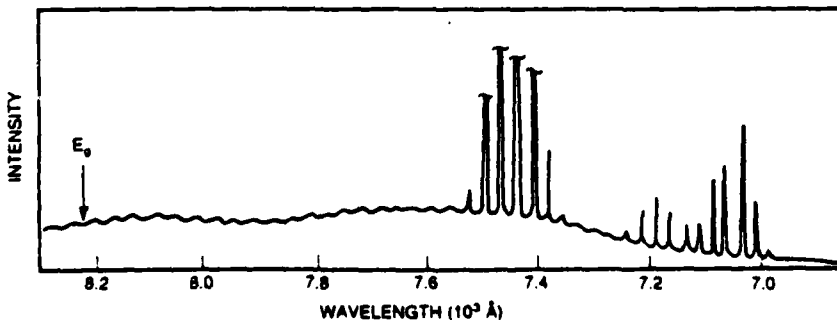
A buried-channel metal-oxide-semiconductor structure. The structure of the device is shown in the upper diagram. The graph below shows the potential as a function of depth. Cold electrons reside at the potential-energy minimum, between x_a and x_b . If the electrons become "hot" (because of, say, high electric fields), they can spread to the interface, that is, they overcome the potential barrier ΔV_s . Figure 5

layer of GaAs in figure 3 is 200 Å thick and that the $\text{Al}_x\text{Ga}_{1-x}\text{As}$ layers on either side are 0.5–1 micron thick. If we put the structure in contact with a good heat sink and photopump it with an intense light source, electrons and holes are generated in the $\text{Al}_x\text{Ga}_{1-x}\text{As}$ layers and will be collected (in a very short time) in the GaAs potential well. Relative to the bottom of the GaAs well, however, these electrons are "hot," that is, they are high above the GaAs band edge E_C in energy and can either scatter downward to the bottom of the GaAs well, releasing lattice vibrations (phonons) in the process, or, while still hot and high in the well, they can recombine with holes, releasing high-energy photons (red, not the usual infrared of bulk GaAs!). This is a remarkable effect; a crystal system that normally (in bulk) emits infrared light, when made into a quantum well,

emits (via the recombination of hot electrons and holes) true red light.¹²⁻¹⁴ This is shown in figure 6 by the laser emission near 7000 Å.

The hot-carrier red-light emission from GaAs shown in figure 6 was first observed by Robert Kolbas and Holonyak¹² on quantum-well crystals first grown by their coworkers at Rockwell International, Russell Dupuis and Daniel Dapkus and, later, James J. Coleman. We should mention that the quantum-well structure that emits the red light (as well as the longer-wavelength infrared laser light) of figure 6 can be constructed by putting doped p -type material on one side of the GaAs quantum-well and n -type on the other side; it then operates as a unique form of injection laser: a hot-carrier quantum-well semiconductor laser.

It is also possible to insert, or couple together, more than one quantum well



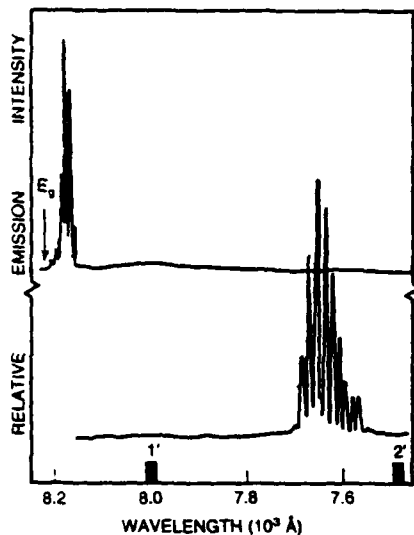
Stimulated emission due to the recombination of photogenerated hot electrons and holes in a 200 Å thick GaAs quantum well. The hot-carrier emission occurs high in the quantum well above the GaAs energy gap (E_g), in the visible (red) portion of the spectrum. This visible radiation is possible only from such a thin (quantum-well) layer. Figure 6

in the center of the structure as the layered structure of figure 2 shows. In that case, the hot-carrier collection and the downward scattering into the quantum wells can be much more efficient. If the number of these quantum wells is not too great and the wells are not too thick, say six wells, each 50 Å thick, one can observe still another important effect at sufficient excitation (photo-pumping or current excitation): The hot carriers scatter down towards the bottom of the quantum wells and, instead of recombining at the first (lowest) quantum states of the coupled GaAs wells, the carriers will scatter down even further and produce laser emission on a phonon sideband.

Just as the collection and the scattering of hot carriers to lower energy in a layered structure is improved when more than one quantum well is employed, carrier scattering to lower energies in a single potential well is constrained—and, in fact, makes possible the hot-carrier electron-hole recombination observed^{12,15} over the unusually large wavelength range of figure 6. If the rather large (200 Å thick) well that produced this spectrum is reduced in thickness to much under 100 Å, then the size constraint does not permit carriers to scatter down to the lower quantum states before recombination occurs. When a single potential well becomes as small as 80 Å, the highly mobile electrons can travel all the way across the potential well before colliding with the lattice. For excessively thin layers, then, the hot electrons tend to travel right across the very narrow well instead of scattering, losing energy, and descending into the well.^{16,17}

If these ideas and observations have much validity, it should be possible to verify them by still other means. Hot carriers lose energy by collisions with the crystal lattice, thereby converting some of their energy to increased lattice vibrations, or, equivalently, an increased phonon density. The process is strong when the coupling between the charge carriers and the lattice vibrations is strong. The electron-phonon coupling can be screened by introducing a large background of free carriers into the crystal, such as a large number ($10^{19}/\text{cm}^3$ or more) of positive holes—which can be introduced by diffusing zinc atoms to serve as acceptors into the layered structure. The screening is such a powerful effect that when carried out on the sample that produced figure 6, the weakening of the electron-phonon interaction almost cuts off the carrier scattering into the well: the hot carriers no longer scatter into the (rather large) quantum well, and the laser spectrum vanishes.¹⁷

We have to construct a much bigger active region to be able to see that the zinc doping merely screens the elec-



Comparison of laser spectra of (a) an undoped and (b) a zinc-doped (hole density $10^{19}/\text{cm}^3$) layered heterostructure consisting of six 120-Å GaAs quantum wells coupled by five 120-Å AlGaAs barriers. In (a) the photo-generated hot carriers thermalize to low energy while with the zinc impurity, in (b), the electron-phonon interaction is screened, so the carriers remain hotter and recombine at higher energy (100 meV). Figure 7

tron-phonon interaction and does not in fact damage the layered structure, and thus "kill" the light emission of the GaAs quantum wells. The screening effect of the doping is seen in figure 7. The device that produced these graphs consists of six layers (120 Å thick) of GaAs separated by five equally thick layers of AlGaAs. The top spectrum shows the laser emission from the undoped sample one phonon below the lowest quantum states (1'). When zinc doping is introduced into the sample (generating, as we said, a large background of holes), the photogenerated hot carriers cannot thermalize to as low an energy before recombination (because of screening and a weaker electron-phonon coupling), and the laser operation (curve b) shifts up in energy by 100 meV to the region of the second quantum states (2') of the coupled quantum wells. That is, the higher-energy laser operation at 7655 Å of curve b involves the recombination of carriers that are hotter than those leading to the laser operation (8180 Å) at the lower energy of curve a.

It is worth mentioning that the results of figure 7 are in excellent agreement with the hot-electron effects mentioned earlier. The quantum-well laser operation occurring at 7655 Å in curve b of figure 7 corresponds to an electron temperature of about 1330 K compared to a lattice temperature of about 77 K (the copper heat sink for the crystal is immersed in liquid nitro-

gen). In essence, the impurity screening has switched off some of the carrier energy loss to the lattice (to phonons), and, as a consequence, more of the input energy emerges from the crystal as higher energy recombination radiation (crystal laser output).

Small devices

Although the ideas and examples presented here concerning hot-electron effects in semiconductors are not exhaustive, they are representative and show clearly that newer semiconductor devices, as well as a higher level of integrated circuit development and smaller sizes, will inevitably make hot-carrier effects more and more important. Making semiconductor elements smaller and closer together to increase the number of active elements per square centimeter or per chip, is not a matter of just finding methods of reducing device size and generating a microscopic system of element interconnections. New physical effects and processes will appear.

The increased power densities involved in small-device operation makes higher-order processes important. For example, we mentioned above in some detail the phonon sidebands that appear in quantum-well heterojunction lasers. It is clear, however, that high phonon densities are also generated:

- ▶ during material processing such as laser annealing
- ▶ by the exceedingly high local current densities possible in VLSI elements
- ▶ in research such as picosecond spectroscopy.

The simple statement in solid-state textbooks that indirect optical processes (involving phonons) are unimportant ceases to be true even in the case of direct semiconductors.

Another class of new effects is connected with the unusual boundary conditions in small structures. The cyclic (Born-von Karman) boundary conditions, which are so convenient in solid-state theory, are inappropriate for quantum-well heterostructures and for very small devices. Instead of finding a "repeated crystal" after a large number of atoms, the electron can, as we know, transfer out of the silicon into the silicon dioxide and thereby limit the functioning lifetime of semiconductor devices. This process involves electron energies of about 3 eV above the conduction-band edge. The interesting question therefore arises whether this emission process can be avoided by using supply voltages lower than 3 volts or by using band-structure effects such as Bragg reflection. This question is also relevant for the possibility of high-speed, low-temperature silicon circuits but is too complicated for us to discuss here in detail.

The effect of hot-electron emission

can possess positive aspects, as it can clearly be used to construct ultra-fast electronic switches.⁹ The issue of boundary conditions and size effects also opens fascinating possibilities for optoelectronic devices, which are illustrated, for example, by the red-light emission of gallium arsenide.

Small integrated semiconductor devices already have had a strong impact on our daily lives; the impact promises to continue and, in fact, increase in scope. This will in turn further stimulate research in the field of "ultra-small electronics."

* * *

We are indebted to John Bardeen and Charles B. Duke for helpful comments, and to the NSF, the Navy, and the Army for support.

References

1. See, for example, the papers of K. Hess, D. K. Ferry and J. R. Barker in *Physics of Nonlinear Transport in Semiconductors*, D. K. Ferry, J. R. Barker and C. Jacoboni, eds., Plenum, New York (1980).
2. M. L. Cohen, T. K. Bergstresser, *Phys. Rev.* **141**, 789 (1966).
3. E. M. Conwell, *High Field Transport in Semiconductors*, Academic, New York (1967).
4. See K. Hess, in reference 1.
5. S. M. Sze, *Physics of Semiconductor Devices*, Wiley, New York (1969).
6. This effect was first proposed by John Bardeen and J. R. Schrieffer (*Phys. Rev.* **97**, 641 (1955)) for MOS transistors and later investigated in detail by F. Stern *Phys. Rev. B* **5**, 4891 (1972).
7. L. Esaki, R. Tsu, IBM Research Report No. RC-2418, 1969. See also *PHYSICS TODAY* April 1979, page 20; R. Dingle, H. L. Stormer, A. C. Gossard, W. Wiegmann, *Appl. Phys. Lett.* **3**, 665 (1978).
8. K. Hess, *Appl. Phys. Lett.* **35**, 484 (1979); K. Hess, P. Vogl, *Solid State Commun.* **30**, 807 (1979).
9. K. Hess, H. Morkoç, H. Shichijo, B. G. Streetman, *Appl. Phys. Lett.* **35**, 469 (1979).
10. T. Ning, *Solid-State Electron.* **21**, 273 (1978).
11. See the papers of D. K. Ferry and J. R. Barker, in reference 1.
12. R. M. Kolbas, N. Holonyak Jr., R. D. Dupuis, P. D. Dapkus, *Pis'ma Zh. Tekh. Fiz.* **4**, 69 (1978), (*Sov. Tech. Phys. Lett.* **4**, (1978)).
13. N. Holonyak Jr., R. M. Kolbas, R. D. Dupuis, P. D. Dapkus, *IEEE J. Quantum Electron.* **QE-16**, 170 (1980).
14. *PHYSICS TODAY*, April 1979, page 20.
15. N. Holonyak Jr., R. M. Kolbas, E. A. Rezek, R. Chin, R. D. Dupuis, P. D. Dapkus, *J. Appl. Phys.* **49**, 5392 (1978).
16. R. M. Kolbas, N. Holonyak Jr., B. A. Vojak, K. Hess, M. Altarelli, R. D. Dupuis, P. D. Dapkus, *Solid State Commun.* **31**, 1033 (1979).
17. N. Holonyak Jr., R. M. Kolbas, W. D. Laidig, B. A. Vojak, K. Hess, R. D. Dupuis, P. D. Dapkus, *J. Appl. Phys.* **51**, 1328 (1980).